

## ABSTRACT

Title of Document:

CHEMICAL FUNCTIONALIZATION OF  
CARBON NANOTUBES FOR CONTROLLED  
OPTICAL, ELECTRICAL AND DISPERSION  
PROPERTIES

**Alexandra Brozena, Doctor of Philosophy,  
2013**

Directed By:

Professor YuHuang Wang, Department of  
Chemistry and Biochemistry

A carbon nanotube is a graphitic sheet, rolled into a one-dimensional, hollow tube. This structure provides certain *individual* nanotubes with high conductivity and near-infrared optical activity. These properties are not necessarily translated at the macroscale, however, due to strong van der Waals attractive forces that determine the behavior at the bulk level – exemplified by aggregation of nanotubes into bundles with significantly attenuated functionality. Different methods of carbon nanotube covalent functionalization are studied to improve dispersion while simultaneously maintaining intrinsic electrical and optical properties. In addition to retention of known behavior, new carbon nanotube photoluminescence pathways are also revealed as a result of this same covalent functionalization strategy.

With various wet chemistries, including super-acid oxidation, the Billups-Birch reaction, and various diazonium based reactions, that utilize strong reducing or

oxidizing conditions to spontaneously exfoliate aggregated carbon nanotubes, we are able to covalently functionalize individually dispersed nanotubes in a highly scalable manner. Covalent addition to the nanotube sidewalls converts the native  $sp^2$  hybridized carbon atoms to  $sp^3$  hybridization, which helps disrupt inter-tube van der Waals forces. However, this change in hybridization also perturbs the carbon nanotube electronic structure, resulting in an undesired loss of electrical conductivity and optical activity. We observe that controlling the location of functionalization, such as to the outer-walls of double-walled carbon nanotubes or as discrete functional “bands,” we avert the loss of desirable properties by leaving significant tracts of  $sp^2$  carbon atoms unperturbed. We also demonstrate that such functional groups can act as electron and hole traps through the creation of a potential well deviation in the carbon nanotube electronic structure. This defect-activated carrier trapping primes the formation of charged excitons (trions) which are observed as redshifted photoluminescence in the near-infrared region. Implications and impacts of these covalent functionalization strategies will be discussed.

CHEMICAL FUNCTIONALIZATION OF CARBON NANOTUBES FOR  
CONTROLLED OPTICAL, ELECTRICAL, AND DISPERSION PROPERTIES.

By

Alexandra H. Brozena

Dissertation submitted to the Faculty of the Graduate School of the  
University of Maryland, College Park, in partial fulfillment  
of the requirements for the degree of  
Doctor of Philosophy  
2013

Advisory Committee:

Professor YuHuang Wang, Chair

Professor Philip DeShong

Professor John Fourkas

Professor Lawrence Sita

Dean's Representative: Professor John Cumings

To my family and husband.

## Acknowledgements

This work was made possible by the support of many people. My advisor Professor YuHuang Wang's vision of carbon nanotubes was instrumental in encouraging us to think beyond and around the problems that surround this material. I would also like to thank my co-workers, particularly Jarrett Leeds, for teaching me so much in the lab and about Chemistry. I would also like to thank Professor Gary Rubloff and Dr. Ashley Predith for their mentoring and support, and for welcoming me into the Nanostructures for Electrical Energy Storage - Energy Frontier Research program (NEES-EFRC). Being a part of this research effort and observing how large, multi-institutional grants such as this one are organized and run was a career opportunity that I have very much appreciated. I would like to thank Dr. Lee Friedman and Dr. Daniel Steffek, who could not have been better professors to TA for. I would also like to thank my committee members for their direction on this work. And it goes without saying, that I owe my family and loved ones significant thanks for their continued belief in me and emotional support during my time at the University of Maryland in pursuit of my doctoral degree.

Financially, this research was supported by many sources which I would like to thank. I would particularly like to acknowledge the Department of Energy Office of Science Graduate Fellowship Program (DOE-SCGF), which was made possible in part by the American Recovery and Reinvestment Act of 2009, administered by ORISE-ORAU under contract no. DE-AC05-06OR23100 for fellowship support. This research was also supported in part by the National

Science Foundation (CAREER CHE – 1055514), the Office of Naval Research (N000141110465), startup funds and a General Research Board Research Support Award from the University of Maryland, a Nano-Biotechnology Initiative Start-up Award from the Maryland Department of Business and Economic Development, and partially supported as part of the Science of Precision Multifunctional Nanostructures for Electrical Energy Storage, an Energy Frontier Research Center funded by the U.S. Department of Energy, Office of Science, Office of Basic Energy Sciences under Award Number DESC0001160. The support of the Maryland NanoCenter and shared experimental facilities supported by the NSF MRSEC under grant DMR 05-20471 are also grateful acknowledged.

I would also like to thank Dr. Li-Chung Lai and Dr. Wen-An Chiou for assistance with the transmission and scanning electron microscopes, Karen Gaskell for assistance with x-ray photoelectron spectroscopy, and Professor Gary Rubloff for access to the Horiba Jobin Yvon LabRAM HR800 Raman microscope.

## Table of Contents

Acknowledgements.....	iii
Table of Contents .....	v
List of Tables .....	vii
List of Figures .....	viii
List of Abbreviations .....	xii
Chapter 1: Introduction .....	1
Background .....	2
Polydispersity Issue .....	8
Aggregation Issues.....	10
Surfactant Dispersion.....	12
Covalent Functionalization Strategies .....	15
New Optical Properties of Functionalized CNTs .....	20
Chapter 2: Outer-Wall-Selectively Oxidized, Water soluble Double-Walled Carbon Nanotubes.....	23
Introduction.....	23
Materials and Methods.....	26
Outer-wall Selective Oxidation of Superacid Intercalated DWCNTs .....	26
Relative Solubility of Oxidized DWCNTs Prepared at Different Reaction Conditions .....	27
Determining Maximum Water Solubility of Oxidized DWCNTs .....	28
X-ray Photoelectron Spectroscopy .....	28
Raman Spectroscopy.....	29
Electron Microscopy .....	29
Carbon Nanotube Thin Film Conductivity Measurements .....	30
Results and Discussion .....	30
Outer-wall Selectivity .....	30
Oso-DWCNT Solubility .....	38
Improved Conductivity Percolation of Oso-DWCNTs.....	40
Conclusions.....	45
Chapter 3: Confined Propagation of a Covalent Chemistry on Single-Walled Carbon Nanotubes.....	48
Introduction.....	48
Materials and Methods.....	50
Synthesis of HiPco- $[(CH_2)_5COONa]_n$ .....	50
Synthesis of CoMoCat- $[(CH_2)_5COONa]_n$ , CoMoCat- $[(CH_2)_5CH_3]_n$ and CoMoCat-[H] $_n$ .....	51
3-Cycle reaction and water extraction .....	52
Solubility measurement .....	52
Spectroscopy characterization .....	52
Au-Substrated Enhanced Scanning Electron Microscopy .....	53
Atomic Layer Deposition.....	53

Thermogravimetric analysis.....	54
Results and Discussion .....	54
“Banded” SWCNTs .....	54
Propagation modes.....	58
Optical properties.....	60
Conclusions.....	70
 Chapter 4: Trion Photoluminescence of Covalently Functionalized, Semiconducting carbon nanotubes .....	73
Introduction.....	73
Materials and Methods.....	77
Covalent Functionalization Chemistries .....	77
Spectroscopy .....	79
Results and Discussion .....	80
Photoluminescence of Negative Trions .....	80
Photoluminescence of Positive Trions.....	91
SWCNT Trion Defect Dependence .....	99
Conclusions.....	103
 Chapter 5: Conclusions and Outlook .....	104
 Appendix 1.....	111
Bibliography .....	119

## List of Tables

**Table 2-1.** XPS of raw DWCNTs, 5 mL 24 hrs and 10 mL 2 hrs samples.

**Table 2-2.** Electrical conductivity of *oso*-DWCNTs thin films in comparison with pristine DWCNTs, SWCNTs, and functionalized SWCNTs

**Table 3-1.** Net atomic charges around a sp<sup>3</sup> defect site from Mulliken population analysis of a SWCNT with a covalently bonded -(CH<sub>2</sub>)<sub>5</sub>COOH group.

**Table 3-2.** Net atomic charges on a (10,0)-(CH<sub>2</sub>)<sub>5</sub>COOH SWCNT.

**Table 3-3.** Net Atomic Charges on a (5,5)-(CH<sub>2</sub>)<sub>5</sub>COOH

## List of Figures

**Figure 1-1.** Early transmission electron microscope images of a double walled and a multi-walled CNT taken by Sumio Iijima's group, frequently credited with the modern discovery of CNTs.

**Figure 1-2.** Vector diagram of a CNT on an unrolled sheet of graphene.

**Figure 1-3.** Graphene energy dispersion and zone-folding method of deriving the CNT band structure using the graphitic Brillouin zone.

**Figure 1-4.** The DOS diagram of semiconductor and metallic CNTs.

**Figure 1-5.** A cross-section of a bundled, DWCNT "rope" as viewed by TEM.

**Figure 1-6.** Potential surfactant adsorption arrangements on a CNT and resulting optical properties of individually dispersed CNTs using surfactant to individualize the nanotubes.

**Figure 1-7.** An example of CNT covalent functionalization by a diazonium salt.

**Figure 1-8.** Calculated CNT conductance as a function of energy near the Fermi level dramatically decreases with increasing carbon atom functionalization.

**Scheme 1-1.** Schematic strategy of positionally controlled CNT covalent functionalization to avoid the tradeoff of desirable properties that are linked to  $sp^2$  carbon atoms.

**Scheme 2-1.** Illustration of outer-wall selective oxidation of DWCNTs by  $H_2SO_4/HNO_3$ .

**Figure 2-1.** Raman spectral evidence of outer-wall selectivity.

**Figure 2-2.** Raman spectra of the 10 mL 2 hrs sample in comparison with raw DWCNTs.

**Figure 2-3.** Comparative TEM studies of *oso*-DWCNT samples with highest water solubility (5 mL 24 hrs) and highest outer-wall selectivity (10 mL 2 hrs).

**Figure 2-4.** Length distribution of raw, 10 ml 2 hrs, 5 ml 24 hrs oxidized samples.

**Figure 2-5.** XPS of the raw DWCNTs and the 10mL 2 hrs oxidized sample.

**Figure 2-6.** Relative water solubility and degree of functionalization of oxidized DWCNTs under increasing amount of  $\text{HNO}_3$  at a fixed reaction time of 2 hrs and increasing reaction time using 5mL  $\text{HNO}_3$ .

**Figure 2-7.** Electrical percolation of *oso*-DWCNTs via inner-tubes.

**Scheme 3-1.** Schematic illustration of the recycling, reductive alkylation of SWCNTs.

**Figure 3-1.** Functional bands on SWCNTs.

**Scheme 3-2.** An illustration of the growth of  $\text{Al}_2\text{O}_3$  from carboxylic acid functional groups on the CNT surface with self-limiting, cycled  $\text{Al}_2\text{O}_3$  chemistry.

**Figure 3-2.** TEM images of non-functionalized, 40 cycles Billups-Birch hexanoic acid functionalized SWCNTs before and after 10 and 50 cycles of  $\text{Al}_2\text{O}_3$  deposition at  $-\text{COOH}$  groups.

**Figure 3-3.** Two modes of propagation revealed in the length distributions of intact segments and functional bands.

**Figure 3-4.** Visible-NIR absorption spectrum and excitation-emission map of the 3-cycle HiPco-SWCNT-[ $(\text{C}_2\text{H}_5)_5\text{COOH}$ ]<sub>n</sub> in comparison with the starting, non-functionalized nanotubes, which were individually dispersed in  $\text{D}_2\text{O}$  solutions of 1wt% SDBS.

**Figure 3-5.** Water soluble SWNT-[ $(\text{CH}_2)_5\text{COONa}$ ]<sub>n</sub>.

**Figure 3-6.** A kinetic model of reaction propagation from a point defect on a  $\text{sp}^2$  bonded carbon lattice.

**Figure 3-7.** TGA of HiPco-[ $(\text{CH}_2)_5\text{COOH}$ ]<sub>n</sub>.

**Figure 3-8.** FT-IR of SWNT-[ $(\text{CH}_2)_5\text{COOH}$ ]<sub>n</sub> showing increased IR absorbance for  $-\text{COOH}$  and C-H from starting material.

**Figure 3-9.** Evolution of Billups-Birch reductive addition.

**Figure 3-10.** Optimized structure of a (5,5)-SWCNT with a covalently bonded - $(\text{C}_2\text{H}_5)_5\text{COOH}$  group.

**Figure 4-1.** DFT modeling reveals the splitting of the energy states that make up the SWCNT  $E_{11}$  transition as covalent functionalization increases.

**Scheme 4-1.** Proposed exciton diffusion pathways of a functionalized carbon nanotube under reducing conditions.

**Figure 4-2.** Sidewall propagative alkylcarboxylation of (6,5) SWCNTs produces two new photoluminescence peaks,  $E_{11}^-$  and  $E_T$ , in addition to the  $E_{11}$  exciton transition.

**Figure 4-3.** Photoluminescence emission spectra of 3 cycles Billups-Birch alkylcarboxylated SWCNTs using 970 and 570 nm excitation wavelengths (corresponding to the  $E_{11}$  and  $E_{22}$  (6,5) transitions respectively), normalized to the  $E_T$  peak.

**Figure 4-4.** Emission spectra of pristine and alkylcarboxylated SWCNTs after 3 cycles of the Billups-Birch alkylcarboxylation using different excitation lines.

**Figure 4-5.** Photoluminescence and absorption spectra of SWCNTs functionalized by 1 cycle of the Billups-Birch alkylcarboxylation reaction.

**Figure 4-6.** Emission spectra of 1 wt% SDBS-D<sub>2</sub>O suspended (6,5) SWCNTs functionalized by hexanoic acid groups using the Billups-Birch reduction before and after dispersion in oleum shows the change in the intensity of the  $E_T$  peak after reducing conditions are removed.

**Figure 4-7.** An excitation study of the 3 cycle Billups-Birch functionalized, oleum treated sample indicates the position of the  $E_{11}^-$  and  $E_T$  peaks that come into resonance at the same excitation as the (6,5)  $E_{11}$  transition.

**Figure 4-8.** UV-Visible-NIR absorption spectra of the Billups-Birch alkylcarboxylated SWCNTS before and after oleum treatment.

**Figure 4-9.** Dispersion of pristine SWCNTs in oleum or with sodium in liquid ammonia, without functionalization, fails to produce  $E_T$  in the photoluminescence spectra.

**Figure 4-10.** A van't Hoff plot was used to derive an average well depth of  $75.3 \pm 4.6$  meV/ $sp^3$  carbon atom for 3 cycle, Billups-Birch alkylcarboxylated (6,5) SWCNTs.

**Figure 4-11.** 3-D photoluminescence excitation-emission maps of (6,5) SWCNTs dispersed in 1 wt% SDBS-D<sub>2</sub>O before and after covalent functionalization by 4-nitrobenzene groups using an in-situ diazonium chemistry in oleum.

**Figure 4-12.** Multi-line excitation study of 4-nitrobenzene functionalized and pristine SWCNTs reveal that  $E_{11}^-$  and  $E_T$  are in resonance with the (6,5)  $E_{11}$  transition.

**Figure 4-13.** Raman spectra of pristine and 4-nitrobenzene functionalized SWCNTs.

**Figure 4-14.** Modulation of the 4-nitrobenzene functionalized SWCNT  $E_T$  peak is accomplished through subsequent reduction by different equivalents of sodium.

**Figure 4-15.** Raman spectroscopy of 4-nitrobenzene SWCNTs functionalized in oleum and subsequently dried and reduced with varying equivalents of sodium in liquid ammonia.

**Figure 4-16.** The peak at 1125 nm for the 4-nitrobenzene functionalized SWCNT sample contains convoluted data from multiple nanotubes in solution.

**Figure 4-17.** (A) Covalent functionalization SWCNTs by 4-nitrobenzene under neutral, aqueous conditions produces the  $E_{11}^-$  peak alone. (B) Subsequent sodium reduction of the functionalized SWCNTs revealed a second peak,  $E_T$ , suggesting a defect dependence of trion emission under these conditions.

**Figure 4-18.** TFTs made from the diazonium functionalized and reduced samples.

## List of Abbreviations

**ALD:** Atomic Layer Deposition

**CNT:** Carbon Nanotube

**CoMoCat:** Cobalt Molbydneum Catalyst

**CVD:** Chemical Vapor Deposition

**DFT:** Density Functional Theory

**DOS:** Density of States

**DWCNT:** Double-Walled Carbon Nanotube

**E<sub>11</sub>:** Excitonic SCWNT energy transition between the first valence and conduction band van Hove singularities

**E<sub>11̄</sub>:** Defect activated SWCNT intra-bandgap transition

**E<sub>22</sub>:** Excitonic SWCNT energy transition between the second valence and conduction band van Hove singularities

**E<sub>T</sub>:** Intra-bandgap SWCNT trion transition

**FEG:** Field Emission Gun

**FET:** Field Effect Transistor

**FT-IR:** Fourier Transform-Infrared spectroscopy

**FWCNT:** Few-Walled Carbon Nanotube

**FWHM:** Full Width at Half Maximum

**HDPE:** High-Density Polyethylene

**HiPco:** High-Pressure Carbon Monoxide

**IR:** Infrared

**MWCNT:** Multi-Walled Carbon Nanotube

**Oso-DWCNTs:** Outerwall Selectively Oxidized Double-Walled Carbon Nanotubes

**PL:** Photoluminescence

**RBM:** Radial Breathing Mode

**SDBS:** Sodium Dodecylbenzenesulfonate

**SDS:** Sodium Dodecylsulfonate

**SEM:** Scanning Electron Microscopy

**SWCNT:** Single-Walled Carbon Nanotube

**TEM:** Transmission Electron Microscopy

**TFT:** Thin Film Transistor

**TGA:** Thermogravimetric Analysis

**TMA:** Trimethyl Aluminum

**Wt.:** Weight

**UV:** Ultraviolet

**UV-Vis-NIR:** Ultraviolet-Visible-Near-Infrared

**XPS:** X-ray Photoelectron Spectroscopy

## Chapter 1: Introduction

Carbon nanotubes (CNTs) generated considerable excitement after their discovery, leading to predictions of high impact applications such as space elevators<sup>1</sup> and nanometer scale transistors.<sup>2</sup> So far, however, these materials have yet to achieve these exceedingly high device expectations. It is worthwhile to note that the study of CNTs has barely crossed the 20-year mark. With this in mind, patience is counseled on the development of CNT based applications and a renewed focus on the fundamental research, necessary to overcome the current, acknowledged limitations of this material, is urged.

This work aims to address some fundamental issues of carbon nanotubes by studying the chemistry of the carbon-carbon, double-bond crystal structure that grants CNTs a unique combination of superior physical properties (electrical, optical, thermal, and mechanical).<sup>3</sup> The delocalized pi bonding scheme of these quantum confined materials generates an unusual electronic structure having both properties of molecular orbital levels and solid state energy bands. We have determined that the atomic and electronic structure of these materials enables CNTs to be chemically modified in a very controlled manner – particularly in the positional control of covalently attached functional groups on the nanotube surface. Consistent with the adage, “structure is function,” we have learned that controlling the location of functional groups on the nanotube surface allows us to tailor the properties of these materials to overcome some of the physical limitations of CNTs.

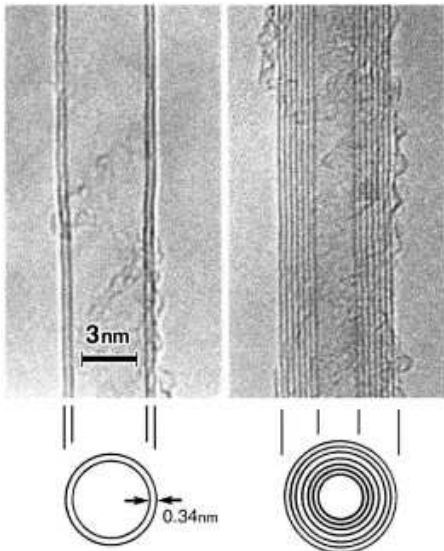


**Figure 1-1.** Early transmission electron microscope images of a double walled (left) and a multi-walled (right) CNT taken by Sumio Iijima's group, frequently credited with the modern discovery of CNTs.<sup>4</sup>

### *Background*

Of all the nanomaterials, perhaps none owe more to their advance and study than the striking visual discovery of CNTs by transmission electron microscopy (TEM) in the early 1990s.<sup>4–6</sup> While CNTs had been previously synthesized and observed without particular note,<sup>7</sup> it was Sumio Iijima's high resolution TEM images of these nanostructures that fostered widespread interest in graphitic materials (Figure 1-1).<sup>4,5</sup> CNTs are a unique nanomaterial composed entirely of carbon, and conceptually constructed (though not synthesized) by rolling a sheet of graphene into a tube as narrow as 0.7 nm wide.<sup>3</sup> In the same way that a sheet of paper can be rolled into a tube of varying width and length by deepening the twist, CNTs similarly vary by a unique structural twist, or chiral vector ( $C_h$ ), that can be defined using lattice vectors  $a_1$  and  $a_2$  to fulfill the

equation,  $C_h = n\mathbf{a}_1 + m\mathbf{a}_2$ . ( $n, m$ ) are integers and convenient indices to define the nanotube chirality<sup>3</sup> (Figure 1-2).

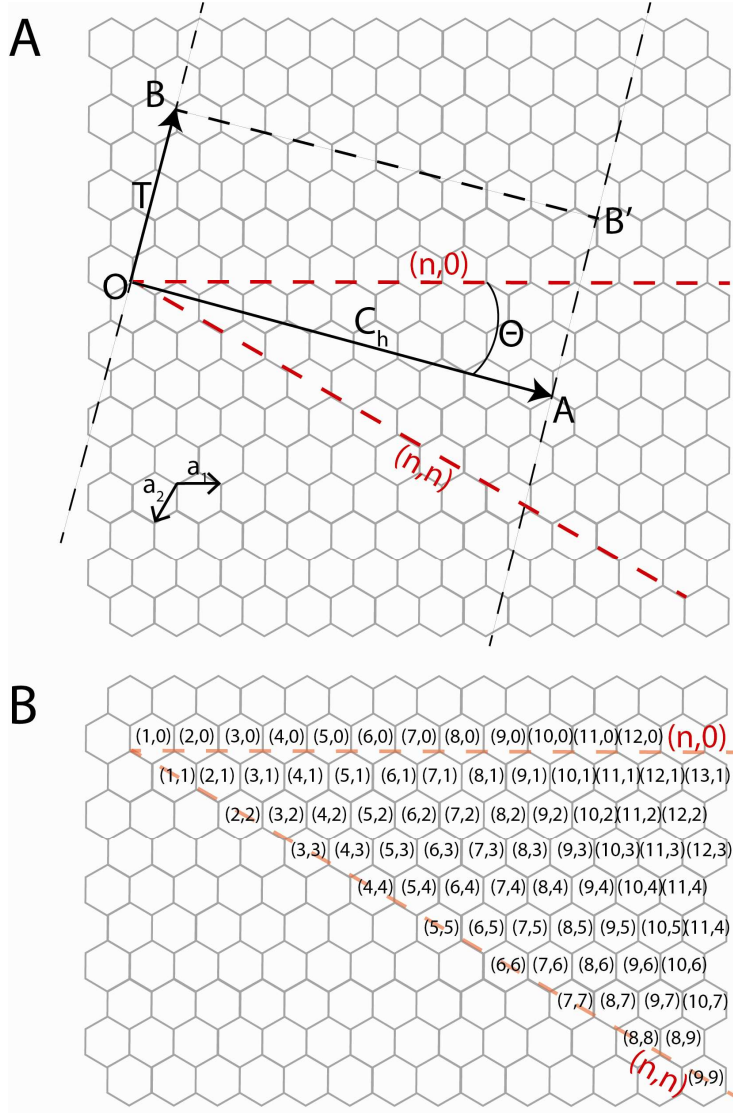


**Figure 1-2.** (A) When points O and A, and B and B' are brought together by “rolling” the graphitic sheet, they form the nanotube unit cell. This roll-up configuration can be defined by the chiral vector,  $C_h = n\mathbf{a}_1 + m\mathbf{a}_2$ , also abbreviated using the indices  $(n,m)$ . Shown here is the unit cell for a chiral vector made up by 8 $\mathbf{a}_1$  unit vectors and 3 $\mathbf{a}_2$  unit vectors, making this nanotube of the (8,3) chirality. The chiral angle,  $\square$ , is defined as the angle between the chiral vector  $C_h$ , and the “zigzag” line  $(n,0)$ . Varying the chiral angle and vector thus changes the identifying nanotube chirality,  $(n,m)$ . T is the translational vector and corresponds to the nanotube longitudinal axis. (B) A representative example of possible chiralities shown using the chiral indices labeled on a graphene sheet corresponding to the bottom right point of each hexagonal cell.

This chiral, “roll-up” vector determines more than just the diameter of the nanotube; it also plays a significant role in determining the electronic properties of the individual CNT type. As CNTs are one-dimensional (confined at the diameter to quantum scale dimensions, but of high aspect ratio along the axis), the electronic structure can be derived by taking a cross section of the two-dimensional graphene energy dispersion. Figure 1-3 displays the graphite Brillouin zone, with the K points corresponding to the degeneracies of the  $\pi$  and  $\pi^*$  (valence and conduction bands respectively) energy dispersion of graphene. Thus depending on where the CNT is “folded” from its graphene basis, a line which is determined by the chiral and translational vectors, the graphitic energy dispersion will be cross-sectioned by the resultant wave vectors at either a K point or between K points. These cross-sections corresponding to metallic (zero bandgap) or semiconducting (bandgap) band structure respectively. The metallic or semiconducting behavior of a nanotube chirality can be easily determined using the chiral indices according to the equation,  $n-m=3j$ . When  $j$  is an integer, the CNT chirality is metallic.<sup>3</sup>

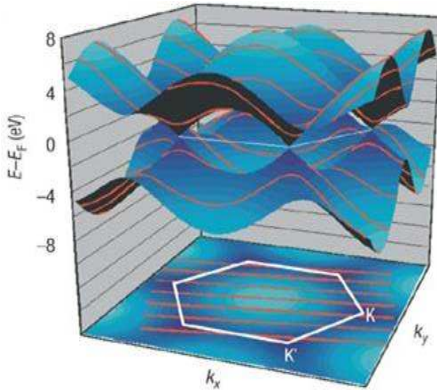


**Figure 1-3.** The cross section of the graphene energy dispersion relation can be used to derive the band structure of CNTs. Chiralities that correspond to a cross section that crosses through a K point results in metallic behavior.<sup>8</sup>

The CNT electronic density of states (DOS) feature the expected singularity structure of 1-dimensional materials.<sup>9</sup> These singularities, also known as van Hove singularities, enable a molecular-like transition that is chirality dependent, resulting in unique energy transitions that appear as discrete photon absorption and photoluminescence peaks for the semiconducting species, with transition energy inversely proportional to nanotube diameter.<sup>3</sup>

Often, these transitions are identified by the mirror valence and conduction band van Hove singularity states. For example, the wider gap of semiconducting CNTs is labeled S<sub>22</sub> and the smaller gap is S<sub>11</sub> (Figure 1-4A). Photoluminescence occurs by absorption of a photon of equal or greater energy than the S<sub>22</sub> transition, followed by vibrational relaxation of the excited electron to the conduction band S<sub>11</sub> state, at which point radiative relaxation may occur to cross the band-gap, resulting in an emitted photon. Energy states do occur within this bandgap, but are not optically active (and in fact are believed to be the cause of low, CNT photoluminescence quantum yield). The bandgap between these van

Hove valence and conduction band singularities is chirality dependent, which creates a unique combination of absorption excitation and photoluminescence emission wavelengths for each nanotube chirality. Photoluminescence of metallic CNTs does not occur due radiative quenching effects by the lower energy continuum states that reside at and around the Fermi level (Figure 1-4B). The  $S_{11}$  and  $M_{11}$  formalism to describe the van Hove transitions is often simplified to just  $E_{11}$  when electronic type is not defined or is assumed.

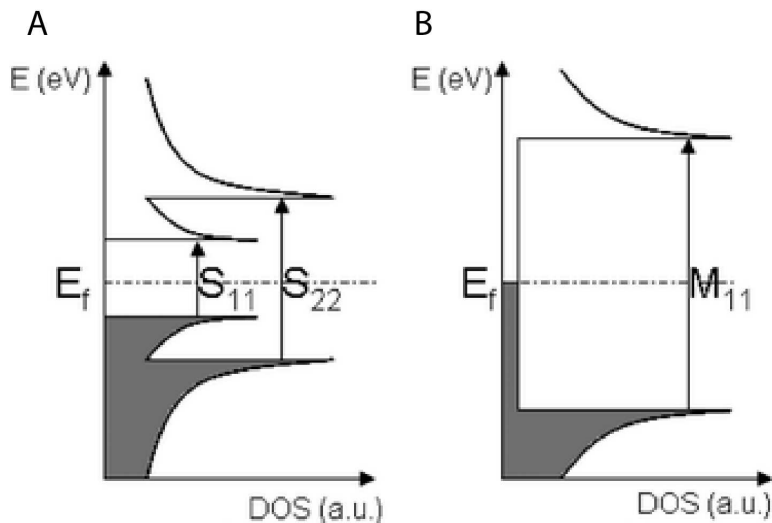


**Figure 1-4.** The DOS diagram of (A) semiconducting and (B) metallic CNTs. CNTs derive their optical properties from the transitions between the valence and conduction band van Hove singularities, labeled here  $S_{11}$  and  $S_{22}$  for the semiconductor species and  $M_{11}$  for metallic.<sup>10</sup>

Prior to the discovery of CNTs, it was understood that the extended conjugation of  $sp^2$  hybridized carbon-carbon bonds, would generate exciting properties that were just beginning to be understood within quantum confined dimensions.<sup>3</sup> Researchers have since discovered that the physical behavior of CNTs far exceeds initial expectations, including: a mobility higher than any other

known semiconductor ( $>100,000 \text{ cm}^2/\text{Vs}$ );<sup>11</sup> ballistic electron transport at room temperature;<sup>12</sup> a Young's modulus on the order of one terapascal (TPa);<sup>13</sup> thermal conductivity greater than 2000 W/mK;<sup>14</sup> and near-infrared (IR) photoluminescence that occurs in wavelengths not strongly absorbed by biological tissue.<sup>15-19</sup> These properties outstrip many widely utilized commercial materials, including copper and aluminum, in terms of conductivity,<sup>20</sup> and specific strength compared to steel.<sup>21</sup> These traits generated interest in developing a multitude of CNTs applications, including transistors for smaller microprocessors,<sup>2</sup> composite strength additives for ultra-light aerospace polymers,<sup>22,23</sup> biomedical imaging applications,<sup>18,19,24</sup> and current collectors for photovoltaics<sup>25,26</sup> and lithium ion batteries,<sup>27</sup> to name just a few.

However, proof-of-concept CNT devices and applications designed for these purposes largely failed to live up to expectations. Individual CNT devices worked as expected, but these same devices performed poorly when scaled up to practical dimensions. For example, macroscale fibers spun from individual CNTs were approximately 10 times weaker<sup>28</sup> than expected given the experimentally determined Young's modulus of individual nanotubes (~1.2 TPa).<sup>13,29</sup> It was also observed that CNT additives to polymer composites did not generally enhance the polymer strength and often made the material more prone to cracking.<sup>30</sup> Photoluminescence quantum yields were low (<1%)<sup>16,31</sup> due to fast, non-radiative decay pathways, making CNTs impractical for bio-imaging uses. CNT field effect transistors (FET) were exceedingly difficult to pattern in large arrays and demonstrated unexpectedly high failure rates due to low current on-off ratios .<sup>32,33</sup>

The early promise of CNTs stalled as it was determined that the properties of individual nanotubes under ideal environmental conditions were not the same as the bulk material and scaled devices.

Two major obstacles to these CNT applications were identified: 1) polydispersity and 2) the tendency of individual nanotubes to aggregate into bundles. We will briefly discuss the first issue and focus on the second for the rest of this work.

### *Polydispersity Issue*

The polydispersity issue is due to the current limitations of synthetic methods which generate many different types of CNTs. The “HiPco” process utilizes high-pressure carbon monoxide gas over a heated iron pentacarbonyl catalyst to grow SWCNTs, but always with a broad mixture of different chiralities.<sup>34</sup> These chiralities, which were described earlier, not only delineate the atomic structure of CNTs, but also define the electronic nature of these materials. Approximately 2/3 of synthesized CNTs are semiconducting and the remaining 1/3 are metallic.<sup>3</sup> Under these conditions, it is almost impossible to synthesize CNT-based electronics if the components cannot be reliably or uniformly made of either semiconducting or metallic material. This synthetic problem explains the low on-off ratio of CNT FET devices due to the incorporation of metallic nanotubes.<sup>32</sup>

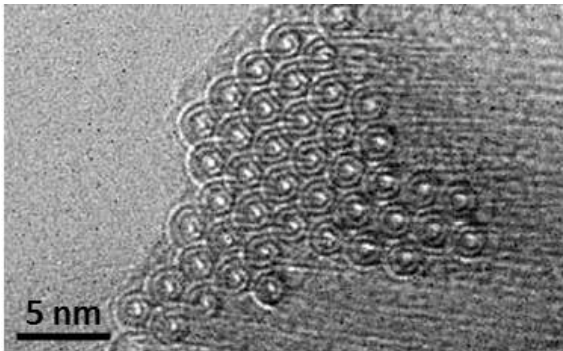


**Figure 1-5.** A cross-section of a bundled, DWCNT “rope” as viewed by TEM.<sup>35</sup>

An additional complication is that the number of graphitic walls or concentric nanotubes can depend on the synthesis method. Some CNTs are composed of only a single wall (SWCNTs); others are composed of two walls (double-walled carbon nanotubes or DWCNTs) (Figure 1-5). Few-walled carbon nanotubes (FWCNTs) contain 3-5 graphite walls, and multi-walled carbon nanotubes (MWCNTs) have >5 walls. As each concentric nanotube wall can be either semiconductor or metallic, DWCNTs and MWCNTs are often composed of both types for complex electronic character.

While the diverse electronic behavior of CNTs complicates their incorporation into devices, this problem is more practically solved at the synthetic level rather than by attempting post-synthetic separations, which have limited scalability.<sup>36-44</sup> While there is no method currently capable of producing pure electronic type or wall numbers, synthetic methods have been improving. For example, the CoMoCat process, a chemical vapor deposition method that uses a cobalt and molybdenum catalysts,<sup>45</sup> has been shown to be particularly successful at synthesizing SWCNTs enriched in single chiralities, including (6,5) and (7,5).<sup>46</sup>

Such SWCNTs are now commercially available through the companies such as South West NanoTechnologies (Norman, OK).

While the polydispersity problem is significant, the CNT aggregation issue has seen fewer advances in the last 10 years and may be the determining factor in the limitations of future applications. CNTs have a natural tendency to aggregate and form insoluble bundles, which limits processing and device fabrication methods. Additionally, we now understand that to retain the physical properties of CNTs in devices largely depends on maintaining the nanotubes in an individually dispersed state.

### *Aggregation Issues*

The fundamental properties of CNTs that attracted researchers are largely due to the  $sp^2$  covalent bonds that make up the carbon lattice of individual nanotubes. However, at bulk scale, inter-nanotube interactions are dominated by van der Waals forces. While van der Waals forces are much weaker than covalent bonds, the atomically flat and inflexible nature of CNTs enables large numbers of carbon atoms to come close together. This proximity additively increases the effect of the attractive van der Waals forces. For every nm of contacting CNTs, there is approximately 950 meV of van der Waals attraction.<sup>47</sup> Given the length of CNTs ( $>1\mu m$ )<sup>34</sup> and their atomically flat nature, these forces quickly add up, resulting in hexagonally packed, crystalline bundles<sup>35</sup> of nanotubes featuring diverse electronic and optical properties.

Van der Waals forces can interfere with CNT applications to fail by either being too weak or too strong, depending on the scenario. For example, while the

estimated tensile strength of an individual SWCNT is on the order of GPa,<sup>48</sup> a fiber spun out of many individual nanotubes exhibits only 116 MPa tensile strength.<sup>28</sup> Van der Waals forces are the weakest link connecting neighboring CNTs within the fiber so the structure frays at a much lower tension that is expected from individual nanotubes, whose properties are dictated by carbon-carbon double bonds.

The same van der Waals forces that cause CNT fibers to fail are strong enough to compel CNTs to aggregate into bundles making them insoluble in nearly all solvents. Bundling prevents the use of inexpensive, roll-to-roll manufacturing and printing methods for device fabrication. Aggregation is also the cause of low photoluminescence quantum yields of bulk CNTs. Neighboring nanotubes within these bundles enable the transfer<sup>49</sup> and fast relaxation of photoexcited electrons (110 ns lifetime)<sup>31</sup> into lower energy states. The continuum DOS of metallic CNTs, in particular, facilitate faster, non-radiative recombination pathways.<sup>50</sup> Aggregation and poor solubility are also a problem for CNT composites, as they cause uneven distribution of CNTs in polymers. This distribution prevents even load transfer from the matrix to the nanotubes and so generates non-uniform mechanical properties that facilitate the formation of material defects.<sup>30</sup> Dispersion properties are also acknowledged to have a strong effect on electrical percolation threshold values of CNT thin films and polymer composites.<sup>51</sup>

The attraction of CNTs for various applications thus existed on a fundamentally interesting but largely irrelevant scale of the individual nanotube in

terms of practical applications. Researchers wanted to develop these CNTs for device applications without being aware until later that van der Waals forces had a greater impact on the behavior of the bulk material. However, understanding this limitation helps us proceed to successfully translate the properties of individual CNTs to the macroscale. We now understand that even at the bulk level, nanotubes must remain effectively individual to take advantage of the attractive properties related to  $sp^2$  carbon bonding and to avoid the drawbacks of van der Waals forces.

Dispersing CNTs points us in the direction of solution processing methods. Because of the van der Waals aggregation effect, only a few solvents can weakly disperse CNTs with the aid of sonication, including dimethylformamide, N-methylpyrrolidone,<sup>52</sup> and 1,2 dichlorobenzene.<sup>53</sup> However, these nanotube solutions are not thermodynamically stable and flocculate within hours. They are also unable to achieve high CNT concentrations.<sup>52</sup> To overcome this problem, two methods of individually dispersing CNTs have been developed: 1) non-covalent surfactant dispersion and 2) covalent sidewall functionalization. Both of these methods have their pros and cons, though we will learn how the disadvantages of covalent functionalization can be circumvented through controlling the position of functional groups on the nanotube surface.

### *Surfactant Dispersion*

There are many different kinds of surfactants used for individually dispersing CNTs including sodium cholate and sodium dodecylsulfonate (SDS). The best surfactants for this purpose, such as sodium dodecylbenzenesulfonate

(SDBS), tend to include aromatic groups. These groups facilitate pi-pi stacking of surfactant molecules on the CNT surface, improving adsorption.<sup>54</sup> Cavitation forces, created by ultrasonication<sup>55</sup> of CNTs in 1-2 wt% surfactant water solution, generate enough energy to overcome the van der Waals attractions and exfoliate nanotube bundles. This process enables surfactants to adsorb to the exposed individual nanotube surfaces and facilitate the interaction of the CNT with the solvation cage via polar head groups (Figure 1-6A). Subsequent ultracentrifugation removes any remaining nanotube bundles, leaving individual CNTs suspended in solution.<sup>16</sup> In addition to improving solubility, the arrangement of surfactant around the nanotube provides a buffering space between CNTs to prevent optical quenching interactions with metallic nanotubes. Thus CNT photoluminescence properties are a good indicator of the extent of individual nanotube dispersion (Figure 1-6B).<sup>56</sup>

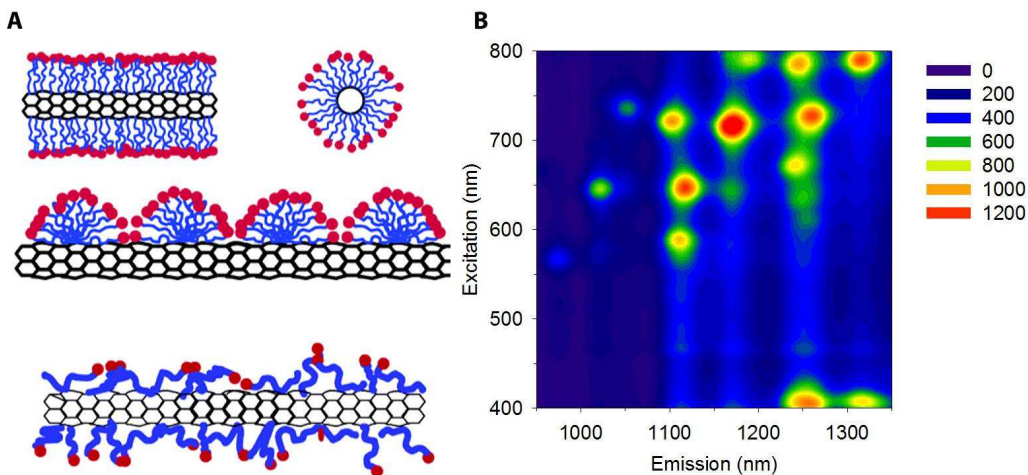


**Figure 1-6.** (A) Potential surfactant adsorption arrangements on a CNT. The surfactant typically features a non-polar tail that interacts with the nanotube and a polar head group to increase solubility as well as aid in dispersion of nanotubes by disrupting van der Waals forces and by electrostatic repulsion.<sup>57</sup> (B) An emission-excitation photoluminescence map of CNT chiralities individually dispersed using the ionic surfactant, sodium dodecylbenzenesulfonate.

The surfactant method of nanotube dispersion enabled the first highly resolved near-IR photoluminescence studies. These studies revealed both the excitonic nature<sup>15</sup> and the chiral dependence of CNT fluorescence behavior.<sup>16,17</sup> Surfactant dispersion has also been used for separation purposes in conjunction with a density gradient to enable the density based sorting of metallic and semiconducting CNTs, SWCNTs and MWCNTS.<sup>42–44,58</sup> Nanotube purities as high as 97% can be achieved using this method, though yields are typically at the  $\mu\text{g}$  level. Scalability could increase with the use of industrial size centrifuges, raising yields to gram levels.<sup>42</sup> However, the use of surfactants and ultracentrifugation ultimately limits scalability and requires excessive sonication. Sonication severs SWCNTs and diminishes their attractive one-dimensional properties.<sup>16,47,59</sup> Surfactants are also difficult to remove completely from the nanotubes,<sup>56</sup> which makes their use problematic for applications that require ultra clean samples, such as electronic circuitry.

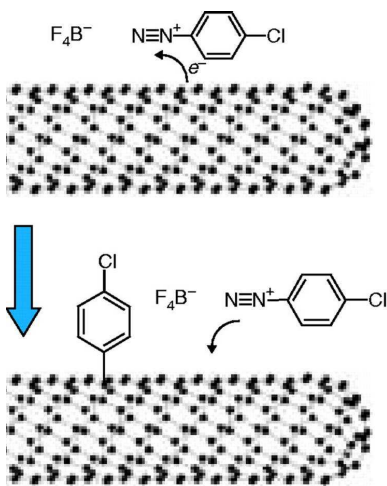


**Figure 1-7.** An example of CNT covalent functionalization by a diazonium salt. This reaction utilizes electron transfer from the nanotube carbon-carbon double-bonds to form a covalent bond, converting the  $sp^2$  hybridized attaching carbon atom to  $sp^3$  hybridization upon single bond formation.<sup>60</sup>

### *Covalent Functionalization Strategies*

As-synthesized and acid purified CNTs can have a range of “native” covalent defects, the concentration or density of which depend on the synthesis and purification method. Acid purified (for the removal of excess amorphous carbon and catalyst impurities), CVD synthesized CNTs have been observed to display an  $sp^3/sp^2$  hybridized defect concentration as high as 1-3%.<sup>61</sup> Without acid processing, arc-discharged CNTs can have 1  $sp^3$  hybridized carbon defect every 100 nm.<sup>62</sup>

However, the benzene-like structure of CNTs also suggests ways to intentionally implant covalent defects using wet chemistries adapted from the extensive, aromatic organic chemistry literature, including the Diels-Alder reaction, Birch reduction, diazonium salts addition (Figure 1-7), Friedel-Crafts acylation, and various cycloaddition reactions.<sup>63,64</sup> These organic sidewall

functional groups can provide a steric buffer between neighboring CNTs to prevent collective van der Waals forces from aggregating the nanotubes, which helps the nanotubes to be more soluble. The yields of some covalent chemistries are better than others, in large part because the aggregation issue must also be taken into account during the chemistry itself – otherwise functionalization will only take place on the exterior of nanotube bundles, leaving interior nanotubes unreacted. This situation makes CNT chemistry particularly challenging, as one must use the correct solvent to create a homogenous solution of individual nanotubes for organic reaction. Although some solvents are successful at dispersing CNTs for organic reaction, these solvents also tend to be harsh oxidizing or reducing media, which prevent their use for device fabrication.

Covalent functionalization may succeed at assisting in the dispersion of CNTs, but there is a significant drawback to this method. Covalent addition to the nanotube sidewall utilizes the reactive pi-bonds, a process that converts the  $sp^2$  hybridized carbon atoms to  $sp^3$ . This process disrupts the extended conjugation of carbon-carbon double bonds and generates scattering sites that largely eliminate conductivity and photon emission, thus removing the highly desirable electric and optical properties of CNTs (Figure 1-8).<sup>65-70</sup> This tradeoff is largely the reason that surfactant dispersions of CNTs have been so highly relied upon despite scaling limitations. However, as covalent functionalization is the only dispersion method with any real scalability, this tradeoff needs to be circumvented in order to make practical CNT applications possible.

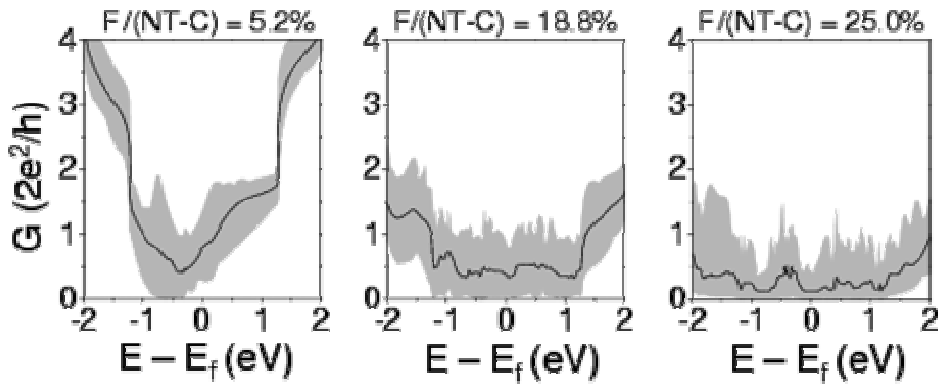
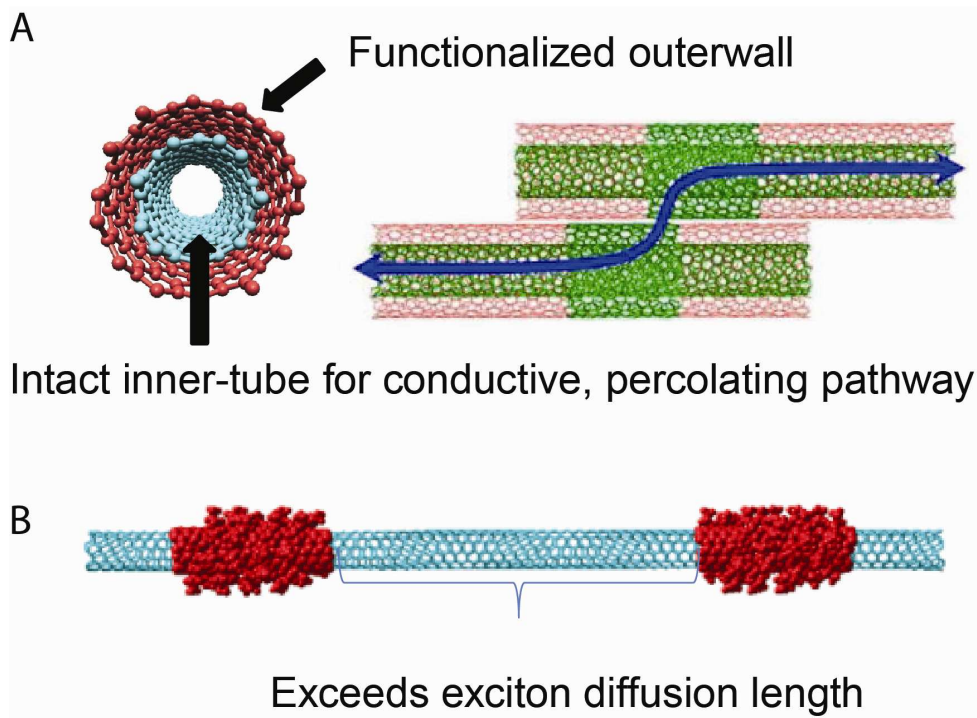


**Figure 1-8.** Calculated CNT conductance as a function of energy near the Fermi level dramatically decreases with increasing carbon atom functionalization. Here a (6,6) metallic CNT modeled using the Hückel approximation is modified by increasing fluorine atom covalent sidewall addition. At a F/C ratio of 25%, conductance is almost completely lost.<sup>65</sup>

While previous research had suggested that covalent functionalization is highly detrimental to CNT properties, our studies have shown that not all CNT covalent defects are equivalent. The impact of a defect on any material must be considered in relation to the lifetime and distance traveled of the fundamental particles (including charge carriers, excitons, and phonons) the defect may be disrupting. The extended crystalline structure of CNTs means that the distance traveled and number of carbon atoms visited by these particles can be substantial. For example, excitons are known to diffuse for up to 90 nm on the CNT before decaying, visiting up to 10,000 carbon atoms during their lifetime.<sup>69</sup> Therefore, defects in the nanotube structure within 90 nm of the exciton generation point can scatter these excitons and quench photoluminescence.

However, if defects are at low density on the CNT surface (i.e. greater than 90 nm apart) then there is a higher probability of radiative recombination of the exciton before it can be quenched by these functional groups. Thus, while the absolute number of covalent defects on a CNT can adversely affect its properties,

the distribution of these defects may be of even greater importance in determining the degree of perturbation. Given this knowledge, we aim to circumvent the tradeoff of dispersion and functionality of covalently functionalized CNTs by controlling the locations of functional groups so as to minimize the disruption of excitons and electrons. In this manner, we can facilitate the retention of photoluminescence and conductivity respectively.



**Scheme 1-1.** Schematic strategy of positionally controlled CNT covalent functionalization to avoid the tradeoff of desirable properties that are linked to  $sp^2$  carbon atoms. (A) The outer-walls of DWCNTs are functionalized to enhance individual dispersion and prevent detrimental aggregation effects, while the inner-tube is protected from functionalization and thus retains conductive properties for lower percolation thresholds. (B) Functionalized SWCNTs are able to retain functionality while improving dispersion properties by limiting the covalent addition to discrete bands (shown in red), leaving regions of the nanotube intact that are longer than the exciton diffusion length to minimize exciton quenching.

Keeping in mind the effects of defect density and location on CNT properties, we have devised two strategies of spatially selective CNT covalent

functionalization with the aim of diminishing the scattering effects on electrons, holes and excitons to minimize the detriment to electric and optical properties (Scheme 1-1). The first method is called “outer-wall selective functionalization” and utilizes DWCNTs as a reactive medium. Selectively functionalizing the outer-most graphitic wall improves dispersion, but it also protects the inner-tubes from reaction which enables retention of conductivity due to the maintenance of its delocalized, pi-electron network (Scheme 1-1A).

The second strategy involves spatial confinement of functional groups on the CNT surface in discrete “bands” that leave intact regions of the graphitic surface which are longer than the exciton diffusion distance, thus enabling unperturbed exciton generation and diffusion to avoid encounter with a defect before radiative decay. This functional morphology allows photoluminescence to occur even after covalent functionalization (Scheme 1-1B). We have determined that this positional control of functional groups is made possible due to the defect propagative mechanism of a Birch-reduction-based chemistry when applied to CNTs.<sup>71</sup>

Precise control of functional modification of any nanomaterial is difficult to accomplish without the use of lithographic techniques. Such methods can be cumbersome and difficult to scale up. As with most nanomaterials, scalability is an issue with CNTs, but the highly controlled covalent chemistries we have developed can be easily scaled to bulk magnitudes due to the use of reaction solvents that spontaneously exfoliate CNT bundles by electrostatic repulsion

(superacid protonation, or sodium-liquid ammonia reduction). Thus, we can ensure that the reaction takes places on individual nanotubes.

### *New Optical Properties of Functionalized CNTs*

In addition to maintaining desirable CNT properties by controlling the location and effective density of covalent functional groups attached to the graphitic surface, we have also discovered that the same chemistry can engender new optical behaviors that are indicative of a defect dependent doping effect that generates CNT trion photoluminescence. Covalent functionalization of CNTs generates defects within the extended carbon lattice structure that are manifested as intra-bandgap defect states due to splitting of the excited and ground states.<sup>72,73</sup> These new electronic states are optically active and appear as a new photoluminescence peak that is redshifted from the native, chirality-dependent emission in the near-IR range.<sup>72,73</sup> However, when such a covalent defect is generated in the presence of highly reducing or oxidative chemistry, this defect state can trap excess electrons or holes.

When a photogenerated exciton diffuses to a doped defect site, a quasi-particle called a trion is formed. Trions are charged excitons that were theoretically predicted in semiconductors in the 1950s,<sup>74</sup> but were not experimentally observed until the synthesis of quantum confined materials such as quantum dots.<sup>75,76</sup> Only the Coulombic attractive force in low dimensional materials is strong enough to increase the binding energy of the extra carrier relative to the neutral exciton species to enable enough of a redshift in the emission spectrum to be resolved from the exciton radiative signature.<sup>77</sup> This

unique ability of CNT defects to activate trions results in a total of three simultaneous photoluminescence emissions from a single covalently functionalized CNT (native, defect, and trion) and is unprecedented in the CNT literature.

Instead of eliminating photoluminescence after covalent functionalization, carefully controlled addition of functional groups can in fact retain and even create new photoluminescence peaks. These peaks are further redshifted into the near-IR than the unperturbed CNT signatures. Near-IR photoluminescence is of interest for bio-imaging purposes, as biological tissue does not absorb strongly in the 1000-1400 nm range.<sup>19,78</sup> With this chemistry, we are able to achieve both CNT excitation and emission within this window while maintaining excellent dispersion properties that are essential for biocompatibility.<sup>79</sup>

The following chapters will discuss these covalent chemistries and how the corresponding reaction mechanisms allow us to control the location of functional groups on the CNT surfaces in a way that enables both retention and generation of desirable nanotube properties. The chemistries we study generally incorporate highly reducing or oxidative solvents to ensure scalable reaction on individual nanotubes. Functionalized samples are characterized either as-is or after subsequent re-dispersion using 1wt% SDBS in deuterium oxide for optical studies. Thermogravimetric analysis (TGA) and Raman spectroscopy are used in conjunction with absorption spectroscopy to characterize the degree of CNT covalent functionalization. Transmission and scanning electron microscopies provide fundamental information regarding the surface functional morphology.

CNT thin films were used exclusively to characterize electronic properties. Photoluminescence reveals how optical activity is retained or modified after covalent functionalization as well as providing a measure of the nanotube dispersion.

We hope this study of CNT covalent addition will prompt new thinking on functionalization of graphitic materials, which suffer from similar processing issues. We will begin with our study of outer-wall-selectively oxidized DWCNTs to demonstrate the concept of selective and locational control of functionalization for such graphitic systems.

## Chapter 2: Outer-Wall-Selectively Oxidized, Water soluble Double-Walled Carbon Nanotubes

*Adapted from Brozena, A. H.; Moskowitz, J.; Shao, B.; Deng, S.; Liao, H.; Gaskell, K. J.; Wang, Y. *J. Am. Chem. Soc.* **2010**, 132, 3932–3938.<sup>80</sup>*

*A.H. Brozena performed all the Raman spectroscopy, the TEM imaging and directed some synthesis. J. Moskowitz, B. Shao, and S.L. Deng synthesized the majority of the samples and characterized the water solubility of these materials. H. Liao constructed the nanotube length histograms, as well as the carbon nanotube thin films and characterized their conductivity. K. Gaskell took and analyzed the XPS data.*

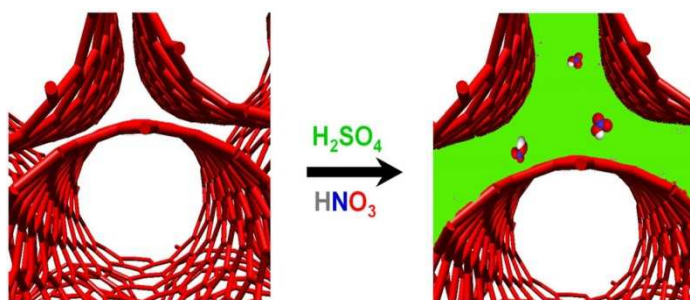
### Introduction

Single-walled carbon nanotubes combine remarkable electrical, mechanical, thermal, and optical properties,<sup>3,81</sup> yet their lack of solubility in conventional solvents is a serious drawback to applications in a number of important areas, including composite materials,<sup>22,82</sup> biomedicine,<sup>24</sup> and solar cells.<sup>25,83</sup> The insolubility is due to the inert graphitic nature and strong inter-tube van der Waals interactions.<sup>47,84</sup> Over the past decade, enormous efforts have been devoted to addressing this insolubility problem.<sup>16,47,59,64,85</sup> The most successful approaches to date have involved either covalent sidewall functionalization chemistry<sup>64,85</sup> or non-covalent processes that rely on the use of surfactants or polymers to form kinetically stable suspensions.<sup>16,47,59</sup> However, choosing between covalent and non-covalent approaches involves an unattractive trade-off. Non-covalent approaches typically suffer from large amounts of surfactant/polymer contamination, low yields, and limited scalability.<sup>16,47,59</sup> Covalent sidewall chemistries can overcome these problems and effectively

render SWCNTs soluble in thermodynamically stable solutions.<sup>64,85</sup>

Unfortunately, covalent chemistry dramatically alters the atomic and electronic structures of SWCNTs,<sup>65</sup> causing the loss of the electrical properties<sup>60</sup> and the degradation of their mechanical strength and chemical stability.

Here we report outer-wall selectively oxidized double-walled carbon nanotubes (*oso*-DWCNTs), a promising material to address this insolubility problem. DWCNTs are a class of carbon nanostructures composed of exactly two graphene sheets that are rolled into concentric tubes. A series of recent studies have shown that DWCNTs exhibit a range of interesting electrical,<sup>86</sup> thermal,<sup>87</sup> and mechanical properties,<sup>88</sup> that are sometimes superior to those of SWCNTs. By adapting an acid oxidation chemistry previously used on SWCNTs,<sup>89,90</sup> we have demonstrated outer-wall selective oxidation of DWCNTs to the exclusion of the inner-tubes. This “double-wall” chemistry produces water-soluble materials that preserve the electrical properties of the inner-tube.



**Scheme 2-1.** Illustration of outer-wall selective oxidation of DWCNTs by  $\text{H}_2\text{SO}_4/\text{HNO}_3$ .  $\text{H}_2\text{SO}_4$  intercalation opens the diffusion pathways for  $\text{HNO}_3$  to access nanotubes embedded in a rope and selectively react with the exposed outer-walls. For clarity, the inner-tubes are omitted.

DWCNTs were dispersed in oleum (100%  $\text{H}_2\text{SO}_4$  with excess  $\text{SO}_3$ ) and then reacted with nitric acid to afford *oso*-DWCNTs that are highly soluble in

water. Over 70% of DWCNTs became soluble in water with a yield of better than 70% from the starting material. Unlike conventional organic covalent chemistry or gas-phase reactions,<sup>85</sup> the intercalation of oleum between bundled nanotubes<sup>28,91</sup> presumably opens diffusion pathways for the HNO<sub>3</sub> to equally access all outer-wall surfaces (Scheme 2-1). We believe this intercalation diffusion mechanism allows the reaction to occur homogeneously at high concentrations. The diffusion mechanism may also include epoxidation<sup>92,93</sup> of the bundled DWCNT ends with the potential for these groups to migrate across the surface. However, the rate of epoxide migration calculated by density functional theory is only 10<sup>-2</sup>/s at room temperature<sup>93</sup> and is therefore not considered to be the major contributor of DWCNT oxidation in this experiment. In-situ formation of the nitronium ion after addition of HNO<sub>3</sub> to the oleum-DWCNT solution is believed to form the positively charged carbon nanotube-nitronium adduct. Upon 1,3 or 1,5 addition of the sulfate anion to the remaining positively charged carbon site<sup>94</sup> could result in the formation of the epoxide upon loss of the SO<sub>3</sub> and the NO<sub>2</sub> species. Post functionalization water workup could lead to the formation of hydroxide functionalities. Research has established that oxidation tends to “cut” the nanotubes at sites of pre-existing defects rather than oxidatively shortening the nanotubes from the ends in a fuse-burning mechanism.<sup>95</sup>

The functionalized DWCNTs were characterized with Raman spectroscopy, UV-Visible spectroscopy, X-ray photoelectron spectroscopy (XPS), and high resolution TEM. Our results reveal strong correlations of solubility and the degree of functionalization with the relative reactant concentration and

reaction time. We have also determined optimized reaction conditions for outer-wall selectivity. Outer-wall selectivity is essential to retain the electrical conductivity of *oso*-DWCNT thin films by maintaining efficient inner-tube pathways that are absent in functionalized SWCNT films. These results demonstrate a possible solution to the covalent-modification tradeoff between water-solubility and the desirable electrical properties associated with these CNTs.

## Materials and Methods

### *Outer-wall Selective Oxidation of Superacid Intercalated DWCNTs*

50 mg of raw DWCNTs (Unidym DW411UA) were added to 50 mL oleum (reagent grade, 20% free SO<sub>3</sub> basis, Sigma Aldrich) (*Warning: oleum is very corrosive and should be treated with caution*) in a three-necked flask. The spontaneously formed black, homogeneous solution was stirred for 24 hrs under an argon atmosphere to ensure complete intercalation by oleum, after which the dispersion was heated in a water bath to 65 °C. 1-20 mL of 70% HNO<sub>3</sub> (Certified ACS Plus, Fischer Scientific) was added to the solution drop by drop through an addition funnel (*Warning: nitric acid is extremely corrosive and should be treated with caution*). The solution was left to react for 2-24 hrs. The conditions investigated included a 2 hours reaction time with added nitric acid volumes of 1 mL, 5 mL, 10 mL and 20 mL. Additional conditions included reacting with 5 mL of nitric acid for 2 hrs, 12 hrs, and 24 hrs. This fixed 5 mL reactant volume was chosen to avoid immediate over-oxidation of the sample, allowing the reaction to be studied over longer periods of time than if a 10 mL fixed volume were chosen.

When the desired reaction time was reached, the solution was removed from the warm bath and left to cool in air for 10 minutes. The black slurry was slowly added into 250 mL of nanopure water ( $18.2\text{ M}\Omega$ ), using a glass stir rod to prevent splashing. The diluted DWCNT solution was vacuum filtered and then washed with 100 mL of diethyl ether and 50 mL of methanol. Finally, the DWCNTs were washed with 1 L nanopure water to ensure that the DWCNTs were acid free. The solids were placed in a vacuum oven at  $80\text{ }^{\circ}\text{C}$  for 12 hrs to dry. These experimental procedures ensured that the samples were free of the chemical doping effects that can be caused by acids.<sup>96</sup>

#### *Relative Solubility of Oxidized DWCNTs Prepared at Different Reaction Conditions*

In order to determine which oxidative conditions (in terms of reactant concentration and reaction time) resulted in the most soluble sample, a hexane and water extraction procedure was developed to separate the water soluble and insoluble DWCNTs. 3.0 mg of each oxidized DWCNT sample was sonicated using a Misonix S-4000 ultrasonicator at  $\sim 115\text{ W}$  in 18 mL basic (pH~9) nanopure water ( $18.2\text{ M}\Omega$ ) for 25 min. 7 mL of hexane (99.5%, Pharmco-AAPER) was then added to the water dispersion and shaken by hand in a sealed vial. After 25 minutes, the mixture phase separated into two distinct layers with water soluble DWCNTs on the bottom aqueous layer. The concentration of the functionalized DWCNTs that were water soluble was determined by absorbance of the aqueous solution, which was measured using a Perkin Elmer 1050 UV-Vis-NIR spectrophotometer. The concentration was determined optically at  $\lambda=500\text{ nm}$

from absorbance vs. concentration working curves of raw DWCNTs dispersed in nanopure water using 1 wt% SDS.

#### *Determining Maximum Water Solubility of Oxidized DWCNTs*

To find the maximum water solubility, 16.6 mg of the oxidized DWCNT sample was dispersed in 10 mL NaOH aqueous solution (pH~10) and sonicated at ~115 W for 1 hr in circulated cooling water bath. 1 mL of the dispersed solution was added to three centrifuge tubes each, which were then centrifuged at 2800 g for 60 minutes. After centrifugation, 0.10 mL of the top layer solution was taken from each vial and diluted 80 times. The UV-Vis-NIR spectra were taken for each of the diluted solutions. This centrifugation and absorbance measurement procedure was repeated for the remaining 0.90 mL dispersions in each centrifuge tube under the same conditions for a total of 5 times, after which the UV-Vis-NIR spectra did not change. The dispersion was then expected to be at its most stable state, in which the maximum solubility of the functionalized DWCNTs was calculated by the aforementioned optical method.

#### *X-ray Photoelectron Spectroscopy*

XPS data were collected on a Kratos Axis 165 operating in hybrid mode using monochromatic Al K $\alpha$  radiation (1486.6 eV) at 240 W. The samples were mounted on double sided carbon tape and the pressure of the instrument remained below  $1 \times 10^{-8}$  Torr throughout the data collection. Survey spectra were collected at a pass energy of 160 eV while high resolution spectra were collected at a pass energy of 20 eV. All peaks were calibrated to the sp<sup>2</sup> hybridized peak at 284.5 eV,

and after the application of a Shirley background,<sup>97</sup> fit with peaks with a 70% Gaussian 30% Lorentzian product function. The graphitic peak was modified with an asymmetric form A(0.4,0.55,30)GL(30) determined through fitting of the pristine nanotube C 1s spectrum, using CasaXPS software.

### *Raman Spectroscopy*

Raman scattering data were collected on a Horiba Jobin Yvon LabRAM HR800 Raman microscope using 632.8, 514.5 and 488.0 nm excitation lines. The non-partitioned samples of the DWCNTs (including both water soluble and insoluble fractions) were dispersed in ethanol by brief sonication to improve uniformity and deposited drop-wise on a glass microscope slide using a Pasteur pipette and allowed to dry. Spectra for each sample were obtained by measuring the Raman scattering at three separate spots and averaging.

### *Electron Microscopy*

TEM images of the 5 mL 24 hrs and 10 mL 2 hrs samples were obtained using a JEOL JEM-2100 LaB6 transmission electron microscope at 200 kV accelerating voltage. High resolution images were taken on a JEOL JEM 2100 FEG transmission electron microscope at the same accelerating voltage. Non-partitioned DWCNT samples were washed with nanopure water to protonate surface carboxylic acid functional groups and then dispersed in ethanol. These solutions were then briefly sonicated and deposited on an SPI lacey carbon coated 300 mesh copper grid using a Pasteur pipette.

Length distributions of the raw, 5 mL 24 hrs and 10 mL 2 hrs samples were measured based on images taken on a Hitachi SU-70 SEM at 3kV accelerating voltage. The raw DWCNT sample was first dispersed in 1,2-dichlorobenzene and spin-coated on a silicon wafer at 3000 rpm. The 5 mL 24 hrs and 10 mL 2 hrs samples were re-suspended in ethanol, followed by deposition on a silicon wafer by spin-coating. The images were then analyzed using ImageJ software.

#### *Carbon Nanotube Thin Film Conductivity Measurements*

Functionalized DWCNT samples and HiPco SWCNT controls<sup>98</sup> (received as a gift from Rice University) were weighed and re-suspended in ethanol by sonication to form a 0.20 mg/mL solution. The oxidized SWCNT sample was functionalized at the same conditions as the 10 mL 2 hrs DWCNT sample. The solution was filtrated through a 0.2 $\mu$ m GTTP Isopore<sup>TM</sup> Membrane (Millipore) to form a thin film. The thin film was cut into 0.20-0.32 cm wide strips. Electrodes (5 nm Cr/50 nm Au) were deposited on the strip through a shadow mask using thermal evaporation (Metra Evaporator, Metra, Inc) to form a 0.50 cm long conducting channel. Resistances were measured with a multimeter. The film thickness was estimated using the film area and density (1.3 g/cm<sup>3</sup>).

## **Results and Discussion**

#### *Outer-wall Selectivity*

Raman, XPS and water solubility data clearly indicate the successful functionalization of the DWCNT samples, but most interesting was the evidence

of outer-wall selectivity. Figure 2-1 shows Raman spectra of the oxidized DWCNTs under different reaction conditions. The most pronounced Raman signatures of a DWCNT arise from scattering by the radial breathing modes (RBMs) in the range 100-350 cm<sup>-1</sup> and sp<sup>2</sup> hybridized carbon tangential modes around 1500-1600 cm<sup>-1</sup>, which are collectively known as the G band.<sup>28</sup> Oxidation introduces sp<sup>3</sup> centers and other structural defects, which give rise to the so-called D band around 1350 cm<sup>-1</sup>.<sup>99</sup> Importantly, due to relatively weak inter-wall interactions within a DWCNT, each of the two constituent walls gives a different set of Raman peaks.<sup>35</sup> In particular, the inner-tube and the outer-wall have distinct RBMs because the low frequency Raman shifts are inversely proportional to the nanotube diameter.<sup>99,100</sup> We attributed the raw-DWCNT peaks at approximately 150 cm<sup>-1</sup> and 215 cm<sup>-1</sup> to the RBMs of the outer-walls and inner-tubes, respectively. After oxidation, the peaks centered around 150 cm<sup>-1</sup> were depressed. However these same samples retain the peaks centered around 215 cm<sup>-1</sup>, corresponding to the inner-tubes of the DWCNTs. The retention of the inner-tubes' RBMs and the simultaneous disappearance of those of the outer-walls strongly suggest high outer-wall selectivity of this intercalation oxidation chemistry.

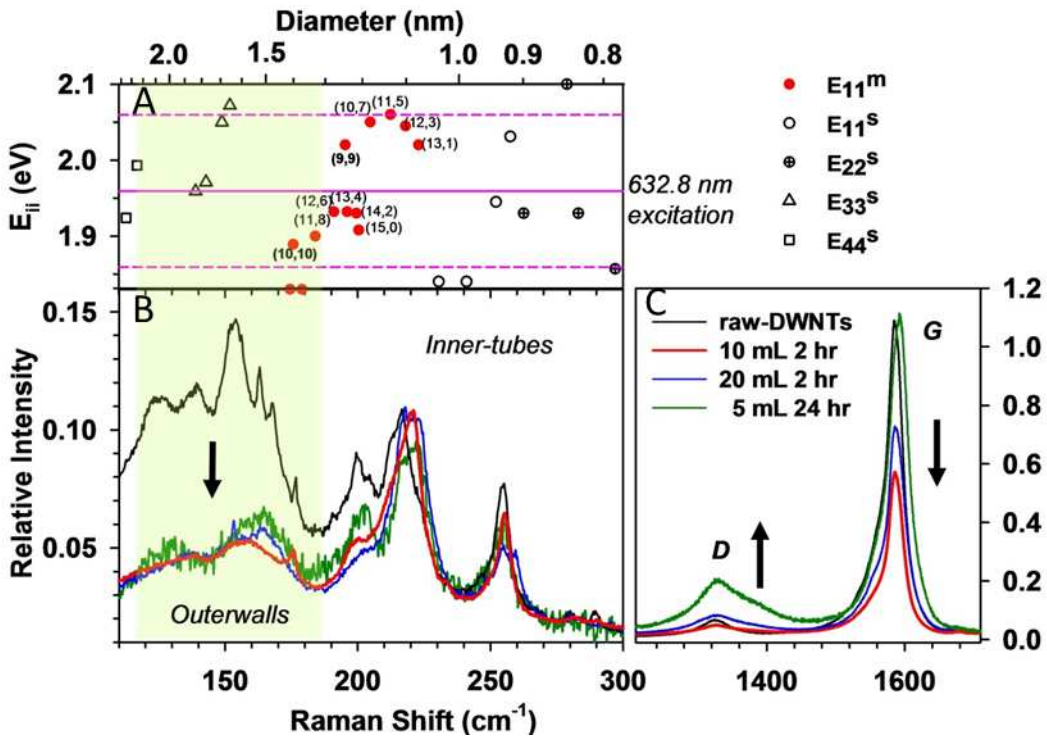


**Figure 2-1.** Raman spectral evidence for outer-wall selectivity. Raman spectra of the oxidized DWCNTs under different reaction conditions (red line: 10 mL HNO<sub>3</sub> 2 hrs; blue line 20 mL 2 hrs; green line: 5 mL 24 hr) are plotted in comparison with that of raw DWCNTs (black line). (A) The metallic inner tubes (red circles) are indicated by the above Kataura plot, where the excitation window of the laser used ( $\lambda=632.8 \text{ nm}$ ) is indicated by the two dotted lines. (B) The intensities were normalized to the peak centered at  $215 \text{ cm}^{-1}$ . The shaded area is dominated by outer-walls. (C) The G peak (sp<sup>2</sup> hybridized carbon) decreases and the D peak (sp<sup>3</sup> hybridized carbon) increases with increasing functionalization degree by the shown oxidation conditions.

Using an experimental Kataura plot which correlates electronic transitions and the RBM modes,<sup>31-33</sup> we can assign the majority of the inner-tubes within the Raman resonance window of the laser excitation line used (632.8 nm) to metallic CNTs. Similar trends were observed with 514.5 nm and 488.0 nm excitation wavelengths, which are resonant with different populations of CNT chiralities (Figure 2-2). Since the Kataura plot was constructed from Raman data on SWCNTs with a wide range of diameters (0.7-2.3 nm)<sup>101-103</sup> and the three laser

excitation lines together sampled a large population of different nanotube structures, the outer-wall selectivity is likely a general phenomena of DWCNTs reacted under the intercalation oxidation conditions investigated. Metallic selectivity has important implications for the use of *oso*-DWCNTs for electronic applications and will be discussed further below.

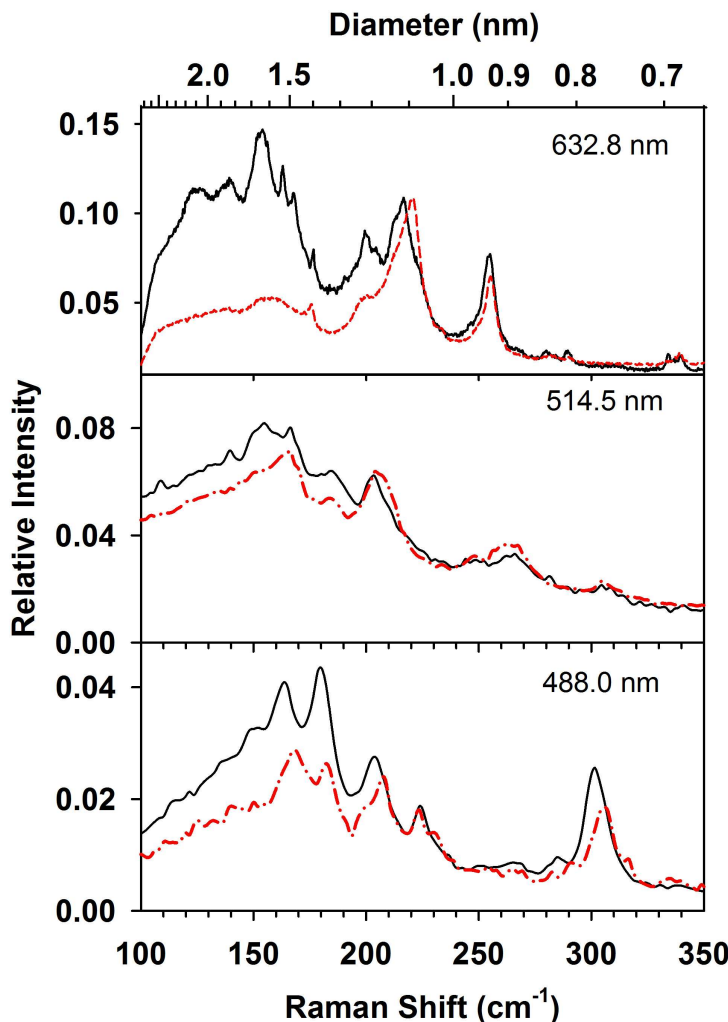


**Figure 2-2.** Raman spectra of the 10 mL 2 hrs sample in comparison with raw DWCNTs. Outer-wall selectivity is evident by the diminishing of the outer-wall RBMs and retention of those of the inner-tubes. The excitation line is indicated in each spectrum.

The disappearance of the outer-wall RBMs correlates with the simultaneous decrease of the G band ( $\sim 1585 \text{ cm}^{-1}$ ) and the rise of the D band

( $\sim 1350$   $\text{cm}^{-1}$ ), the latter of which occurs due to the increased outer-wall functionalization. The integrated ratio of the disorder and the graphene vibrational modes (D/G ratio) directly indicates the degree of DWCNT functionalization. Additionally, the higher the ratio of the inner-tube RBM intensity to the G band, the higher the outer-wall selectivity (Figure 2-1).

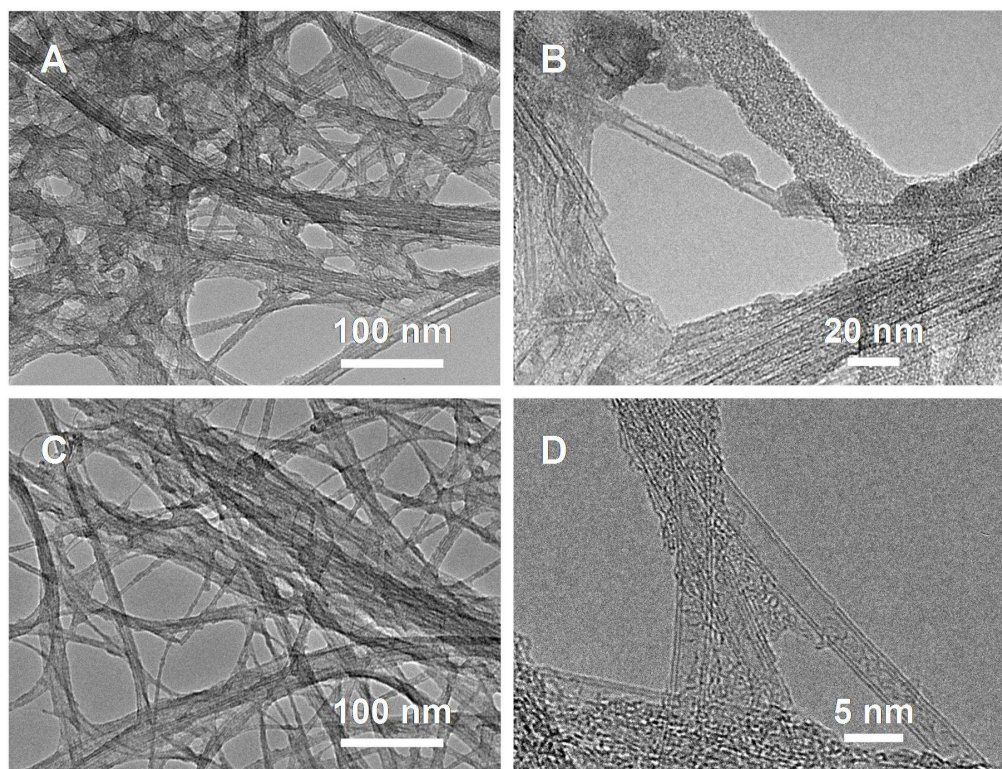


**Figure 2-3.** Comparative TEM studies of *oso*-DWCNT samples with the highest water solubility (A,B: 5 mL 24 hrs) and the highest outer-wall selectivity (C,D: 10 mL 2 hrs). These images show two contrasting oxidation products: (A,B) shortened nanotubes with amorphous carbon coating; (C,D) long, exfoliated nanotube bundles with clean wall structures.

To confirm the outer-wall selectivity, high resolution TEM was performed on the 10 mL 2 hrs sample, which had the highest outer-wall selectivity according to the RBM/G band ratio, and the 5 mL 24 hrs sample, which had the highest D/G

ratio among the eight reaction conditions investigated. Consistent with the higher Raman D/G ratio, TEM images of the 5 mL 24 hrs sample revealed etched holes on the nanotube sidewalls, and shortened nanotubes with some amorphous carbon coating as a result of over oxidation (Figure 2-3A and B). The results from the 10 mL 2 hrs sample demonstrated intact inner-tubes with an absence of the roughness associated with the oxidized outer-walls (Figure 2-3C and D). This outer-wall surface morphology is a result of  $sp^2$  hybridized carbon atoms converting to pyramidalized  $sp^3$  by oxidation. The structural contrast between inner-tubes and outer-walls further supports the conclusion drawn from the Raman data that oxidative functionalization occurred primarily on the outer-wall.

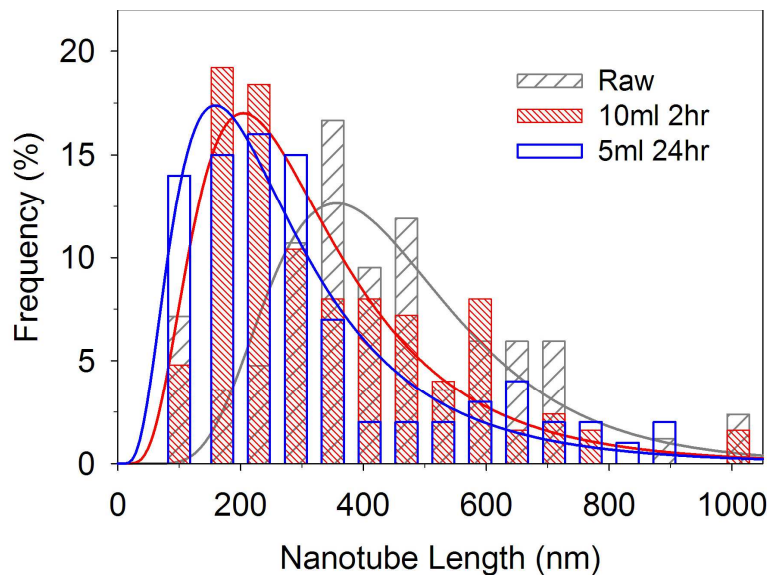


**Figure 2-4.** Length distribution of raw, 10 ml 2 hrs, 5 ml 24 hrs samples. Approximately 100 nanotubes were samples for each histogram. The distributions are fitted with log-normal functions.

Length distributions of the samples were quantified using a combination of SEM and the imaging software, ImageJ. Raw, non-oxidized DWCNTs featured an average length of  $502 \pm 341$  nm, while the 10 mL 2hrs and 5 mL 24 hrs samples

were  $361 \pm 277$  nm and  $305 \pm 250$  nm, respectively. The length distributions for all three samples followed log-normal distribution functions (Figure 2-4). Therefore, the 5 mL 24 hrs sample had undergone greater oxidative shortening than the 10 mL 2 hrs sample, which is consistent with the TEM images.

The outer-wall selectivity can be attributed to the physical protection of the inner-tube by the outer-wall<sup>104,105</sup> and to the deliberately controlled reaction conditions. The high aspect ratio of the one-dimensional structure ( $>1,000$ ) can significantly slow the diffusion of the reagents into the inner-tubes and thus retard the endohedral reaction pathway.<sup>106</sup> Although there are few studies on DWCNT chemistry, it is reasonable to suspect that sulfuric and nitric acids anions can diffuse into the inner-tubes due to their smaller sizes than the opening of the nanotubes. However, the intercalation by oleum opens diffusion pathways for  $\text{NO}_3^-$  to access the outer-wall surface more readily. This mechanism enables a more homogeneous reaction compared with fluorination<sup>105</sup> or nitric acid alone.<sup>107</sup> The chemistry is straightforward and highly scalable, as it eliminates an initial step involving dispersion by surfactants or organic solvent<sup>85</sup> and allows for homogeneous reactions at high nanotube concentrations.

Functional groups are carboxylic acids as shown by high resolution XPS data. The C 1s spectrum for the raw DWCNTs shows a dominant peak due to  $\text{sp}^2$  hybridized carbon (~284.5 eV). After oxidation, the content of  $\text{sp}^3$  carbon increases and two new peaks at ~289.0 eV and ~285.0 eV appeared, which can be attributed to  $-\text{COOH}$  (~ 6.5% of total carbon signal) (Figure 2-5). Consistent with this assignment, examination of the O 1s region reveals a large increase in oxygen

concentration for the oxidized DWCNTs as compared to the starting material. The peaks for C-O (~533.5 eV) and C=O (~531.9 eV) have a 1:1 area ratio that matches the stoichiometry of the carboxylic acid group (Table 2-1). The appearance of these surface functional groups after oxidation explains the increased solubility of the DWCNTs.

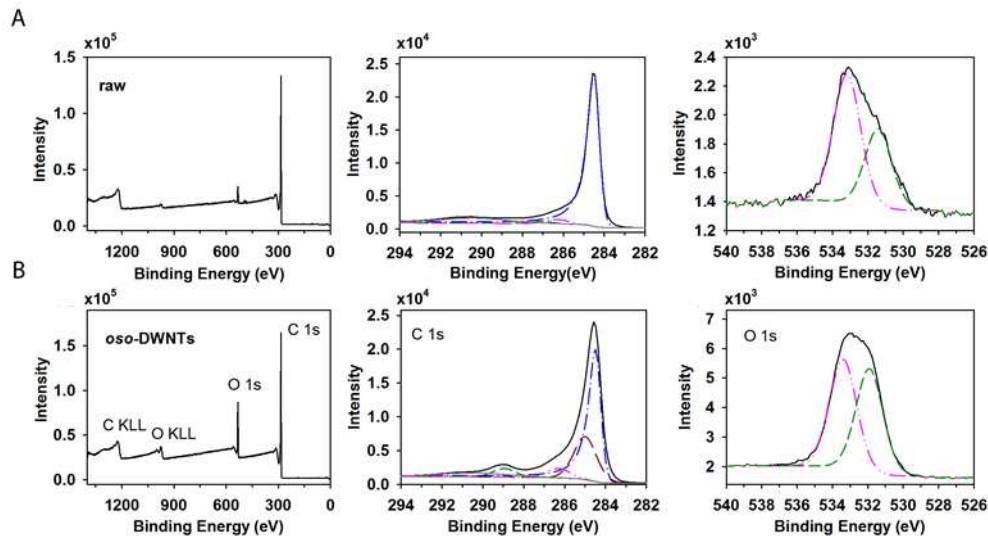


**Figure 2-5.** XPS of (A) raw DWCNTs and (B) 10 mL 2 hrs sample.

Sample	Binding Energy (eV) C 1s (%)						Binding Energy (eV) O 1s (%)	
	sp <sup>2</sup> C <sup>1</sup>	sp <sup>3</sup> C <sup>1</sup>	C-O <sup>1</sup>	C=O <sup>1</sup>	COOH	π- π* <sup>1</sup>	C-O	C=O
Raw DWCNTs	284.5 (77.0)	-	286.3 (4.6)	287.1 (2.4)	-	290.4 (16.0)	533.2 (62.0)	531.3 (38.0)
5 mL 24 hrs DWCNTs	284.5 (48.7)	285.0 (27.5)	286.3 (8.0)	287.1 (1.8)	289.1 (7.3)	290.4 (6.8)	533.7 (50.9)	532.2 (49.1)
10 mL 2 hrs DWCNTs	284.5 (44.5)	285.0 (31.4)	286.3 (8.6)	287.1 (1.5)	289.0 (5.5)	290.4 (8.0)	533.4 (51.1)	531.9 (48.9)

**Table 2-1.** XPS data for raw DWCNTs, 5 mL 24 hrs and 10 mL 2 hrs samples. The oxidized DWCNT samples show a rise of oxygen containing functional groups consistent with carboxylic acids.

<sup>1</sup>Binding energy fixed as determined from fitting of raw DWCNTs.

### *Oso-DWCNT Solubility*

The samples' solubility was further investigated as a function of reactant concentration and reaction time by following the product with UV-Visible absorption and Raman spectroscopies. Because the oxidized nanotubes are soluble in water, a solvation competition between water and an organic solvent, such as hexane, enables separation of water soluble nanotubes from the more hydrophobic components. Figures 2-6A and 2-6D show photographs of the partitioned DWCNT samples (3.0 mg each) in 18 mL basic water and 7 mL hexane after being oxidized at different reaction conditions. The darkness of the aqueous layer correlates with an increase in the percentage of nanotubes dissolved. The percentage of water soluble nanotubes, or relative solubility, at each experimental condition was further quantified by measuring the absorbance of the aqueous layer against an absorbance-concentration working curve. The expected solubility trends were observed. When reaction time was held constant (2 hrs), solubility increased with reactant concentration (1 mL, 5 mL, 10 mL, 20 mL) (Figure 2-6B). When reactant concentration was held constant (5mL), solubility increased with reaction time (2 hrs, 12 hrs, 24 hrs) (Figure 2-6E). Consistent with the solubility trends, the Raman D/G ratio increases with increasing amount of nitric acid in addition to increasing reaction time (Figure 2-6C and 2-6F). These trends were observed as a result of increased oxidative functionalization of the DWCNT samples with either increasing reactant concentration or reaction time.

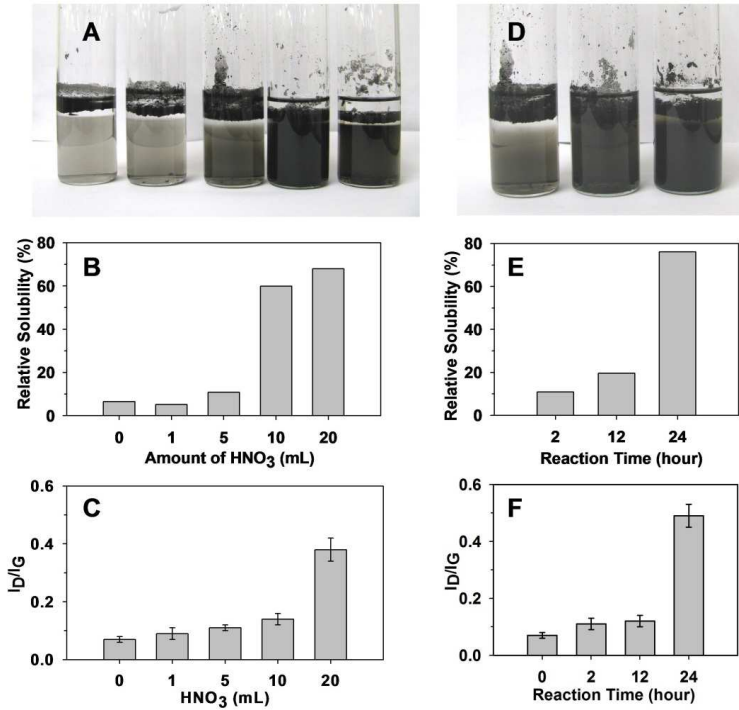


**Figure 2-6.** Relative water solubility and degree of functionalization of oxidized DWCNTs (A-C) under increasing amount of HNO<sub>3</sub> at a fixed reaction time of 2 hrs and (D-F) increasing reaction time using 5 mL HNO<sub>3</sub>. (A, D) Solvation competition of oxidized DWCNTs in water and hexane. The partitioned samples are shown in order as they appear in the solubility graphs below each image. (B, E) Relative solubility: percent of functionalized DWCNTs dissolved in water. (C,F) Degree of functionalization based on Raman I<sub>D</sub>/I<sub>G</sub> of DWCNT samples.

The maximum relative solubility was achieved by reacting the DWCNTs with 5 mL of nitric acid over 24 hrs. 76% of the DWCNTs in this sample dissolved in basic water compared to 68% for the second most soluble sample (20 mL 2 hrs). The maximum solubility, from the 5 mL 24 hrs sample, was 760 mg/L. The solubility for the 10 mL 2 hrs sample, which shows higher outer-wall selectivity, was 600 mg/L as calculated from the relative solubility with respect to the 5 mL 24 hrs sample. High solubility is crucial for potential applications of carbon nanomaterials in a number of areas, especially biomedical applications,<sup>24</sup> composites<sup>108</sup> and solar cells.<sup>25,109</sup> A high density of carboxylic acid groups on the

nanotube sidewall will also offer a large number of covalent anchoring points for further material modification. This feature is important for improving solubility and load transfer.<sup>3</sup>

We note that the maximum solubility may not correspond with the highest outer-wall selectivity. While the maximum solubility was observed for samples reacted with 5 mL HNO<sub>3</sub> for 24 hrs, the highest outer-wall selectivity was achieved at reaction conditions of 10 mL HNO<sub>3</sub> for 2 hrs. This condition mismatch is not surprising since extended reaction time and aggressive reaction conditions tend to produce more functional groups until the nanotube decomposes or each carbon is converted from sp<sup>2</sup> hybridization to sp<sup>3</sup>, which results in higher solubility. However, the extreme condition also involves oxidation of the inner-tubes, which leads to an overall loss of the desirable electronic and optical properties associated with an sp<sup>2</sup> hybridized network of carbons of a pristine inner-tube. Therefore, it is important to balance these competing factors in order to achieve the highest outer-wall selectivity simultaneously with the highest water solubility. Although our experiments have yet to exhaust the parameter space, the trends we have observed could serve as a useful guide for tuning the reaction conditions for intended applications.

### *Improved Conductivity Percolation of Oso-DWCNTs*

The ability to solubilize metallic nanotubes without causing disruption of their electronic structures opens opportunities to investigate the properties and facilitate applications of metallic nanotubes. Wiring nanostructures with effective electrical contact and percolation is a central challenge in conductive composites,

electrical energy storage, and photovoltaic nanoscience.<sup>22,25,81,82</sup> Remarkably, the electrical conductivity of oxidized DWCNTs is better retained as compared to SWCNTs. The volume electrical conductivity of a ~1.5 μm thick film prepared from oxidized DWCNTs reaches  $2.75 \times 10^4$  S·m<sup>-1</sup>, i.e. 66% of electrical conductivity was retained after the outer-wall selective oxidation. This value is 65% higher than what is retained for similarly functionalized HiPco SWCNTs (Table 2-2). The electrical conductivity of the over-oxidized DWCNTs (5 mL 24 hrs samples) drops by 47±2% in comparison to the *oso*-DWCNTs (10 mL 2 hrs samples) for both the 1.53 μm and 0.15 μm films, manifesting the importance of outer-wall selectivity. In contrast to functionalized SWCNTs, the intact inner-tubes of *oso*-DWCNTs provide a continuous conductive pathway which is otherwise shortened due to sidewall functionalization (Figure 2-7A and B).

**Table 2-2.** Electrical conductivity of *oso*-DWCNTs thin films in comparison with pristine DWCNTs, SWCNTs, and functionalized SWCNTs

		Conductivity S·m <sup>-1</sup> (percentage retained)*	
		1.53 μm thick strip	0.15 μm thick strip
<b>Single-walled</b>	Pristine	6.70E+04	7.24E+04
	Functionalized	2.65E+04 (40%)	2.92E+04 (40%)
<b>Double-walled</b>	Pristine	4.16E+04	3.81E+04
	<i>oso</i> -DWCNTs	2.75E+04 (66%)	2.06E+04 (54%)

Note: \*Number in parentheses denotes the percentage of electrical conductivity retained after functionalization with respect to the respective pristine nanotubes of similar thickness. All errors are within ±5%.

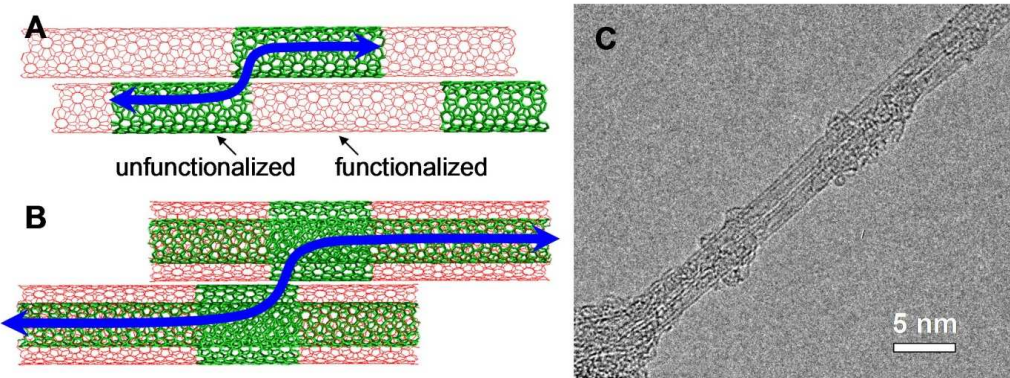


**Figure 2-7.** Electrical percolation of *oso*-DWCNTs via inner-tubes. (A) The broken conductive pathway due to sidewall functionalization of SWCNTs. (B) Intact inner-tubes extend the electrically conductive pathways. (C) High resolution TEM image showing two *oso*-DWCNTs in contact.

However, if the outer-wall is functionalized, how could the inner-tubes make electrical contact with the outer-wall and also interconnect with one another so effectively? This puzzle was resolved with high resolution TEM, which revealed a clustered distribution of functional groups on a carbon nanotube surface (Figure 2-7C). There are segments of intact outer-walls on the orders of 10s of nanometers that would allow two functionalized DWCNTs to contact electrically with the inner-tubes. The clustered distribution of functional groups also explains the surprisingly low Raman D/G ratio associated with these oxidized DWCNT samples. Typically, the D/G ratio indicates the degree of DWCNT functionalization. The D/G ratio increases with increasing amount of nitric acid in addition to increasing reaction time, however the increase is small. For the 2 hrs samples, the D/G ratio changes little with respect to that of as-received DWCNT material ( $\sim 0.07 \pm 0.01$ ) (Figure 2-1). Given the high water solubility, the D/G ratio of *oso*-DWCNTs is unexpectedly low compared with those of oxidized

graphenes<sup>110</sup> and SWCNTs functionalized using covalent organic chemistry (~1.0).<sup>111</sup> However, similarly low D/G ratios have been reported for short SWCNTs with non-functionalized sidewalls.<sup>112</sup> These observations can be explained by invoking a theoretical prediction by Morokuma et al. that the introduction of sp<sup>3</sup>-type defects to a nanotube sidewall causes a significant decrease of Raman intensity of the G-band due to the broken symmetry.<sup>113</sup> In contrast to conventional organic covalent chemistry, the preservation of the cylindrical symmetry, as indicated by the observed structural pattern of the oxidized DWCNTs, might have retained the Raman intensity of the G-band and hence, showing the relatively low D/G ratio.

These data strongly suggests that the intercalation oxidation occurs preferentially by reaction propagation from existing defects. Such a reaction mechanism and the resulting *oso*-DWCNT structures may provide opportunities to tune the interactions of “sticky” nanotubes over a wide range that was impossible before to realize extremely low percolation thresholds in nanocomposites.<sup>82</sup> It is also important to note that the starting DWCNT samples have a purity of only 60% as specified by the manufacturer. Of these 60%, the possibility of an inner-tube is metallic is approximately 1/3.<sup>3</sup> Significant improvements are anticipated with enriched DWCNTs<sup>104</sup> or if pure metallic types can be separated or synthesized. Ongoing experiments are addressing these questions. However, the reported *oso*-DWCNTs and the more efficient electrical percolation through inner-tubes suggest a powerful mechanism to simultaneously

improve dispersion of and percolation through carbon nanostructures in conductive composites.

Piao et al.<sup>114</sup> later applied this same covalent functionalization strategy with even greater success by using a diazonium reaction to attach benzene groups to the outer-walls of DWCNTs. While the oxidation chemistry<sup>80</sup> reported here has the advantage of improving water solubility of the carbon nanomaterials, the reaction is fairly aggressive and can oxidatively digest the nanotubes if conditions are not carefully monitored. This problem can make outer-wall selectivity difficult to achieve. The advantage of the diazonium based chemistry is its ability to selectively functionalize outer-walls of DWCNTs due to size exclusion; the diazonium molecule is too large to enter the interior of the nanotube and is limited to functionalizing the outerwalls. With this size exclusion mechanism, the reaction can be pushed much further, so covalently functionalized SWCNTs prepared using this chemistry can be completely insulating. The same degree of DWCNT functionalization results in a retention of approximately 50% of the original conductivity.<sup>114</sup>

This diazonium-based outer-wall-selective functionalization strategy was recently demonstrated to be particularly effective for electronic CNT devices such as thin-film transistor (TFT) based sensors for small-molecule detection. Benzoic acid groups attached to the outer-walls of DWCNTs by diazonium chemistry improve the sensitivity and selectivity of amine detection compared to similarly functionalized SWCNT devices, which were less conductive (due to covalent

addition) and thus yielded lower signals.<sup>115</sup> There are plans to use this functionalized DWCNT TFT device as a biological molecule sensor.

## Conclusions

Outer-wall-selective oxidization of DWCNTs was demonstrated by reacting DWCNTs with a combination of oleum and nitric acid. The intercalation of oleum between bundled DWCNTs presumably opens the diffusion pathways for nitric acid to access the outer-walls, resulting in a homogeneous reaction. The outer-wall selectivity was confirmed with Raman spectroscopy and high resolution TEM. The conductivity of an *oso*-DWCNTs thin film approached  $2.7 \times 10^4$  S·m<sup>-1</sup>, up to 65% better than similarly functionalized SWCNTs thin films. This improvement is due to the outer-wall selective reaction, which maintains a conductive inner-tube pathway. Improved electrical percolation could be attributed to the combination of the intact inner-tubes and regions of the outer-walls that remained non-oxidized.

These intact regions of the outer-walls are of interest to us mechanistically. Previous CNT functionalization studies displayed similar bands of covalent modification. For example, gas-phase fluorination reactions of CNTs were accessed using scanning tunneling microscopy and showed a tendency of the fluorine atoms to covalently attach in continuous and discrete regions of the nanotube.<sup>116</sup> As a result of this functionalization pattern, regions of the CNT remained intact. Maintaining continuous tracks of sp<sup>2</sup> hybridized carbon atoms is essential for retention of desirable graphitic properties as we have just

demonstrated with the outer-wall selective chemistry in the retention of the integrity of the inner-tube. We were motivated to continue to study how the location of CNT covalent functional groups can be exploited to maintain functionality, particularly in a possible banding morphology for SWCNTs that do not have the advantage of the inner-tube.

Beyond the fluorination reaction, SWCNT functionalization patterns have been fairly unexplored in the literature, although a few oxidation chemistries suggested a similar morphology.<sup>67,95,107</sup> The activation of  $sp^2$  carbon atoms at neighboring  $sp^3$  defect sites for covalent addition may be due to bond angle strain.  $Sp^2$  hybridized carbon prefers a flat,  $120^\circ$  bonding angle, while  $sp^3$  carbon bonding is tetrahedral ( $109.5^\circ$ ). Thus, the angle strain of neighboring  $sp^2$  and  $sp^3$  carbon atoms is even greater compared to ortho  $sp^2$  carbon sites. Functionalization and conversion to entirely  $sp^3$  relieves such strain as the nanotube angle of curvature more closely matches the pyramidalization angle.<sup>117,118</sup> For this reason, despite steric effects it may be more energetically favorable that covalent functionalization occur in clustered regions of the nanotube rather than via uniform nucleation of defects across the surface.

In the following chapter, we will demonstrate how highly reducing chemistry can also result in banding morphologies of functional groups on the nanotube. By functionalizing SWCNTs with alkyl halide based radicals using sodium in liquid ammonia, we have determined that this chemistry tends to propagate from pre-existing defects, resulting in a confined defect propagation mode. We believe this mechanism results from  $sp^3$  hybridized carbon localization

of electrons injected into the SWCNT electronic structure under highly reductive chemical conditions, activating electrophilic addition at these more highly reduced defect neighboring carbon atoms. Maintaining SWCNT functionalization in these bands helps retain optical properties including absorption and photoluminescence. This retention of optical properties may have importance for bio-imaging applications in the near-IR.

# Chapter 3: Confined Propagation of a Covalent Chemistry on Single-Walled Carbon Nanotubes

*Adapted from Deng, S.;\* Zhang, Y.;\* Brozena, A.H.\* et al. Nat. Commun. 2011, 2.*

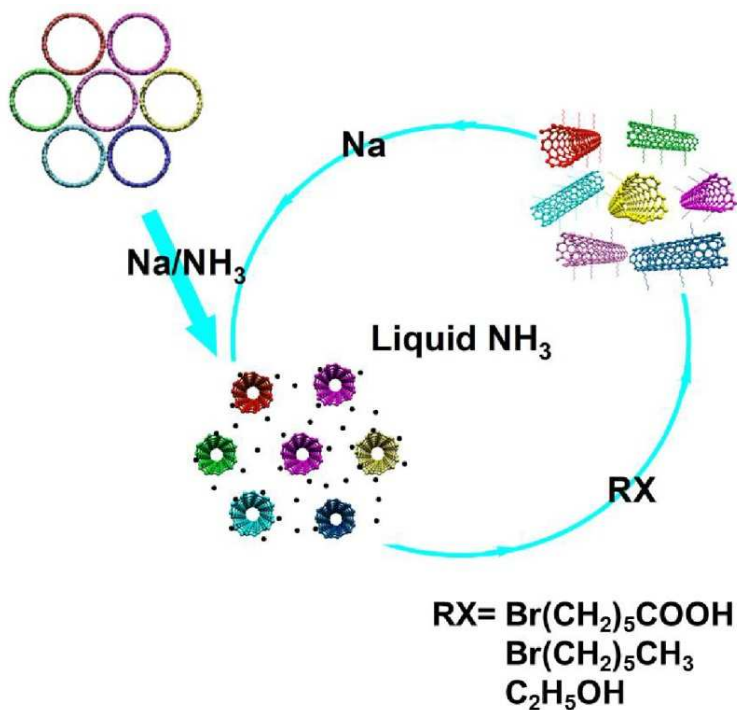
*\*Equal contribution*

*S. Deng synthesized the majority of the samples and took Raman, FT-IR, and absorption spectra. Y. Zhang took SEM images and measured the “functional band” lengths. A.H. Brozena took TEM images of the carbon nanotube samples before and after ALD deposition and developed carbon nanotube dispersion methods for this ALD experiment; she also synthesized many of the functionalized carbon nanotubes, particularly the non-hexanoic acid functionalized samples and took Raman spectra. M.L. Mayes did the DFT calculations and Mulliken Population Analysis. P. Banerjee performed all ALD on the carbon nanotubes.*

## Introduction

Where and how does a molecule covalently bond to a “ $\pi$ -electron sea?” This fundamental question is of central importance to the development of selective chemistries for extended carbon networks, such as SWCNTs<sup>63</sup> and graphene,<sup>119</sup> in which  $\pi$ -electrons are delocalized over thousands of carbon atoms. Theoretical studies predict that the pattern of functional groups, or defects, will substantially affect the electrical and optical properties of these types of low-dimensional systems.<sup>120,121</sup> Spatially controlled chemistry may find uses in graphene edge engineering,<sup>122</sup> molecular lithography,<sup>123</sup> and nanotube electrode networks.<sup>80</sup> Experimentally, it is challenging to control functionalization patterns in carbon nanostructures. For example, recent experiments have demonstrated that diazonium chemistry occurs at completely random atomic sites on a SWCNT

sidewall.<sup>69</sup> The covalent modification of even a single site results in a substantial drop of electrical conductivity<sup>70</sup> and stepwise quenching of exciton fluorescence in semiconducting nanotubes.<sup>69</sup>

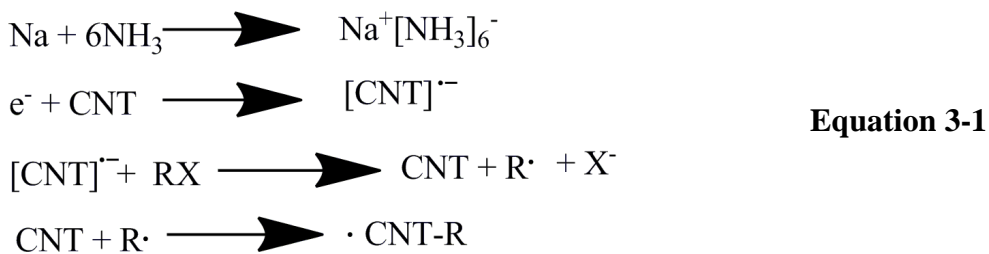


**Scheme 3-1.** Schematic illustration of the recycling, reductive alkylation of SWCNTs.

Here, we show that the Billups-Birch reductive alkylcarboxylation,<sup>124</sup> a variant of the nearly century-old Birch reduction chemistry,<sup>125,126</sup> occurs on SWCNTs exclusively, to the extent observable in our experiments, by reaction propagation from existing defects—the edge of the  $\pi$ -electron sea. Carbon nanotubes were homogenously dispersed in an ammonia solution of solvated electrons and covalently functionalized by alternating the addition of sodium and various alkyl halide reagents in a recycling procedure (Scheme 3-1).

Mechanistically, it is believed the reduced CNTs engage in single-electron

transfer to the alkyl halide reagent, homolytically cleaving the halide and generating a highly reactive alkyl radical that attaches to the nanotube surface (Equation 3-1).<sup>125</sup> The propagation mechanism of this chemistry makes it possible to progressively add new functional groups to the graphitic lattice without nucleating unintended new defects. This defect-activated chemistry bears a remarkable similarity to the high reactivity of nanotube ends<sup>112,127</sup> and step edges in surface science.<sup>128,129</sup> Confinement of the reaction to carbon nanotube “sp<sup>3</sup> step edges” leads to reaction fronts initiated at defect sites that ultimately propagate along the tube at a constant rate.



## Materials and Methods

Two SWCNT materials, HiPco (Rice University) and (6,5)-enriched CoMoCat (Southwest Nanotechnologies, Inc.), were used in this study. HiPco SWCNTs were purified using a one-pot purification method<sup>130</sup> and CoMoCat SWCNTs were used as received. All other reagents were purchased from Sigma-Aldrich and used without further purification.

### *Synthesis of HiPco-[ $(\text{CH}_2)_5\text{COONa}$ ]<sub>n</sub>*

In a typical experiment, purified HiPco SWCNTs (10 mg, 0.83 mmol of carbon) were added to a flame-dried, argon-purged, 250-mL, four-neck round-

bottom flask fitted with a dry-ice/acetone condenser. 75 mL liquid ammonia was condensed into the flask followed by addition of sodium (0.029g, 1.25 mmol), which spontaneously produced a blue color owing to solvated electrons. After stirring for 10 minutes, 6-bromohexanoic acid (0.975 g, 5.00 mmol) was added and the mixture was stirred overnight while the liquid ammonia evaporated. Subsequently, 100 mL nanopure water was added to the flask and briefly sonicated. The functionalized SWCNTs were collected over a 0.8  $\mu$ m ATTP membrane (Millipore), re-dispersed in water and repeatedly extracted with hexane (20 mL) in a separatory funnel to remove salts. The hexane layer was filtered through a 0.8  $\mu$ m ATTP membrane forming a buckypaper of functionalized SWCNTs, which was washed with ethanol and water and dried overnight in a vacuum oven at approximately 80°C.

For multiple reaction cycles, the previously functionalized SWCNTs were used as starting materials. Sodium and 6-bromohexanoic acid were alternately added into the flask at each reaction cycle (Scheme 3-1). After the first cycle, extra sodium was added to balance the loss due to the reactive –COOH groups. For each cycle, the solution was allowed to react for 1 hr.

*Synthesis of CoMoCat-[ $(CH_2)_5COONa$ ]<sub>n</sub>, CoMoCat-[ $(CH_2)_5CH_3$ ]<sub>n</sub> and CoMoCat-[H]<sub>n</sub>*

CoMoCat SWCNTs (20 mg, 1.67 mmol) were exfoliated in 75 mL liquid NH<sub>3</sub> by sodium (0.058g, 2.5 mmol), and subsequently reacted with 6-bromohexanoic acid (0.650 g, 3.33 mmol), 1-iodohexane (0.706 g, 3.33 mmol), or

methanol (0.533 g, 16.67 mmol). Up to 40 reaction cycles were carried out using the same procedures as described above.

### *3-Cycle reaction and water extraction*

Water extraction experiments were carried out on a 3-cycle functionalized HiPco-[ $(CH_2)_5COONa$ ]<sub>n</sub> sample, beginning with 52 mg of purified HiPco-SWCNTs. After functionalization, the black solid was dispersed in 80 mL basic water (pH=10.5). 10 mL hexane was then added to the dispersion and the mixture was shaken vigorously. After phase separation, the aqueous phase was collected. The hexane layer of SWCNTs was filtered over 0.2  $\mu$ m GTTP Isopore membrane (Millipore). This extraction process was repeated to produce 13 bottles of water soluble SWCNT solutions, the last third of which exhibited the optical properties as shown in Figure 3-4.

### *Solubility measurement*

The water solubility was measured by centrifugation in conjunction with UV-Vis-NIR spectroscopy. The solid samples were dispersed in basic water (pH = 10) by bath sonication for 1 hr. Then the aqueous solutions were centrifuged on a Beckman Coulter Microfuge 16 centrifuge at 1919g until the supernatant reached a stable, isotropic phase showing no further decrease in absorbance.

### *Spectroscopy characterization*

Raman scattering spectra were collected on a Horiba Jobin-Yvon LabRAM HR-VIS microRaman system with a helium neon laser excitation source. Lower power density (~0.1 mW/ $\mu$ m<sup>2</sup>) was used to exclude laser induced

thermal effects.<sup>131</sup> UV-Vis-NIR spectra were measured using a Perkin Elmer Lambda 1050 spectrophotometer. Excitation-emission maps were measured with a Horiba Jobin Yvon NanoLog spectrofluorometer using a liquid nitrogen-cooled InGaAs detector array. For Fourier transform-Infrared (FT-IR) analysis, the functionalized SWCNTs was acidified with 0.5 M HCl to ensure termination with -COOH rather than -COONa. A Jascob FT/IR-4100 Spectrometer with an ATR accessory was employed to record the FT-IR spectra.

#### *Au-Substrated Enhanced Scanning Electron Microscopy*

The water soluble SWCNTs were drop-cast on a gold-on-silicon substrate, air dried, and then rinsed with water to remove salts. SEM was performed on a Hitachi SU-70 Schottky field emission gun SEM operating at an accelerating voltage of 1 kV with an emission current of 34-35  $\mu$ A.

#### *Atomic Layer Deposition*

$\text{Al}_2\text{O}_3$  was grown on SWCNT-[ $(\text{CH}_2)_5\text{COOH}$ ]<sub>n</sub> drop-cast on an SPI lacey carbon copper grid using a BENEQ TFS 500 ALD reactor. Trimethyl aluminum (TMA) and de-ionized water were supplied as alternate 250 ms pulses from room temperature ampoules, separated by 500 ms  $\text{N}_2$  system purges with the reactor temperature at 150°C. These conditions yielded a growth rate of ~1.0 Å/cycle which was consistent with literature values.<sup>132</sup> TEM was performed on a JEOL JEM 2100 LaB6 transmission electron microscope at an accelerating voltage of 200 kV.

### *Thermogravimetric analysis*

TGA experiments were performed on a TA Instruments Q500. In TGA analysis, the sample was held at 100 °C for 30 min, ramped 10 °C min<sup>-1</sup> to 800 °C, and then held at 800 °C for 30 min. The carbon/functional group ratio or functional density was calculated according to the weight loss, which can be attributed to the thermally cleaved organic functional groups. For example, for HiPco-[ $(\text{CH}_2)_5\text{COOH}$ ]<sub>n</sub> after 1 cycle of functionalization, the weight loss was 25.07%, corresponding to a functional density of 3.45% or one carboxyl group in every 29 nanotube carbons. This result is consistent with the previous findings.<sup>122</sup> After 20 cycles of functionalization, the weight loss was increased to 43.08%, corresponding to a functional density of 7.69 %.

## **Results and Discussion**

### *“Banded” SWCNTs*

The sp<sup>3</sup> defect propagation mechanism is most directly illustrated by the creation of “banded” SWCNTs. These SWCNTs feature with alternating segments of functionalized (sp<sup>3</sup> hybridized) and intact regions (which remain sp<sup>2</sup> hybridized) created through reaction propagation that starts at defects initially present in the nanotubes or introduced during the H<sub>2</sub>O<sub>2</sub>/HCl purification process (Figure 3-1A).<sup>130</sup> We were able to simultaneously resolve the functionalized and intact regions along the same nanotube by substrate-enhanced scanning electron microscopy.<sup>133</sup> When such functionalized nanotubes were deposited on a gold substrate and imaged with an SEM electron beam at 1 kV, we observed regular alternation of bright and dark contrast along the nanotube length (Figure 3-1B).

The sharp image contrast arises from a substantial increase in the yield of secondary electrons at 1 kV due to covalent modification of the nanotube in greater contrast with the surrounding pristine SWCNT and gold substrate materials. After annealing the samples at 750 °C under flowing Ar/H<sub>2</sub> for 1 hr, which fully recovered the pristine structure of the nanotubes, the banding structures were lost and the images showed the same contrast as those of raw nanotubes (Figure 3-1C). The brighter regions exhibit a contrast comparable to those of microcontact-printed 16-mercaptophexadecanonic acid on a gold substrate (Figure 3-1D). Based on these observations we can unambiguously attribute the bright regions to alkylcarboxylic acid groups and the darker regions to intact nanotubes. Notably, this propagation mechanism persists even after extensive reaction.

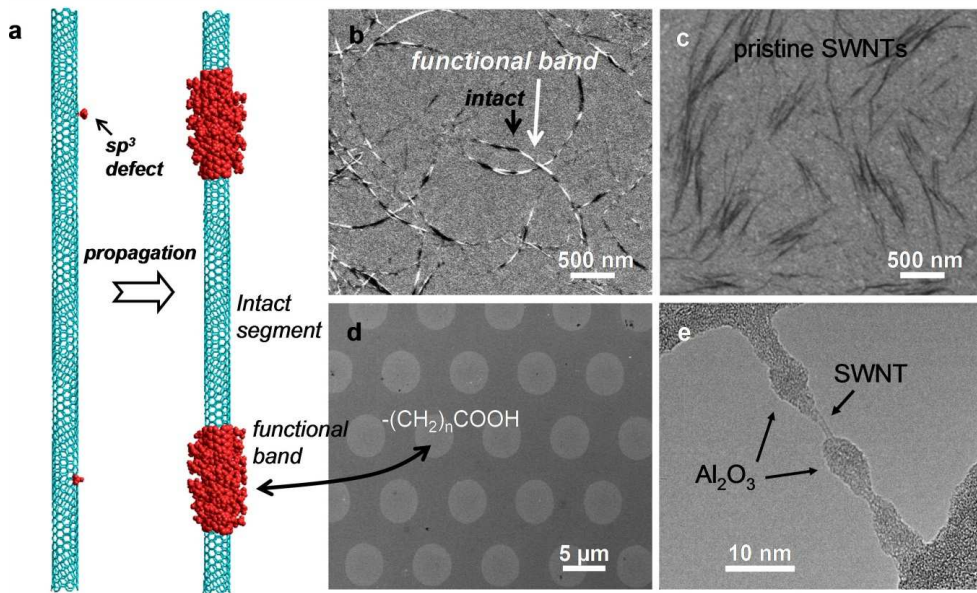
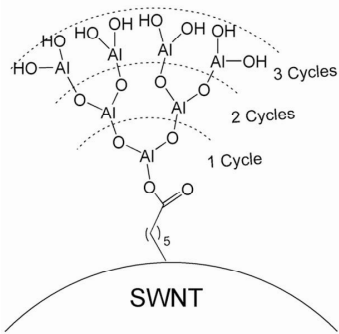


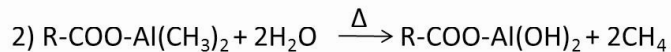
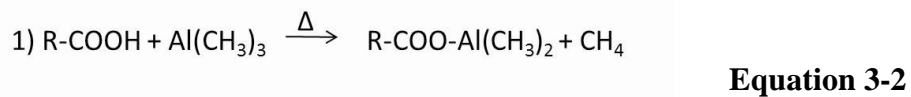
**Figure 3-1.** Functional bands on SWCNTs. (A) Schematic illustration of reaction propagation initiated at  $sp^3$  defect centers that ultimately propagate along the tubular direction, creating  $sp^3$  bands of functional groups. (B) Alkylcarboxylated nanotubes on a gold substrate imaged using an SEM operated at 1 kV. The dark and bright regions closely resemble (C) pristine nanotubes and (D) patterned carboxylic acids, respectively. (E) High resolution TEM image of an individual SWCNT- $[(CH_2)_5COOH]_n$  coated with  $Al_2O_3$  by  $-COOH$  selective atomic layer deposition using TMA and  $H_2O$  precursors.



**Scheme 3-2.** An illustration of the growth of  $Al_2O_3$  from a carboxylic acid functional group on the CNT surface with self-limiting, cycled ALD chemistry (Equation 3-1).

With the aid of atomic layer deposition (ALD), the position of alkylcarboxylic functional groups can also be observed by TEM. ALD is a self-

limiting chemical vapor deposition process that is used to grow metal oxides in discrete, atomic thick layers (Equation 3-1). Normally, the functional groups alone are too small to observe with electron microscopy, however by using ALD to nucleate  $\text{Al}_2\text{O}_3$  from these acid moieties we are able to amplify the visual impact of functional groups through the defect-tagging oxide layer. Using this method, we observed that the  $\text{Al}_2\text{O}_3$  coated extensive regions of the 40 cycle functionalized nanotubse in discrete bands, though small segments of intact nanotubes (5 – 10 nm) were still frequently observed without an oxide layer (Figure 3-1E).



=1 cycle  $\text{Al}_2\text{O}_3$  nucleation

Because this ALD chemistry is self-limiting and chemically selective to reactive functional groups (here carboxylic acids),<sup>134–136</sup> the discrete  $\text{Al}_2\text{O}_3$  coating (Scheme 3-2) reflects the clustered distribution of the functional groups,  $-(\text{CH}_2)_5\text{COOH}$ , along the nanotube. Figure 3-2 provides the complete spread of the ALD/functional group tagging experiment, in which different numbers of ALD cycles were used to grow increasing thickness of  $\text{Al}_2\text{O}_3$  from the carboxylic acid functional groups.

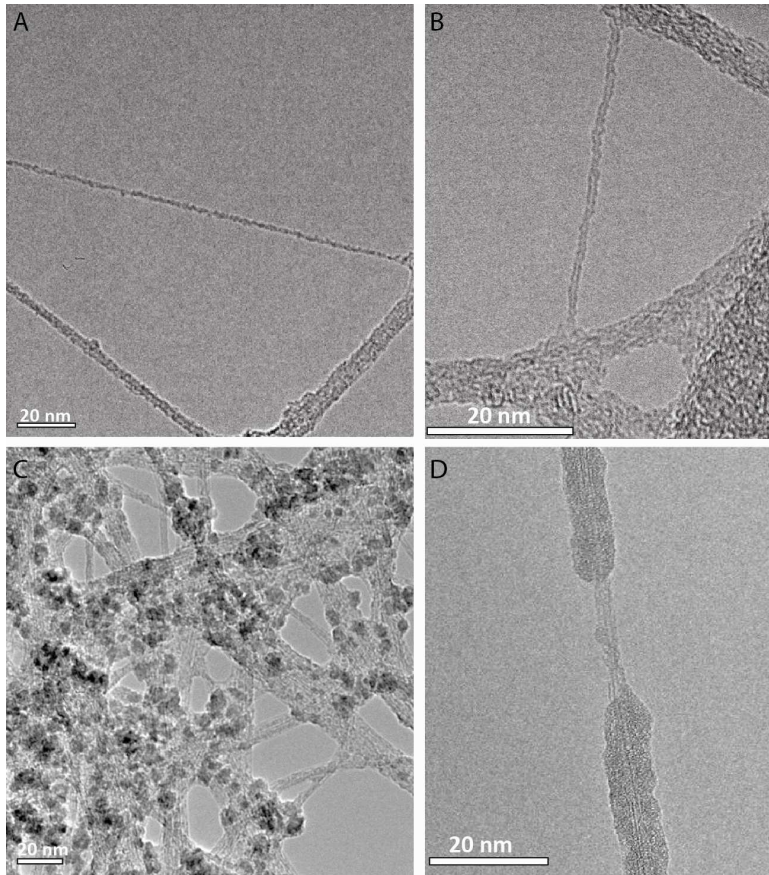


**Figure 3-2.** TEM images of (A) Non-functionalized, (B) 40 cycles Billups-Birch hexanoic acid functionalized SWCNTs before and after (C) 10 and (D) 50 cycles of  $\text{Al}_2\text{O}_3$  deposition at  $-\text{COOH}$  groups.

#### *Propagation modes*

Two distinct modes of defect propagation were revealed in the length distribution of the SEM-resolved intact segments and functional bands (Figure 3-3). The intact segments ( $124 \pm 27$  nm in length) follow a broad, Gaussian length distribution, suggesting a random spatial distribution of initial defects on the pristine nanotubes, as expected. The average pitch is found to be  $212 \pm 48$  nm (this is a lower bound limit, since two or more defects in proximity can develop a merged functional band). This low defect density is corroborated with negligible weight loss at elevated temperatures due to decomposition of the functional

groups, low disorder peak in Raman spectra, and bright fluorescence from individually dispersed pristine nanotubes. In contrast to the intact segments, the functional bands have much narrower distributions. We found that more than 80% of the 81 nanotube ends identified by SEM imaging had a functional band. These end functional bands extend  $53\pm19$  nm on average after three reaction cycles, which is approximately half the length of bands located along the nanotube sidewall ( $88\pm21$  nm). This strong length correlation arises because a defect on the nanotube sidewall will allow the propagation to occur in both directions equally, while there is only one possible direction to propagate from a SWCNT end, the natural defect in the  $\pi$ -electron sea. Note that a reaction cycle in the reductive alkylcarboxylation is limited by the reductant (solvated electrons) which can be stored in the nanotube before reaction.

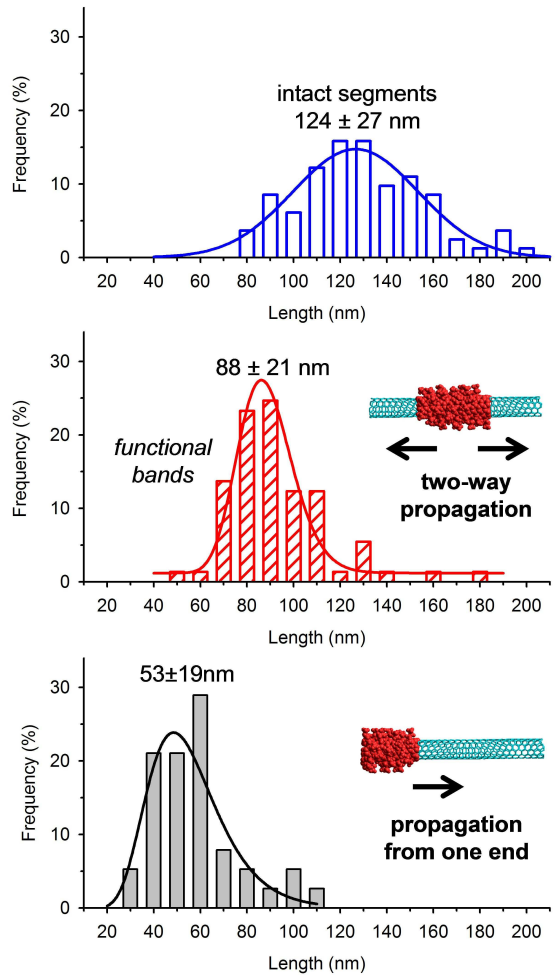


**Figure 3-3.** Two modes of propagation revealed in the length distributions of intact segments and functional bands. The lengths were extracted from SEM images of the same alkylcarboxylated nanotube sample. The sample sizes are 82, 73, and 38, respectively. The curves were fitted with Gaussian, log-normal, and log-normal functions with peaks at  $124 \pm 27$ ,  $88 \pm 21$ , and  $53 \pm 19$  nm, respectively. The errors represent one standard deviation.

### Optical properties

The covalently functionalized SWCNTs retained some of the optical properties of SWCNTs (Figure 3-4). Optical properties of nanotubes are often completely lost due to covalent modification of the electronic band structures by even a small number of defects.<sup>60,69</sup> A defect density of  $\sim 1/10,000$  ( $\sim 0.001\%$ ) is

typically sufficient to completely quench nanotube fluorescence.<sup>69</sup> Partial retention of the van Hove optical absorption<sup>60</sup> and exciton fluorescence<sup>69</sup> properties was made possible here even at a high degree of functionalization (~45 functional groups per 1000 carbons) because of clustered distribution of the –(CH<sub>2</sub>)<sub>5</sub>COOH functional groups along the nanotube length, leaving intact regions of sp<sup>2</sup>-hybridized carbons with sustained band structures (Figure 3-1A and B).

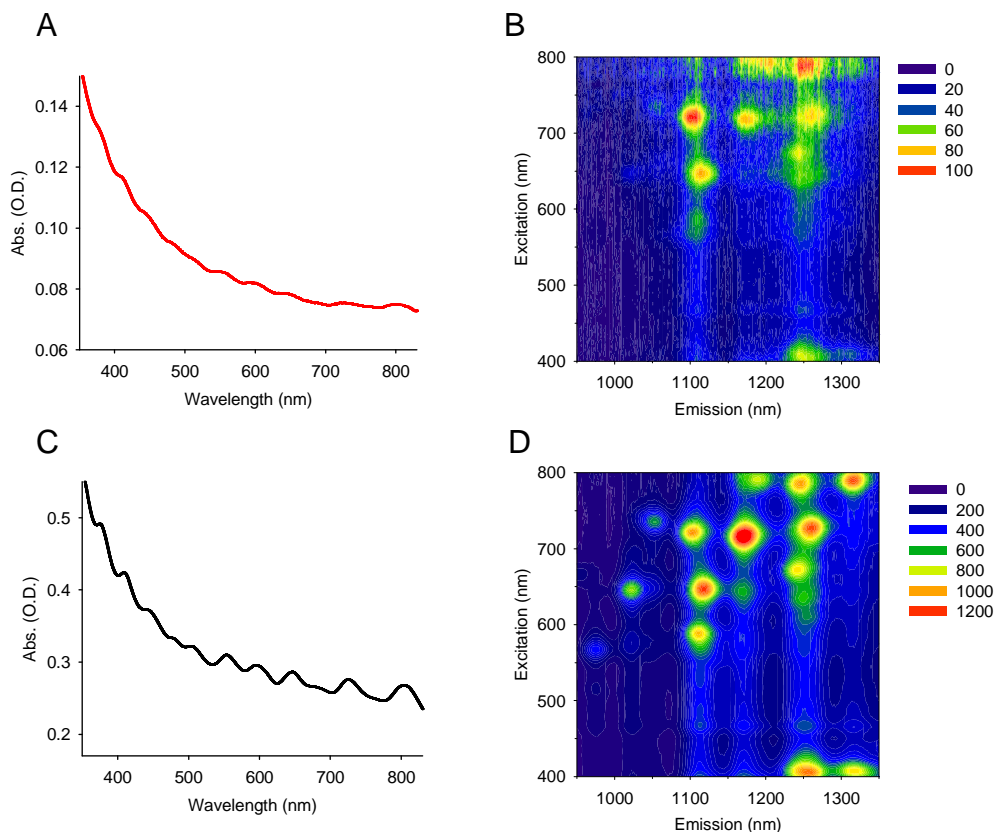


**Figure 3-4.** (A) Visible-NIR absorption spectrum and (B) excitation-emission map of 3-cycle HiPco-SWCNT-[C<sub>2</sub>H<sub>5</sub>)<sub>5</sub>COOH]<sub>n</sub> in comparison with (C,D) the starting, non-functionalized nanotubes, which were individually dispersed in D<sub>2</sub>O solutions of 1wt% SDBS. The van Hove singularity transitions apparent in the absorption spectra from different nanotube chiralities are retained even after covalent functionalization. The photoluminescence properties are retained as well.

This propagation chemistry has allowed us to produce water soluble nanotubes (up to 3,380 mg/L) after 40 cycles of reaction (Figure 3-5), approaching the solubility achieved only in chlorosulfonic superacid.<sup>137</sup> This high water solubility was previously unexpected.<sup>111,138</sup>

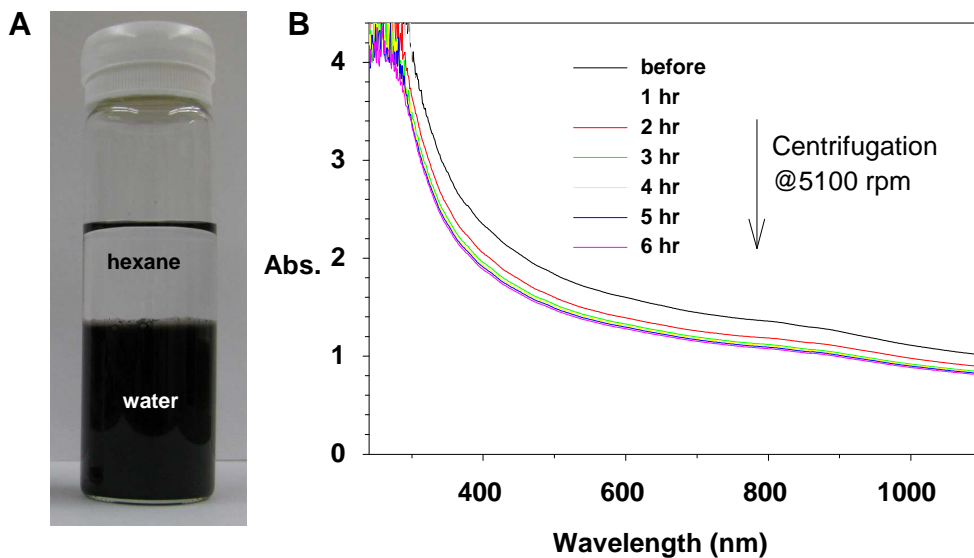


**Figure 3-5.** (A) Water soluble SWNT-[ $(CH_2)_5COONa$ ]<sub>n</sub>. Under solvation competition between water and hexane. (B) Determination of water solubility of nanotubes by optical-centrifugation. UV-Vis-NIR spectra of 20-cycle-functionalized SWNTs-[ $(CH_2)_5COONa$ ]<sub>n</sub> before and after centrifugation at 5100 rpm (1919 g). The saturated nanotube solution was diluted 10 times before the centrifugation.

We propose a simple kinetic model to account for the observed propagation of functional bands (Figure 3-6). For free propagation from a point defect without any constraint, the number of reaction sites at the reaction front will continuously accelerate as the “sp<sup>3</sup> step edge” expands. A transition occurs at a propagation length equal to the circumference of the nanotube, and then at which point propagation becomes confined in a banded morphology down the

length of the tube. The reaction rate becomes constant after the propagation reaches a critical length,  $l_c \sim 1.5\pi d$ , where  $d$  is the nanotube diameter – the ultimate limit of the  $sp^3$  step edge. For a 1 nm diameter SWCNT, this simple model shows that the propagation becomes confined as the reaction expands beyond approximately 5 nm from a defect center. From the nanotube end functional bands, we estimate that the propagation rate is  $18 \pm 6$  nm per reaction cycle under the experimental conditions investigated.

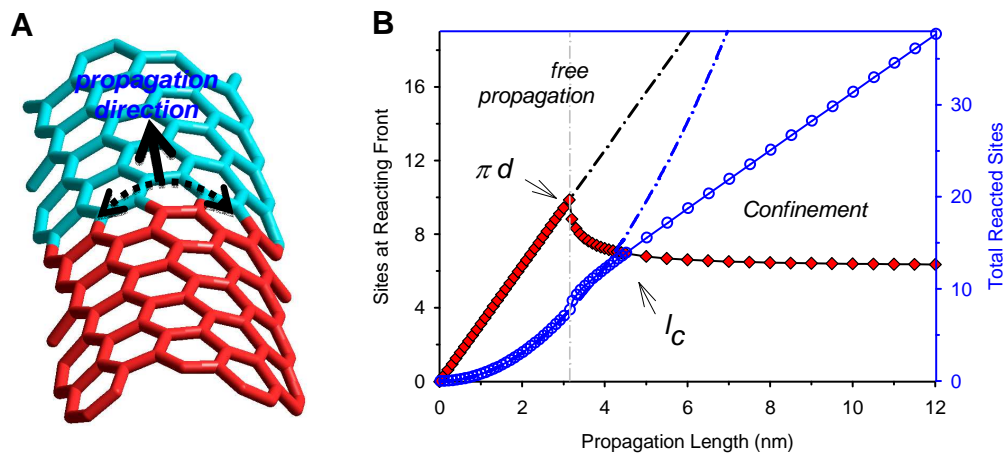


**Figure 3-6.** A kinetic model of reaction propagation from a point defect on a  $sp^2$  bonded carbon lattice. (A) Schematic illustration of the propagation front. For clarity the functional groups are omitted. Note that for most chemistry only a small fraction of carbon sites within the functional band are functionalized. (B) Propagation with confinement to the nanotube cylinder (solid lines) vs. free propagation on an infinite sheet (dotted lines). The sites at the reaction front (red diamond) and total reacted sites (blue open circles) are computed based on geometric considerations for a 1 nm diameter nanotube. For the defect-activated reaction, the reaction rate is proportional to the number of  $sp^3$  defect centers available at the reaction front, which initially increases linearly with propagation length. At a higher degree of functionalization, specifically when the propagation length reaches the circumference of the nanotube  $\pi d$ , the reaction propagation becomes confined to the direction along the nanotube. The degrees of freedom for propagation along the nanotube circumference are completely lost at a critical propagation length  $l_c \sim 1.5\pi d$ , after which the reaction rate becomes a constant.

To more quantitatively describe this picture of reaction propagation, we calculate the relative probability of propagation with respect to the spatially random addition of new functional groups (nucleation). This relative probability defines the “purity” of reaction propagation. We can experimentally determine this parameter by estimating the lower limit number of functional groups within a functional band compared to random nucleation, if any, in the intact segments as reflected by fluorescence. For the SEM-resolved bands of a 3-cycle carboxylic acid functionalized sample (Figure 3-1B), the corresponding average functional density, or the percentage of nanotube carbon atoms that are covalently functionalized, was ~4.5% based on the weight loss of functional groups at elevated temperatures under argon by TGA (Figure 3-7). Given average lengths of 88 and 124 nm functionalized and intact regions respectively, the functional density within the band can be calculated as at least 12%, suggesting only a fraction of the carbons within the band were functionalized. As such, an 88 nm band contains more than 1300 functional groups on average for a 1 nm diameter SWCNT. At this degree of functionalization, the nanotubes fluoresced with a relative quantum yield that is 25% that of the initial starting nanotubes (Figure 3-4). Since a single defect can quench the exciton fluorescence as the exciton diffuses over 90 nm during its lifetime,<sup>69</sup> no more than 1 random nucleation on average should have occurred within the intact segments ( $124 \pm 27$  nm). Taken together, the relative probability of propagative functionalization is at least 1300 times higher than random nucleation. This spatial selectivity is more than 600 times higher than for diazonium chemistry, the only other covalent addition

chemistry whose spatial selectivity on carbon has been quantified.<sup>122</sup> It is important to note that banding has been observed previously with scanning tunneling microscopy on fluorinated nanotubes,<sup>139</sup> but the fluorination bands are densely spaced (pitch < 10 nm vs. the observed ~ 210 nm in this study), suggesting substantial contamination by random nucleation even if fluorination chemistry partially follows the propagation mechanism proposed here.

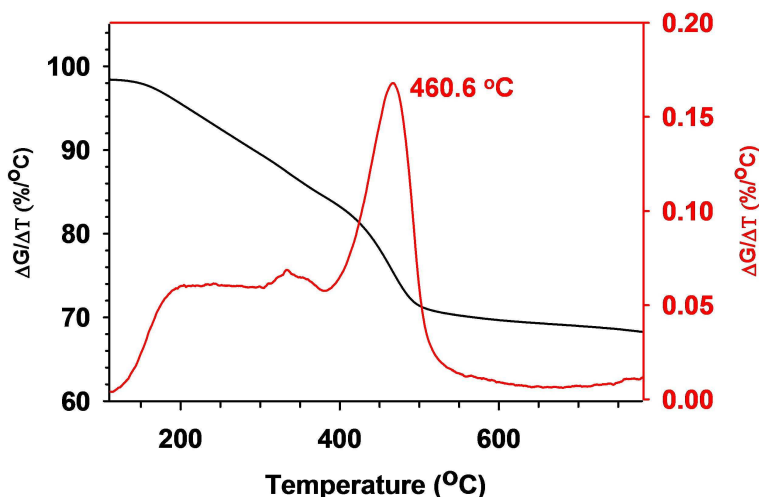


**Figure 3-7.** TGA of 15 cycle functionalized HiPco-[ $(\text{CH}_2)_5\text{COOH}$ ]<sub>n</sub>.

We repeated the reaction up to 40 cycles on CoMoCat (6,5) SWCNTs and characterized the functionalized nanotubes with correlated TGA, Raman spectroscopy, FT-IR, and water solubility measurements. The FT-IR spectra unambiguously confirmed the rise of various IR peaks after functionalization that are characteristic of C-H (2800-3000 cm<sup>-1</sup>, C-H stretch; 1415 cm<sup>-1</sup>, C-H bending) and -COOH moieties (1709 cm<sup>-1</sup>, C=O stretch; 1260 cm<sup>-1</sup>, C-O stretch). The C=O stretching mode grew consistently with increasing degrees of functionalization, in stark contrast with the featureless IR spectrum of the pristine SWCNT control (Figure 3-8).

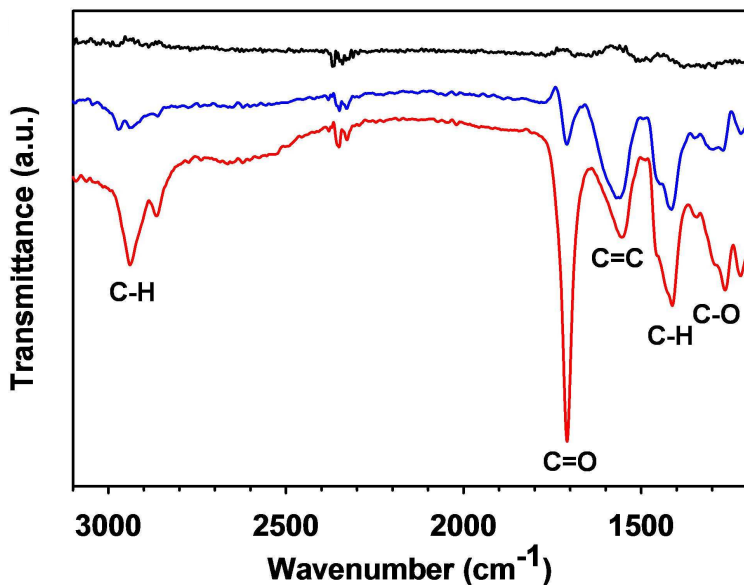


**Figure 3-8.** FT-IR of SWNT-[ $(CH_2)_5COOH$ ]<sub>n</sub> showing increased IR absorbance for –COOH and C–H from starting material (black curve), after 1 cycle of functionalization (blue curve) and 33 cycles of functionalization (red curve).

Consistently, the functional density grew linearly with increasing reaction cycles, as predicted by our confined propagation model. We found this reaction propagation mechanism to hold for other functional groups as well. For all three groups investigated, including  $-(CH_2)_5CH_3$ ,  $-(CH_2)_5COOH$ , and –H, Raman spectroscopy revealed similar trends of reaction propagation (Figure 3-9) and similar banding structures were found by SEM (except –H).<sup>133</sup> Covalent sidewall chemistry introduces  $sp^3$  defect centers, which decrease the Raman oscillator strength of the tangential modes around 1500–1600  $cm^{-1}$  (G bands) and give rise to the so-called D band (around 1350  $cm^{-1}$ ).<sup>99</sup> This effect allowed us to use the D/G ratio (peak area ratio between the D-band and the G-bands) to follow the reaction progress (Figure 3-9C). For the first 3–5 cycles of reaction, the D/G ratio rose exponentially, corresponding to the initial propagation from the  $sp^3$  defect,

sites which quickly convert a long nanotube into shorter segments from the Raman perspective. This result is consistent with previous observations from length sorted SWCNTs that the D/G ratio rises inversely as a function of nanotube length.<sup>140,141</sup> However, as the reaction continues, the trend follows a simple form,

$$\frac{D}{G} = \frac{D_0 + ax}{G_0 - bx}.$$
 This trend reflects a constant growth of the number of defects (x),

which contributes to the increase of the D-band (D) and simultaneous decrease of the G-band (G) intensity at relatively constant weights (a/b), a feature made uniquely possible by the confined propagation.

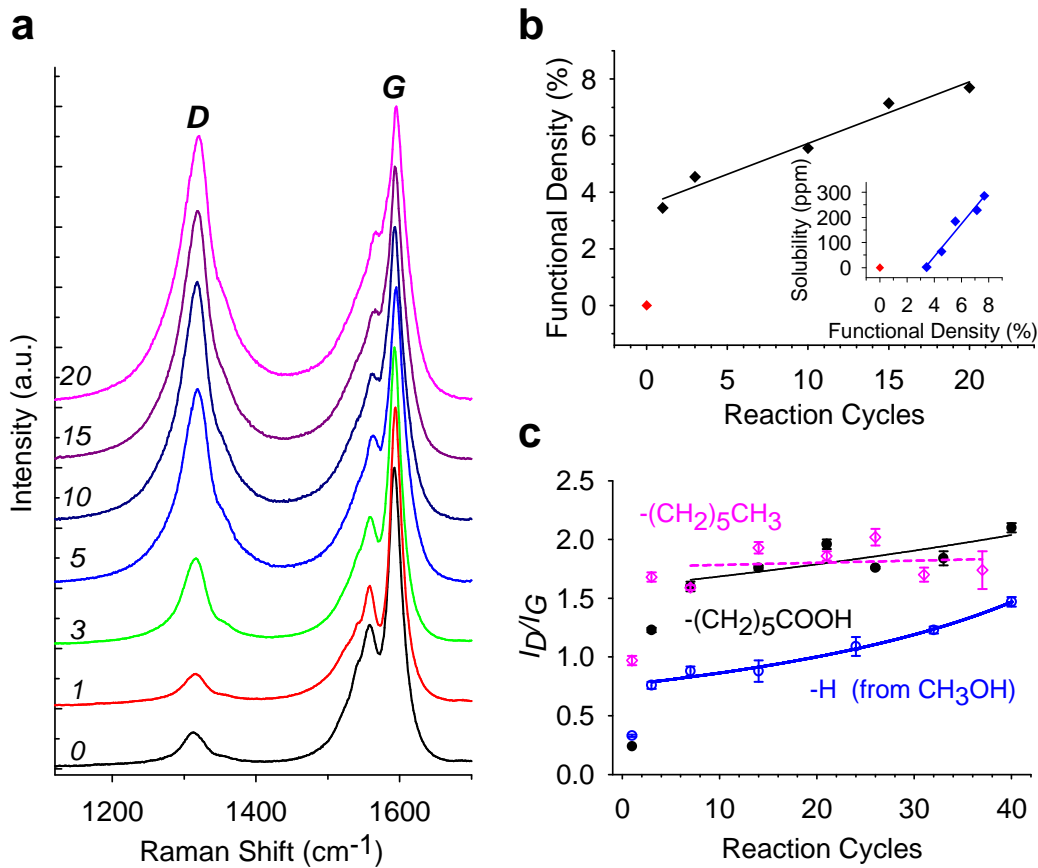


**Figure 3-9.** Evolution of Billups-Birch reductive addition. Correlated (A) Raman spectra, (B) degree of functionalization as determined from weight loss in TGA, and water solubility (B, inset) as a function of reaction cycles for a HiPco SWCNT sample after 0 to 20 cycles of functionalization with  $\text{Br}(\text{CH}_2)_5\text{COOH}$ . The excitation line was 632.8 nm. The degree of functionalization increased linearly with reaction cycles. The functionalized nanotubes became water soluble at a threshold functional density of approximately 3.5% and thereafter increased linearly as a function of reaction cycle. (C) Effect of terminating groups on the reaction propagation probed with Raman spectroscopy. (6,5) enriched CoMoCat SWCNTs were used for this study. The data were fit to  $y = \frac{D + ax}{G - bx}$ .

What is the chemical nature of the initial defects? We do not yet have the experimental means to answer this important question, partly because the initial defect density, approximately 1/10,000 (the fluorescence limit)<sup>69</sup> to 1/30,000 (average pitch of functional bands). However, the observed progressive alkylcarboxylation of nanotubes over at least tens of nanometers suggests that

these functional groups can act as new defect centers for continued propagation of the reaction fronts.

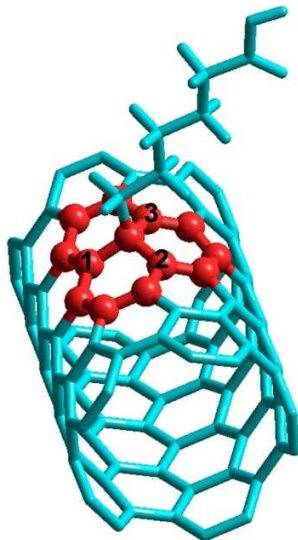


**Figure 3-10.** Optimized structure of a (5,5)-SWCNT with a covalently bonded  $-(\text{C}_2\text{H}_5)_5\text{COOH}$  group. The added electrons are largely localized on the highlighted carbon atoms.

To simulate the electronic effects of a single  $\text{sp}^3$  defect, we performed density functional theory (DFT) calculations on  $-(\text{CH}_2)_5\text{COOH}$  group functionalized (5,5)-SWCNT (Figure 3-10) and (10,0)-SWCNT using periodic boundary conditions. We have used the generalized gradient approximation of the Perdew-Burke-Ernzerhof<sup>142</sup> functional, a double- $\zeta$  basis set, and the standard norm-conserving Troullier–Martins pseudopotentials.<sup>143</sup> A Mulliken population analysis shows that the charges are localized in the carbons around the  $\text{sp}^3$  defect and the remaining atoms have almost negligible, charges (Table 3-1, Tables 3-2 and 3-3 in Appendix 1). When more electrons are added to the nanotube, as in the Birch reduction, the most significant charges are trapped around the defect site. This electronic effect extends as far as another carbon bond beyond the rings to

which the functional group is attached. These results suggest that the observed propagation phenomenon originates from two effects: (1) electrons are trapped around the defects; (2) the trapped electrons promote localized Birch reductive addition. These are essentially the same rules that govern the regioselectivity of the Birch reduction in small aromatic compounds such as anisole.<sup>144</sup> In an electron-delocalized system as large as a carbon nanotube, the Birch reduction occurs by propagating the reaction fronts at the edge of the electron sea.

<b>(5,5)-(CH<sub>2</sub>)<sub>5</sub>COOH</b>	<b>neutral</b>	<b>-1 charge</b>	<b>-2 charge</b>
defect site	0.12	0.13	0.13
C1	-0.04	-0.07	-0.08
C2	-0.02	-0.05	-0.06
C3	-0.02	-0.05	-0.06

<b>(10,0)-(CH<sub>2</sub>)<sub>5</sub>COOH</b>			
defect site	0.12	0.13	0.13
C1	-0.04	-0.06	-0.07
C2	-0.01	-0.02	-0.02
C3	-0.04	-0.06	-0.07

**Table 3-1.** Net atomic charges around a sp<sup>3</sup> defect site from Mulliken population analysis of a SWCNT with a covalently bonded -(CH<sub>2</sub>)<sub>5</sub>COOH group. Carbon atoms not listed have a charge close to zero, being as high as -0.01 e, and -0.02 e charges for neutral, -1, and -2 carbon nanotubes. For the complete set of atomic charges, see Tables 3-2 and 3-3 in Appendix 1.

## Conclusions

SWCNTs were covalently functionalized with a variety of organic groups using the Billups-Birch reductive alkylation chemistry. This chemistry is capable of significantly increasing the functional degree and disrupting attractive inter-tube van der Waals forces which enables the modified SWCNTs to attain high

water solubility after sufficient reaction cycles. Functional groups were attached to the nanotube sidewalls in a banding pattern, as observed via a combination of SEM and Al<sub>2</sub>O<sub>3</sub> tagged functional groups in conjunction with TEM. This observation suggests that this chemistry propagates along the nanotube from pre-existing defects. We note that this propagation chemistry is ideal for retaining the optical properties that are associated with intact sp<sup>2</sup> hybridized carbon atoms. Limiting functionalization to discrete zones thus retains tracts of graphitic carbon that exceed the exciton diffusion distance (~90 nm),<sup>69</sup> and enable photon absorption and subsequent radiative recombination for important near-IR photoluminescence properties.

Interestingly, our laboratory has also found alternative uses for this type of functional morphology, including the development of heterogeneous electrodes for lithium ion batteries in which silicon is deposited by low-pressure CVD onto the banded, functionalized CNTs. The functionalized surfaces provide superior adhesion of silicon due to enhanced surface energy interactions of the amorphous silicon to the sp<sup>3</sup> carbon functional groups. Ideally, this silicon-CNT morphology should help prevent lithium ion battery failure associated with silicon volume changes and delamination from the current collector (the CNT in this case).<sup>145</sup>

DFT modeling suggests this propagation mode of functionalization is a result of the localization of electrons surrounding sp<sup>3</sup> defects after chemical reduction of the SWCNT using solvated sodium in liquid ammonia. The trapping of electrons at these defect sites serves to promote the single electron transfer reaction that generates the reactive radicals from added alkyl halide reagents and

thus increasing the likelihood of covalent addition within the vicinity of the  $sp^3$  defect site.

This electron localization is related to the perturbation to the CNT electronic energy structure after covalent functionalization. DFT computational modeling suggests that the introduction of an  $sp^3$  carbon defect in the extended  $sp^2$  graphitic lattice splits the van Hove singularities which creates a new, defect activated intra-bandgap electronic energy level.<sup>72</sup> This defect state has been observed empirically as redshifted photoluminescence after the incorporation of defects in the nanotube sidewalls.<sup>72,73,146</sup> An energy state that resides below the  $E_{11}$  excitonic state could also serve as a trapping state or potential well-like deviation within the extended nanotube electronic structure. Such a trapping state could be capable of capturing excess electrons that promote the propagative chemistry we have just discussed.

We observe that the propagative Billups-Birch reaction not only enables the retention of desirable optical properties, but also generates new optical features. Specifically, we will discuss how defect activated potential wells in the electronic structure of SWCNTs under conditions which are highly doping result in the formation of charged excitons, also known as trions, which radiatively recombine even further redshifted into the near-IR than defect activated photoluminescence alone.<sup>72,146</sup>

# Chapter 4: Trion Photoluminescence of Covalently Functionalized, Semiconducting carbon nanotubes

*Adapted from Brozena, A.H.; Leeds, J.D.; Zhang, Y.; Huang, J.; Ng, A. Fourkas, J. T.; Wang, Y.H. to be submitted.<sup>147</sup>*

*A.H. Brozena synthesized all the samples, dispersed them and took the Raman, absorbance, and photoluminescence spectroscopy including the data forming the van't Hoff plot. J.D. Leeds dispersed many of the samples, measured the van't Hoff plots, fit the cubic spline curve to the positive trion photoluminescence samples for background correction. Y. Zhang established the defect activation of the  $E_{11}$  peak. J. Huang and A. Ng constructed carbon nanotube thin films for transistor measurements.*

## Introduction

Charged excitons, or trions, are quasi-particles that are composed of two electrons and one hole (or vice versa). Trions were theoretically predicted in semiconductor materials several decades ago<sup>74</sup> and were first observed in quantum dots in the 1990s.<sup>75,76</sup> Predictions suggested that trions should also be stable in SWCNTs,<sup>148</sup> which was verified by recent observations.<sup>149–151</sup> Strong Coulomb interactions occurring in such low-dimensional systems increase the trion binding energy (the energy required to strip the extra carrier from the exciton), making it possible to differentiate trion and exciton relaxation in the photoluminescence spectra of quantum-confined structures.<sup>152</sup>

Trion photoluminescence in SWCNTs has been observed under conditions that promote excess charge carriers. These excess carriers are necessary to generate the tri-carrier species after photoexcitation, which has been

accomplished by chemical or electrochemical doping techniques<sup>149,150</sup> and multi-exciton generation using high-power lasers.<sup>151</sup> In all cases, SWCNT trion emission was found to be chirality dependent and was redshifted from the E<sub>11</sub> exciton photoluminescence.<sup>149–151,153</sup> This redshift could have important implications for bio-imaging<sup>18</sup> and bio-sensing<sup>154,155</sup> applications of SWCNTs in the near-IR, tissue-transparent window.<sup>19,78</sup>

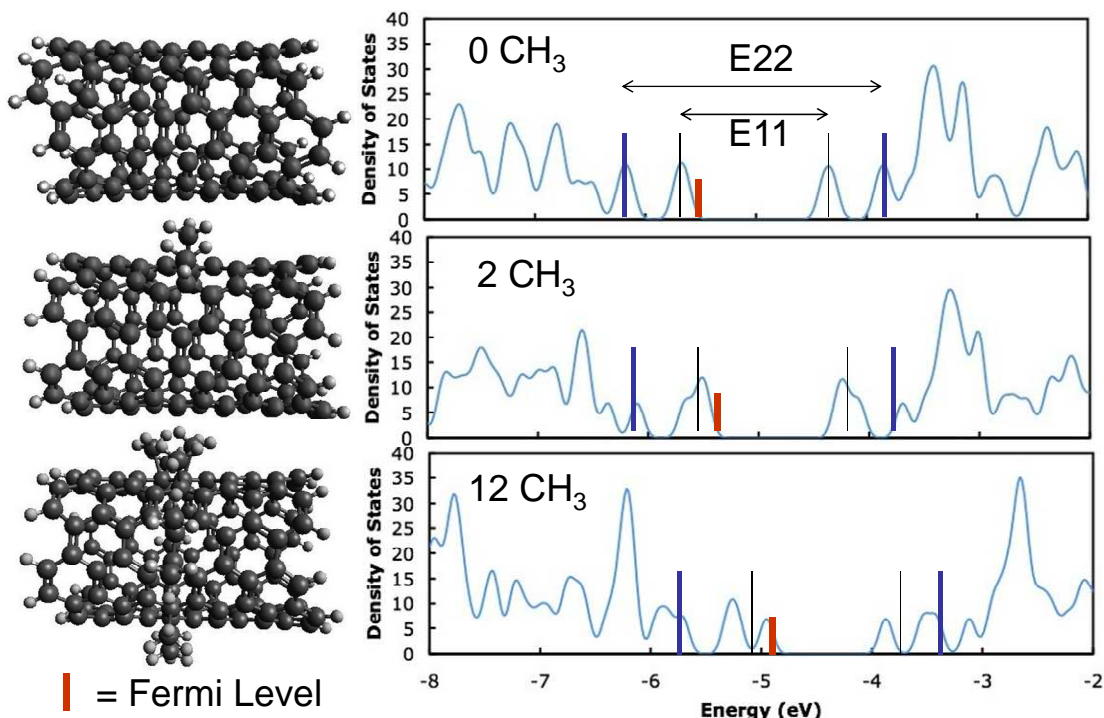


**Figure 4-1.** DFT modeling reveals the splitting of the energy states that make up the SWCNT E<sub>11</sub> transition as covalent functionalization increases.<sup>72</sup>

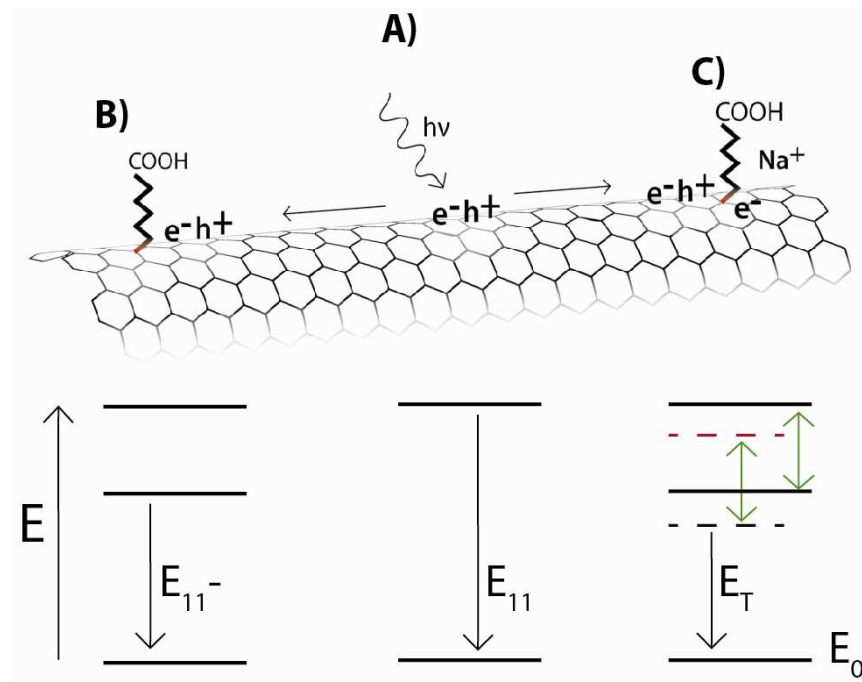
Here, we show for the first time that trion photoluminescence can occur with high stability in covalently functionalized SWCNTs, in which controlled sp<sup>3</sup> defects have been introduced into the sp<sup>2</sup> carbon lattice. SWCNTs were covalently functionalized by two distinct methods: Billups-Birch propagative sidewall alkylcarboxylation chemistry using sodium charged liquid ammonia<sup>71,72,133</sup> and diazonium salts *in situ* generated in oleum (100%, 20% free

$\text{SO}_3$ ).<sup>156</sup> Trion photoluminescence is observed as a new peak in the emission spectra of individually-dispersed, covalently functionalized (6,5) SWCNTs. This new peak is redshifted by ~260 meV from the  $E_{11}$  transition. It was monitored as covalent functionalization and doping conditions were changed, revealing a strong defect dependence that is distinct from previous observations of SWCNT trions. This new emission was observed for multiple covalent chemistries, which suggests a potentially universal behavior for covalently functionalized and doped SWCNTs.

These observations can be understood in terms of the simultaneous trapping of excitons and electrons or holes at controlled  $\text{sp}^3$  defects on the SWCNT sidewalls. At low densities, these functional defects split the doubly degenerate frontier molecular orbitals to create localized potential wells at defect sites along the nanotube. These defect states trap excitons and result in defect-dependent photoluminescence that is red-shifted from the  $E_{11}$  transition for (6,5) SWCNTs (Figure 4-1).<sup>72,73</sup> These defect states trap excitons and result in a defect-dependent photoluminescence that is redshifted from the  $E_{11}$  transition for (6,5) SWCNTs.<sup>72,146</sup> Our previous study on “banded” functionalized SWCNTs also suggests that electrons added into the system by chemical reduction are preferentially localized at these same types of covalent defect sites in the nanotube carbon lattice.<sup>71</sup>

Due to the combination of functionalization and doping, an exciton in a covalently functionalized SWCNT has three different radiative pathways (Scheme 1): A) recombination within the non-functionalized regions of the SWCNT,

leading to retention of  $E_{11}^-$  photoluminescence, B) trapping at a non-doped defect site, resulting in the previously observed defect-activated, redshifted photoluminescence, denoted  $E_{11}^-$ <sup>72,146</sup> or C) under highly reducing or oxidative conditions, diffusion to an electron- or hole-doped defect site, forming a trion that decays to produce the photoluminescence peak,  $E_T$ . The  $E_T$  is even further redshifted than  $E_{11}^-$  due to the lowering of the trion energy relative to the defect-induced potential-well energy.



**Scheme 4-1.** Proposed exciton diffusion pathways of a functionalized carbon nanotube under reducing conditions. Energy level diagrams for (A) the non-functionalized (B) non-doped and (C) doped defect sites. Ground state energy levels are not absolute and are pictured to illustrate the relative energy differences among the different excited levels. The observed emissions occur from the  $E_{11}^-$ , the defect activated  $E_{11}^-$  and the  $E_T$  trion photoluminescence transitions, respectively. The dashed lines of the doped energy level diagram (C) corresponds to the trion energy at non-perturbed (red) and defect sites (black) in which the defect generated trion energy level is depressed by approximately the same amount of energy as the difference between the  $E_{11}$  and  $E_{11}^-$  transition (green double arrows).

We seek to understand the effects of covalent functionalization and doping on the electronic structure of semiconducting SWCNTs based on changes to the optical spectra. SWCNTs that are functionalized using highly reducing or oxidative conditions exhibit new photoluminescence peaks that are consistent with the formation and relaxation of trapped trions. This unexpected phenomenon provides a spectral feature that allows one to probe covalent defects in semiconducting SWCNTs.

## Materials and Methods

### *Covalent Functionalization Chemistries*

All reagents were purchased from Sigma Aldrich unless stated otherwise. CoMoCat (6,5) SWCNT's (SouthWest NanoTechnologies) were functionalized with hexanoic acid groups by cycling the Billups-Birch reduction 1 to 3 times using sodium (99%) and 6-bromohexanoic acid (97%) in liquid ammonia (Airgas, 99.9%) condensed by an acetone/dry-ice bath, followed by purification with nanopure water as per our previously published procedure<sup>71</sup> without aqueous extraction. (6,5) SWCNTs were also reduced using the Billups-Birch conditions, but without functionalization, by dispersing the starting material in liquid ammonia with sodium overnight. Functionalized or pristine SWCNTs were dispersed in oleum for 4 hrs and washed with copious water until the filtrate pH returned to neutral.

4-nitrobenzene functionalized SWCNTs were synthesized using two different diazonium chemistries. The first reaction was an in-situ method in which

SWCNTs are individually dispersed in oleum (100%, 20% free SO<sub>3</sub>) along with 4-nitroaniline (99+%), sodium nitrite ( $\geq 97\%$ ) and 2,2'-azobis(2-methylpropionitrile) (98%).<sup>156</sup> The functionalized sample was purified by quenching and washing with excess water and ethanol. After oven-drying, the sample was reduced by 0.75 or 1.5 mole equivalents of sodium (with respect to moles of carbon) in liquid ammonia and purified the following day using the same procedure as was used for the purification of Billups-Birch alkylcarboxylated samples.

The second diazonium reaction employed 4-nitrobenzene diazonium as previously reported.<sup>157</sup> CoMoCat(6,5) SWCNTs were individually dispersed in 1 wt% SDS-D<sub>2</sub>O solution at a concentration of 30.2 mg/L. The SWCNTs were then functionalized by stirring the dispersed nanotubes with the freshly synthesized 4-nitrobenzene diazonium compound in a mole ratio of 300:1 for 24h in a light-shielded bottle to prevent degradation of the diazonium material. After 24 hrs, the solution was added to ethanol to remove surfactant and subsequently filtered, washed and oven-dried at 80 °C overnight. Part of the diazonium functionalized (6,5) SWCNTs were re-dispersed in 1 wt% SDDBS-D<sub>2</sub>O, the rest was reduced using the Billups-Birch conditions in approximately 35 mL liquid ammonia. The reduced material was purified and subsequently re-dispersed in 1 wt% SDDBS-D<sub>2</sub>O for spectral analysis.

## *Spectroscopy*

For spectroscopic analysis, all samples were dispersed in 1 wt% SDBS {Hard type, TCI-Japan}-D<sub>2</sub>O (99.8% Cambridge Isotope Laboratories, Inc.) by probe-tip ultrasonication using a Misonix S-4000 Ultrasonicator (Farmingdale, NY) at an average power of 33W for 2 hrs in a water cooled, stainless steel beaker, followed by ultracentrifugation with a Beckman Coulter Optima LE-80K Ultracentrifuge (Brea, CA) at 61,034g for 2 hrs to remove bundles. For the aqueous phase diazonium chemistry, SWCNTs were dispersed in 1 wt% SDS-D<sub>2</sub>O using the same procedure.

All surfactant dispersed samples were diluted to an optical density of approximately 0.2 at the (6,5) E<sub>11</sub> absorption peak and monitored with a Perkin Elmer Lambda 1050 UV-Vis-NIR spectrometer (Waltham, MA) and a Horiba Jobin Yvon NanoLog Spectrofluorometer (Edison, NJ). The 970 nm excitation wavelength was produced using an external diode laser and a Thorlabs 1050 nm long pass filter (Newton, NJ). For Raman spectroscopy, surfactant was removed from the dispersed samples by immersion in ethanol, followed by drop-casting the flocculated material on a microscope slide. Raman scattering was taken on a Horiba Jobin Yvon LabRAM HR800 Raman microscope (Edison, NJ) by averaging spectra from three different spots of the dried sample.

The van't Hoff plot was constructed by monitoring the integrated peak areas of the E<sub>11</sub> and E<sub>11</sub><sup>-</sup> photoluminescence of the Billups-Birch reacted

CoMoCat(6,5) samples as temperature was adjusted via water cooling and under magnetic stirring of the sample. Cuvette temperature was ramped up and down between approximately 10-90 °C while the photoluminescence was monitored at discrete temperature points. Peak areas of E<sub>11</sub> and E<sub>11</sub><sup>-</sup> emissions were fit using a Voigt area peak-shape with PeakFit v4.12 software.

SWNT TFTs were constructed by adapting a previously established procedure.<sup>26</sup> 1.0 mL of 1% SDBS-D<sub>2</sub>O dispersed functionalized or control CoMoCat (6,5) SWNT samples were vacuum filtered over 0.05 μm VMWP cellulose ester filter paper (Millipore), followed by 5 minutes drying with applied vacuum, washed with 30 mL nanopure water, and dried for an additional 5 minutes over the filtration apparatus. Thin films were then transferred to a silicon substrate by 1 hr compression and heating at 95 °C, followed by removal of the filter paper by applying an acetone vapor bath for approximately 24 hrs. 50 nm thick gold electrodes were thermally evaporated on the SWNT thin film with a 10 nm chromium adhesion layer. Devices were accessed using both a Keithley 4200 Semiconductor Characterization System (Cleveland, OH) and a Desert Cryogenics TT Microprobe (Tucson, AZ) pumped down with a turbo-ion pump.

## Results and Discussion

### *Photoluminescence of Negative Trions*

Hexanoic acid functional groups were covalently attached to CoMoCat (6,5) SWCNT sidewalls via propagative alkylcarboxylation using the Billups-

Birch reduction.<sup>71,125</sup> This chemistry was repeated as desired to increase the functional degree with each reaction cycle.<sup>72</sup>

The functionalized samples were subsequently dispersed with 1 wt% sodium dodecylbenzenesulfonate (SDBS) in D<sub>2</sub>O for spectroscopic studies. Excitation of the (6,5) E<sub>22</sub> transition (570 nm) revealed two new emission features at 1092 nm and 1225 nm (Figure 1). These peaks are labeled E<sub>11</sub><sup>-</sup> and E<sub>T</sub> and correspond to respective energy shifts of 136 and 262 meV from the (6,5) E<sub>11</sub> exciton transition (973 nm). As the functionalization degree increases with each alkylation cycle,<sup>71</sup> E<sub>11</sub> photoluminescence intensity becomes progressively weaker, while the relative intensity of E<sub>11</sub><sup>-</sup> and E<sub>T</sub> are maximized after 2 cycles. The absolute photoluminescence intensity decreases after 3 reaction cycles due to decreased SWCNT absorption with increasing covalent functionalization.<sup>72</sup>

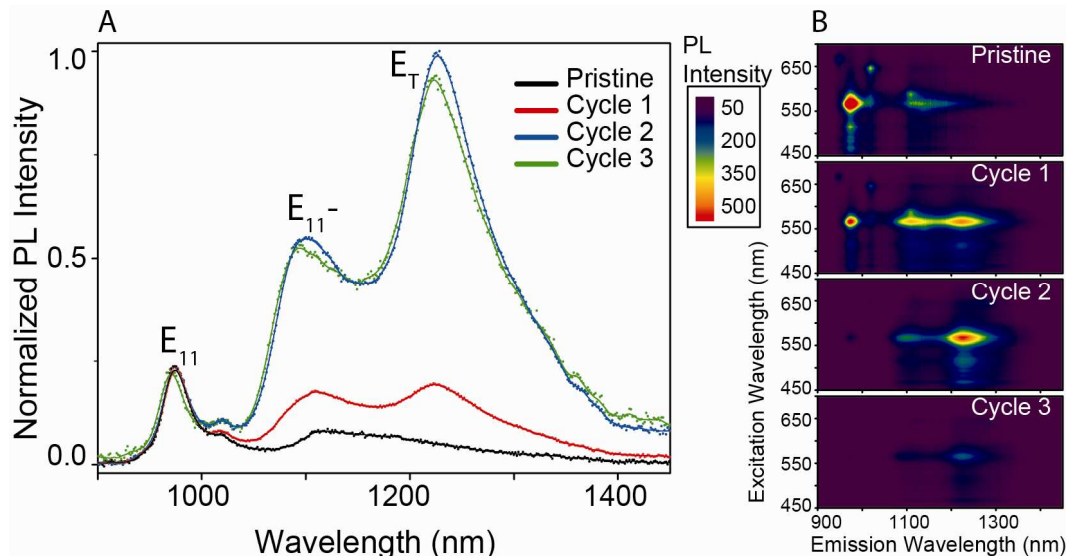


**Figure 4-2.** (A) Sidewall propagative alkylcarboxylation of (6,5) SWCNTs produces two new photoluminescence peaks, E<sub>11</sub><sup>-</sup> and E<sub>T</sub>, in addition to the E<sub>11</sub> exciton transition. The photoluminescence peaks are normalized by the E<sub>11</sub> intensity to show change in the ratio of E<sub>11</sub><sup>-</sup> and E<sub>T</sub> with increased functionalization degree/reaction cycle. (B) Excitation-emission photoluminescence maps of the functionalized samples.

The  $E_{11}^-$  and  $E_T$  emission is observed upon excitation of the  $E_{11}$  (970nm) or the  $E_{22}$  transition of (6,5) SWCNTs indicating that these two new peaks are generated by the (6,5) species (Figure 4-3). The weak emission features between 1100-1200 nm of the non-functionalized SWCNT control sample arise from (8,4) and (9,2) SWCNTs also present in the starting material. Excitation wavelength studies rule out these impurities as the cause of the  $E_{11}^-$  and  $E_T$  peaks (Figure 4-4). These new photoluminescence features did not appear in the absorption spectrum of the functionalized SWCNTs (Figure 4-5).

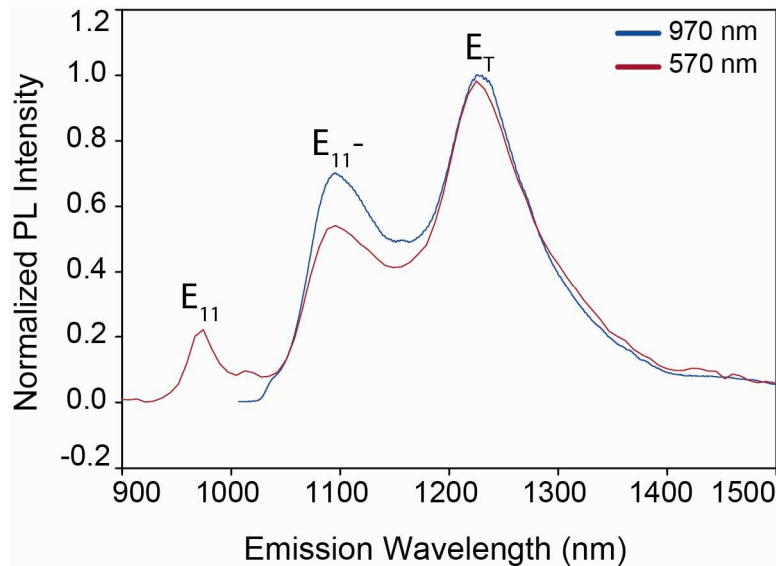


**Figure 4-3.** Photoluminescence emission spectra of 3 cycles Billups-Birch alkylcarboxylated SWCNTs using 970 and 570 nm excitation wavelengths (corresponding to the  $E_{11}$  and  $E_{22}$  (6,5) transitions respectively), normalized to the  $E_T$  peak.

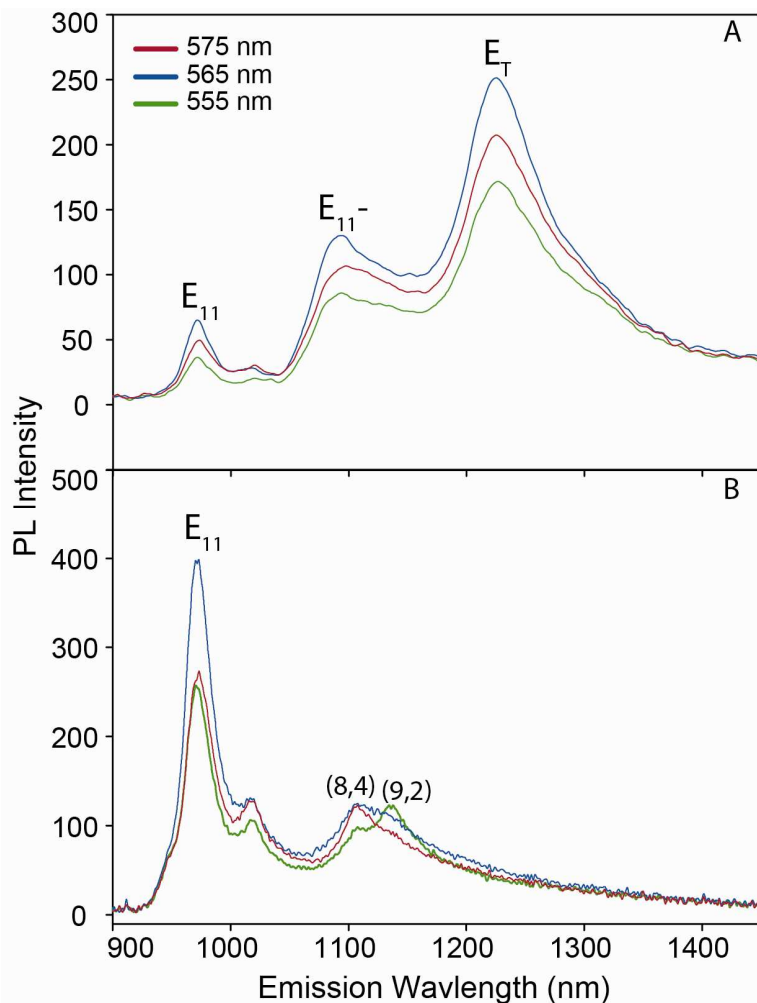


**Figure 4-4.** Emission spectra of (A) alkylcarboxylated SWCNTs after 3 cycles of the Billups-Birch alkylcarboxylation and (B) pristine SWCNTs. Excitation line dependence confirms that the  $E_{11}^-$  and  $E_T$  features are excited at the same wavelength as the  $E_{11}$  transition, as all three peaks come into resonance at 565 nm (the (6,5)  $E_{22}$  excitation wavelength). Changing the excitation wavelengths for the pristine SWCNT material does not reveal either the  $E_{11}^-$  or  $E_T$  peaks, indicating that these emissions are related to the functionalized species.

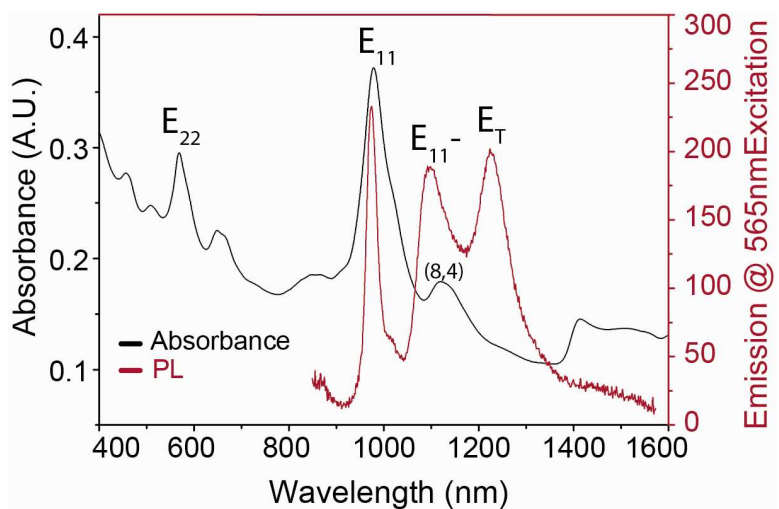


**Figure 4-5.** Photoluminescence and absorption spectra of SWCNTs functionalized by 1 cycle of the Billups-Birch alkylcarboxylation reaction. Resonant excitation at  $E_{22}$  of sidewall alkylcarboxylated (6,5) SWCNTs produces photoluminescence features at  $E_{11}$ ,  $E_{11}^-$ , and  $E_T$  (red), but these new features do not appear in the absorption spectra (black).

A previous study of this same reaction by Zhang et al. revealed the addition of covalent defects to the nanotube sidewalls using Raman spectroscopy. Density functional theory (DFT) calculations demonstrated that this introduction of  $sp^3$  defects into the  $sp^2$  carbon lattice generated the  $E_{11}^-$  photoluminescence due to the splitting of the  $E_{11}$  van Hove transition. This splitting results in an optically active intra-bandgap state that is redshifted from  $E_{11}$ . Consistent with the computational results, the energy shift of the  $E_{11}^-$  peak was found to depend on the identity of the functional group.<sup>72</sup>

This propagative alkylcarboxylation reaction uses sodium in liquid ammonia to reduce SWCNTs for electrostatic dispersion and to generate alkyl radicals for covalent functionalization by single-electron transfer from the reduced nanotubes. It is therefore possible that this chemistry n-dopes the SWCNTs. Such doping is conducive to the formation of trions, which would be

redshifted from  $E_{11}$  in the photoluminescence spectrum.<sup>150</sup> To test this hypothesis, the Billups-Birch-functionalized SWCNTs were dispersed in oleum to counteract potential n-doping effects. The sample was washed with copious water to remove excess protons from the super-acid treatment, and then dispersed with 1 wt% SDBS-D<sub>2</sub>O for spectroscopic studies.

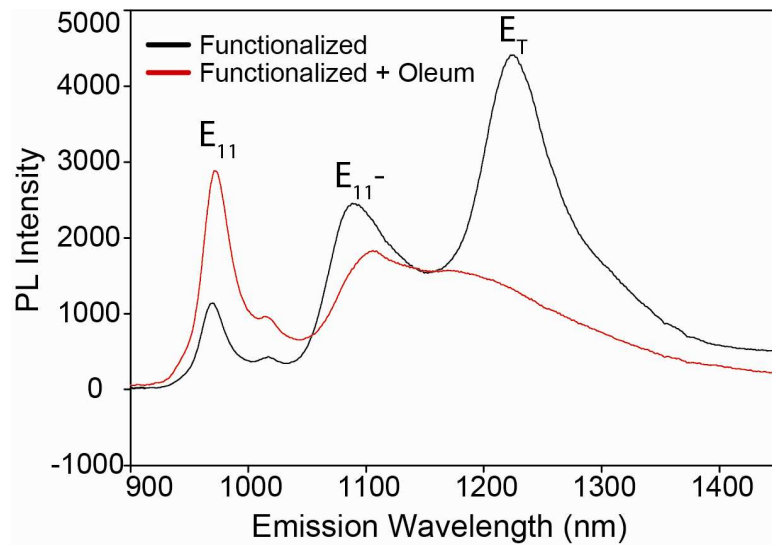


**Figure 4-6.** Emission spectra of 1 wt% SDBS-D<sub>2</sub>O suspended (6,5) SWCNTs functionalized by hexanoic acid groups using the 3 cycles of the Billups-Birch reduction before (black) and after (red) dispersion in oleum show the change in the intensity of the  $E_T$  peak as reducing conditions are removed.

The resulting photoluminescence spectrum shows a striking decrease in the intensity of the  $E_T$  peak that is also visible in the 3-D excitation-emission photoluminescence maps (Figure 4-6). However, the retention of the  $E_{11}^-$  defect-activated peak indicates that the nanotubes are still functionalized after superacid treatment, although  $E_{11}^-$  is redshifted by 45 nm relative to that sample that was not treated with oleum (Figure 4-7). The increase in the  $E_{11}$  emission intensity after dispersion in oleum is consistent with a decreased doping concentration. SWCNT photoluminescence is well known to be highly sensitive to the presence of

dopants (Figure 4-6).<sup>16,150,158</sup> Additionally, the absorption spectrum regains intensity after dispersion in oleum (Figure 4-8), which implies that dispersing the previously sodium-reduced SWCNTs in superacid helps to counteract the effects of electron doping and thus decreases dopant concentration. The use of highly reducing conditions to generate the  $E_T$  photoluminescence peak is consistent with the results of recent SWCNT trion studies, which used a variety of *in situ* methods to dope suspended SWCNTs with excess charge carriers.<sup>149–151</sup> Here, the change in intensity of  $E_T$  after oleum dispersion strongly suggests that the cause of this photoluminescence is related to the SWCNT doping, which supports the assignment of this new peak as trion emission.

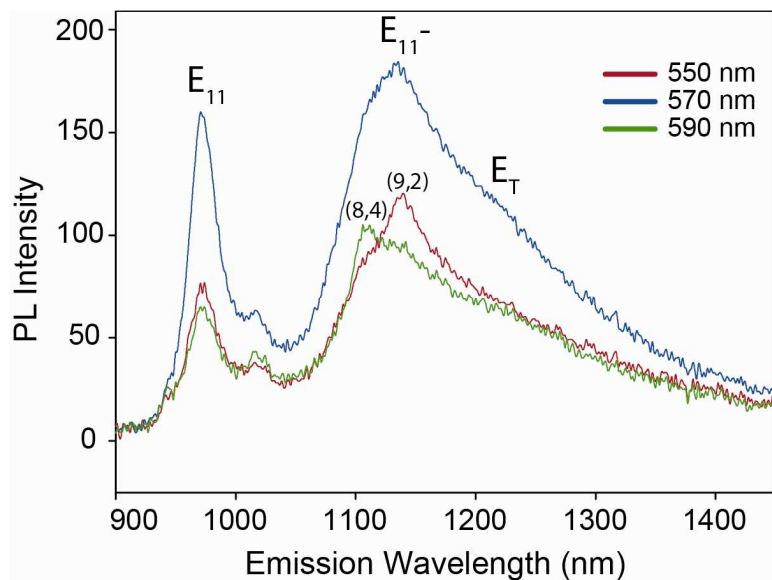


**Figure 4-7.** An excitation study of the 3 cycle Billups-Birch functionalized, oleum treated sample indicates the position of the  $E_{11}^-$  and  $E_T$  peaks that come into resonance at the same excitation as the (6,5)  $E_{11}$  transition. The  $E_T$  peak is greatly diminished in intensity compared to the functionalized sample alone (Figure 4-6), but the position does not appear to be as shifted as the defect activated  $E_{11}^-$ .

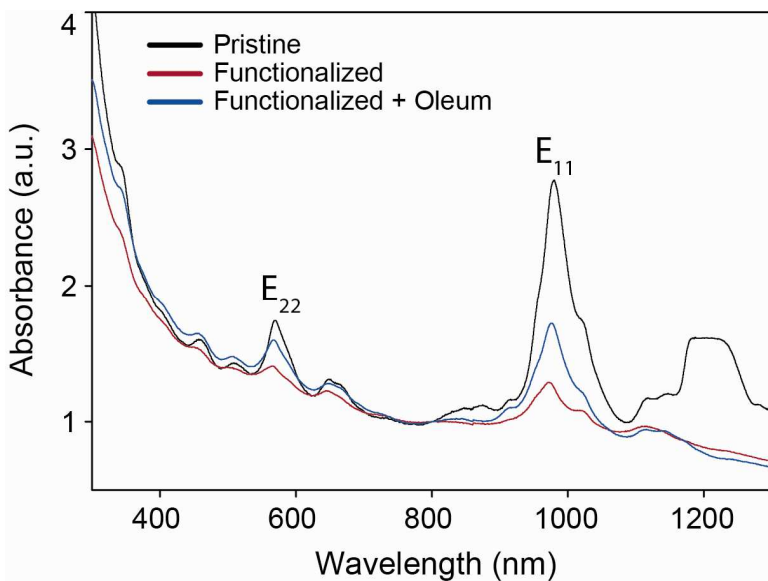


**Figure 4-8.** UV-Visible-NIR absorption spectra of the Billups-Birch alkylcarboxylated SWCNTs before and after oleum treatment. The partially regained  $E_{11}$  and  $E_{22}$  transition intensity after oleum treatment suggests dopant concentration has decreased.

Localized doping at covalent functional sites could also explain the observed redshift of the defect activated  $E_{11}^-$  peak after oleum treatment as shown in Figure 4-6. The splitting degree of the  $E_{11}$  energy level as a result of  $sp^3$  carbon atoms within the SWCNT  $sp^2$  lattice diminishes with distance from the defect site,<sup>72,73</sup> creating a distribution of molecular orbitals that can be filled upon doping by reductive chemistries such as the Billups-Birch, propagative alkylcarboxylation reaction used here. By dispersing these functionalized SWCNTs in oleum, the n-doped energy levels around the defect site become depleted, effectively lowering the possible energy level of the transition and resulting in the observed significant redshift of the  $E_{11}^-$  peak after superacid treatment.

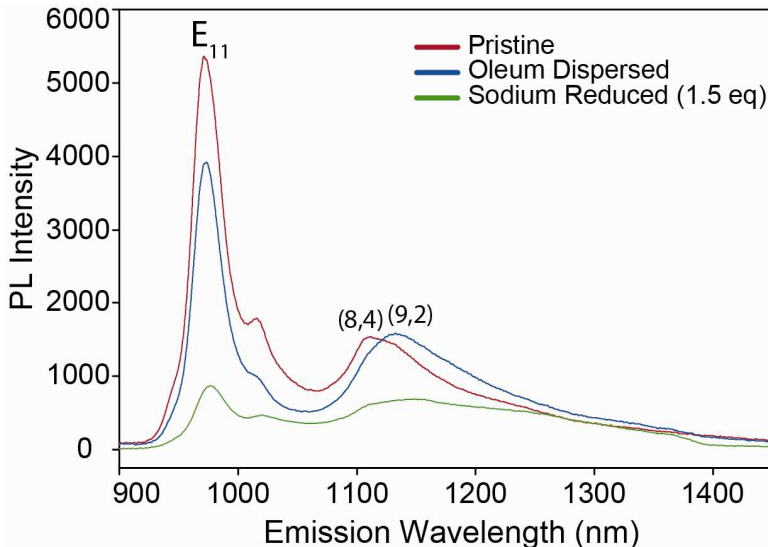


**Figure 4-9.** Dispersion of pristine SWCNTs in oleum or with sodium in liquid ammonia, without functionalization, fails to produce  $E_T$  in the photoluminescence spectra. The convoluted peak between 1100-1200 nm is due to (8,4) and (9,2) species also present in the starting material.

To test this defect hypothesis, non-functionalized, pristine SWCNTs were dispersed in either oleum or sodium and liquid ammonia alone without the addition of  $sp^3$  defects. No new peaks appeared in the photoluminescence spectra after this treatment (Figure 4-9). These controls indicate that defects are necessary for the successful reduction or oxidation of the nanotubes. Simultaneous reduction and functionalization of the SWCNTs produces the trion peak,  $E_T$  (Figure 4-2). However, when SWCNTs are reduced (or oxidized alone), without the addition or presence of defects (as shown by the lack of the  $E_{11}^-$  peak and retention of  $E_{11}$ ),  $E_T$  does not appear. This observation suggests that defects must either be simultaneously added during the reduction or be previously present to effectively dope the nanotubes. Doping is the ultimate requirement for trion generation.<sup>150</sup>

In contrast to previous SWCNT trion reports, which used *in situ* doping techniques without covalent functionalization,<sup>149–151</sup> the defect dependence of the

trion photoluminescence in this study is unique and is a possible cause of the observed trion emission stability. SWCNTs were doped during covalent functionalization, processed in water and air, and then spectrally probed. The  $E_T$  trion photoluminescence that is observed remains for several months after dispersion. This trion longevity may be explained by defect-induced stabilization of the doped charge carriers. Our previous works has shown that a covalent defect can split the doubly degenerate  $E_{11}$  frontier molecular orbitals, creating a potential well in the bandgap of a SWCNT.<sup>72</sup> This potential well state may trap charge carriers introduced by reduction, as suggested by DFT calculations.<sup>71</sup> Such trapping provides energetic protection from subsequent oxidation under the aqueous purification conditions, and enables the trion to form upon exciton diffusion to this doped defect site. This trapping effect may also explain why trion photoluminescence is observed well after the doping event.

The energy shift for the  $E_T$ , trion peak (262 meV) is larger than was observed in previous SWCNT trion studies, which reported a shift of ~170-190 meV relative to the  $E_{11}$  emission for the (6,5) nanotube chirality.<sup>149-151</sup> We hypothesize that the energy shift of the  $E_T$  emission observed for our alkylcarboxylated sample is greater due to trapping of trions at the chemically implanted defect sites. We know that this covalent functionalization splits the  $E_{11}$  state that traps excitons, resulting in the red-shifted excitonic photoluminescence observed (the  $E_{11}^-$  emission). Depression of this exciton level by trapping should similarly lower the trion energy level by approximately the same energy as long as the trion binding energy does not significantly change (as the trion state is

lower on the energy-scale compared to the exciton state by the amount of energy necessary to remove the extra carrier to form the exciton) (Scheme 1). Thus, we would expect that defect-bound trions to be red-shifted compared to previously observed, *in situ* trion photoluminescence, which has never been associated with covalent functional groups on the nanotube sidewalls.<sup>149–151</sup> Determining the well depth corresponding to these defects should reveal whether this hypothesis is consistent with the observed increased trion energy shift.

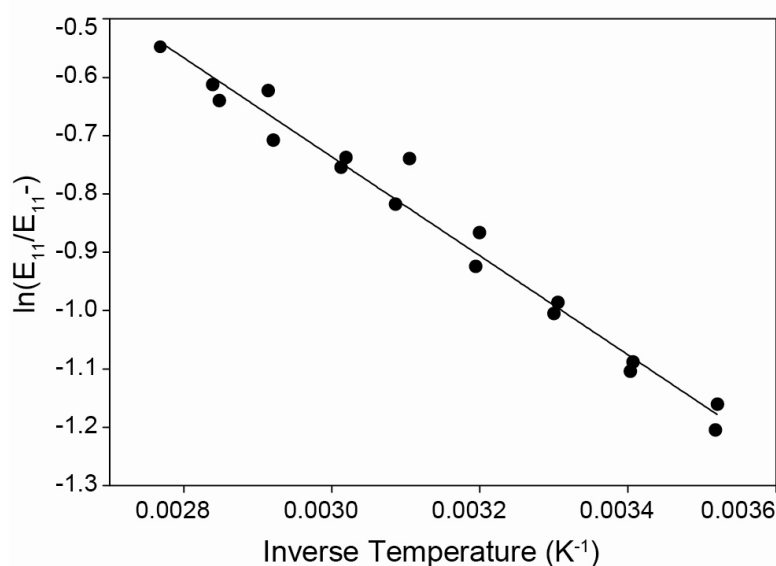


**Figure 4-10.** A van't Hoff plot was used to derive an average well depth of  $75.3 \pm 4.6$  meV/ $sp^3$  carbon atom for 3 cycle, Billups-Birch alkylcarboxylated (6,5) SWCNTs. Three replicate experiments were used to measure the slope of the fitted line and provide an average value for the well depth calculation. One plot is shown here as an example.

A van't Hoff plot constructed from the temperature dependent ratio of the  $E_{11}$  and  $E_{11}^-$  peaks enabled us to derive a  $75.3 \pm 4.6$  meV potential well depth for the implanted defects (Figure 4-10). Photoluminescence of the 3 cycle alkylcarboxylated SWCNT sample was monitored as temperature was ramped up and down between 10°C and 90°C. Changes in the ratio of the  $E_{11}$  and  $E_{11}^-$

integrated peak areas at different temperatures allow us to deduce the difference in energy between these two levels, which is effectively the well depth created by the covalent defect that generates  $E_{11}^-$ .<sup>73</sup> Previous SWCNT trion shifts for the (6,5) chirality were reported to range from approximately 170 meV to 190 meV.<sup>149–151</sup> An additional ~75 meV stabilization of the trion binding energy by lowering the singlet exciton energy level due to defect splitting accounts well for our observed 262 meV energy shift. This observation further supports our conclusion that the  $E_T$  peak observed after SWCNT functionalization by reductive alkylcarboxylation is due to defect-activated trions.

#### *Photoluminescence of Positive Trions*

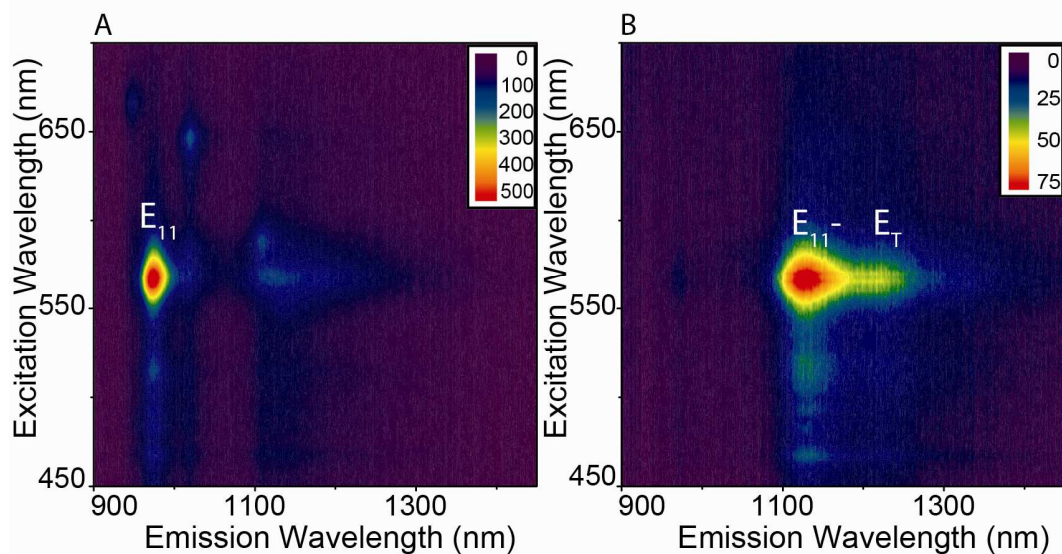


**Figure 4-11.** 3-D photoluminescence excitation-emission maps of (6,5) SWCNTs dispersed in 1wt% SDBS-D<sub>2</sub>O (A) before and (B) after covalent functionalization by 4-nitrobenzene groups using an in-situ diazonium chemistry in oleum. Two new peaks ( $E_{11}^-$  and  $E_T$ ) appear after functionalization at the same excitation as the (6,5)  $E_{11}$  peak.

As oleum was used to neutralize the effects of n-doping-generated trion photoluminescence, we were curious to test whether positive trions could be

observed using oleum based covalent chemistry. To this end, CoMoCat (6,5) SWCNTs were functionalized with 4-nitrobenzene groups using an *in situ* diazonium synthesis in oleum.<sup>156</sup> Normally, carbon nanotube-diazonium salt reactions are initiated by electron transfer from the nanotube to the diazonium salt species for a loss of N<sub>2</sub> followed by radical addition of the remaining benzene molecule to the nanotube surface.<sup>60,159</sup> However, because the chemistry used here takes place in oleum, nanotube sidewall protonation makes electron transfer from the SWCNT to the diazonium salt unlikely. Instead, a radical initiator is utilized to generate radicals on the nanotube sidewalls that are reactive with close proximity diazonium salts.<sup>156</sup> As with the alkylcarboxylated SWCNTs, two new peaks appeared in the photoluminescence excitation-emission maps after functionalization with this superacid chemistry (Figure 4-11). These new peaks were labeled E<sub>11</sub><sup>-</sup> and E<sub>T</sub> and have energy shifts of 174 meV and 264 meV respectively, relative to the (6,5) E<sub>11</sub> emission at 970 nm. The shift in the position of E<sub>11</sub><sup>-</sup> compared to the hexanoic-acid-functionalized SWCNTs by the Billups-Birch reduction is explained by the difference in the electron withdrawing capacity of the functional groups.<sup>146</sup> An excitation study of the functionalized SWCNTs clearly indicates that these new E<sub>11</sub><sup>-</sup> and E<sub>T</sub> features appear at the same excitation wavelength as the (6,5) species and are not due to chiral impurities, which are excited at different wavelengths (Figure 4-12).

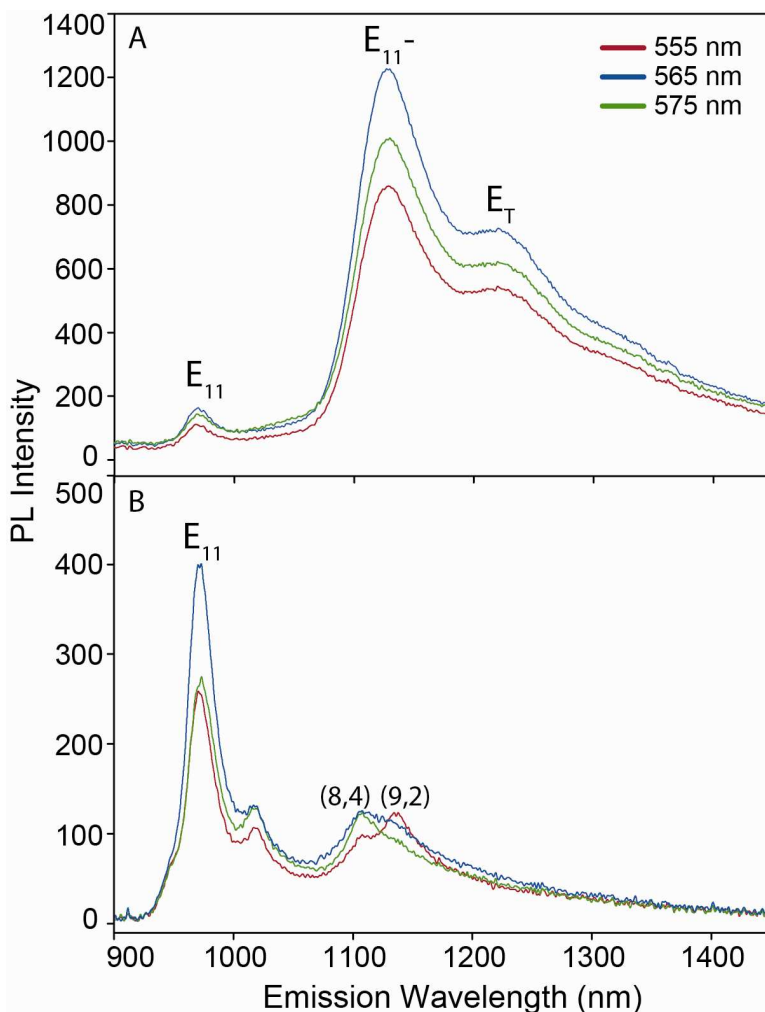


**Figure 4-12.** Multi-line excitation study of (A) 4-nitrobenzene functionalized and (B) pristine SWCNTs reveal that  $E_{11}^-$  and  $E_T$  are in resonance with the (6,5)  $E_{11}$  transition. (8,4) and (9,2) species convolute, but are not excited at the same wavelengths as (6,5).

Raman spectroscopy of the functionalized SWCNT sample shows an increased ratio of the D ( $\sim 1350 \text{ cm}^{-1}$ ,  $\text{sp}^3$  hybridized carbons atoms) and G peak areas ( $\sim 1585 \text{ cm}^{-1}$ ,  $\text{sp}^2$  hybridized) compared to the non-functionalized SWCNT starting material. This observation indicates that covalent functionalization occurs on the SWCNT sidewalls after applying this superacid chemistry (Figure 4-13).

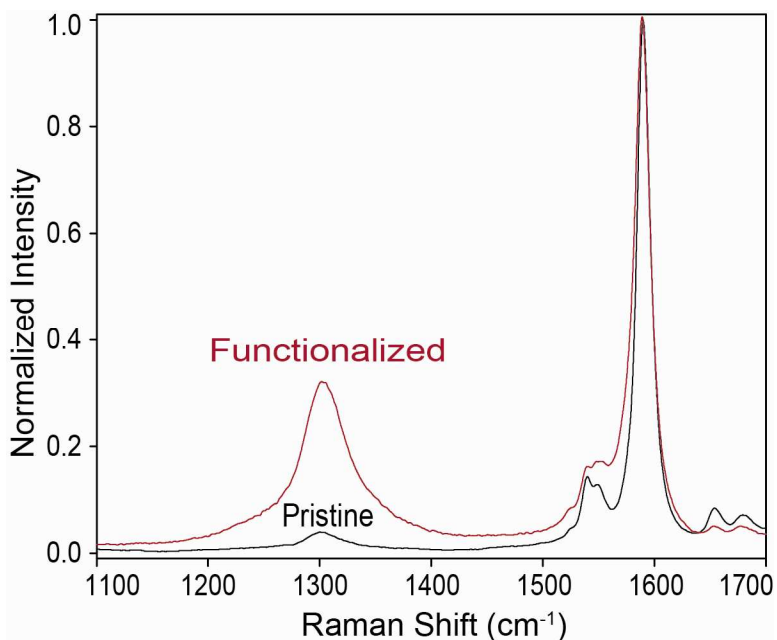


**Figure 4-13.** Raman spectra of pristine and 4-nitrobenzene functionalized SWCNTs. The D/G ratio increases after the in-situ diazonium synthesis reaction, indicating that some native  $sp^2$  hybridized carbons on the SWCNT sidewalls have been converted to  $sp^3$  after covalent addition.

This covalent chemistry uses oleum to individually disperse SWCNTs for functionalization by protonating the weakly basic nanotubes and enabling intercalation of the sulfate ion, which electrostatically exfoliates the nanotubes apart in solution. This process could hole-dope the SWCNTs. To test whether the  $E_T$  peak has any relation to the SWCNT oxidative state, we reduced the oven-dried, functionalized sample with sodium in liquid ammonia to observe possible changes in the photoluminescence spectrum. After reduction, the sample was re-dispersed with 1wt% SDBS-D<sub>2</sub>O for spectral analysis.

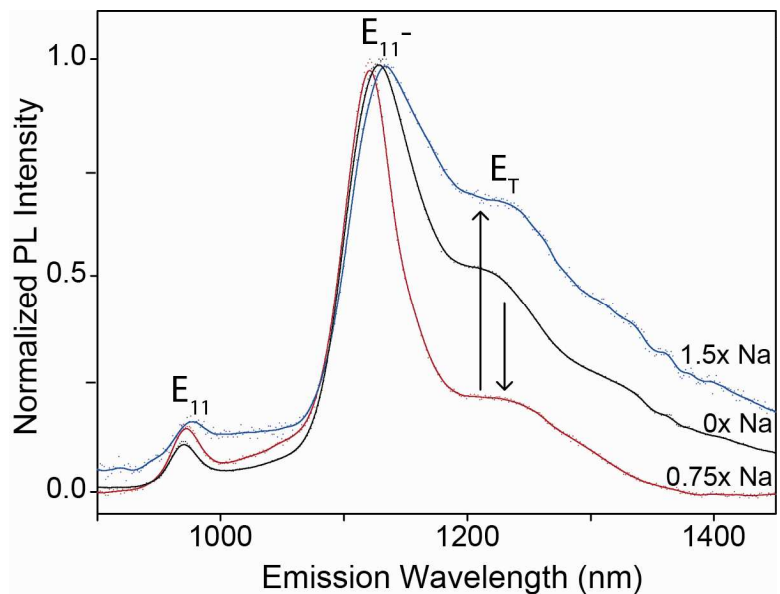


**Figure 4-14.** Modulation of the 4-nitrobenzene functionalized SWCNT  $E_T$  peak is accomplished through subsequent reduction by different numbers of sodium equivalents relative to the number of carbon moles that make up the functionalized SWCNT sample. The spectra are normalized to the  $E_{11}^-$  peak as the intensity of  $E_{11}$  changes dramatically after doping concentrations are modified but the ratio of  $E_{11}^-$  to  $E_{11}$  remains almost constant due to the unchanging functional degree of the sample.

Adding 0.75 equivalents of sodium relative to the number of carbon moles that make up the functionalized SWCNT sample resulted in a substantial drop in the  $E_T$  peak in comparison to the defect activated  $E_{11}^-$  (Figure 4-14). However, treatment with 1.5 equivalents of sodium reduction led to an increase in the intensity of  $E_T$ . The Raman spectra of these reduced samples changed little compared to the functionalized-alone material (Figure 4-15).

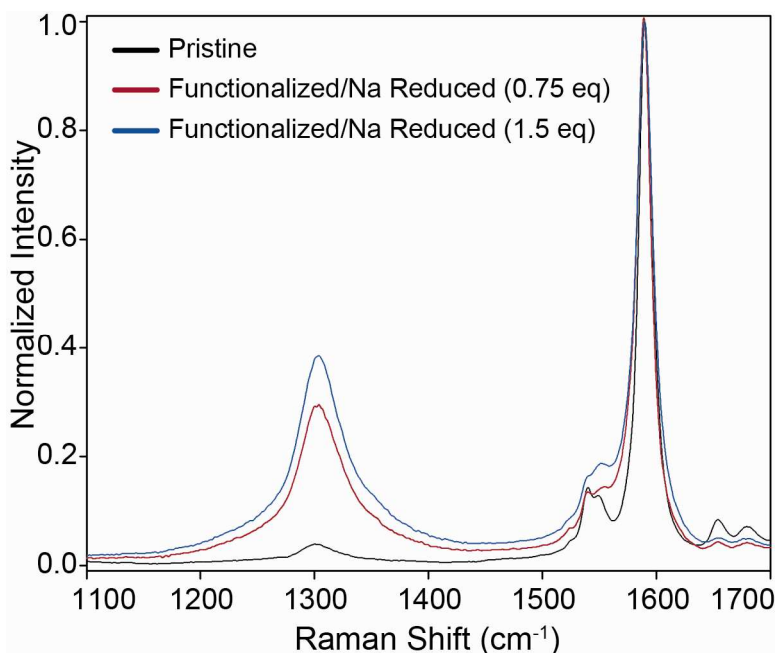


**Figure 4-15.** Raman spectroscopy of 4-nitrobenzene SWCNTs functionalized in oleum and subsequently dried and reduced with varying equivalents of sodium in liquid ammonia. The D/G ratio does not substantially change after reduction compared to the functionalized sample (Figure 4-13).

These results reveal the relation of the  $E_T$  peak to the oxidative state of the SWCNTs. If we assume that the 4-nitrobenzene functionalized SWCNTs are hole-doped after synthesis in oleum, then the addition of 0.75 equivalents sodium effectively reduces the nanotubes. However, after treatment with double that amount of sodium, we observed that  $E_T$  increased. It is difficult to know the exact concentration of SWCNT hole dopants under these conditions (and there is probable sidewall protonation that reacts with the added sodium as well); quantification of the dopant concentration will require better controlled titration experiments. However, we can explain this increase in  $E_T$  if the 1.5 equivalents of sodium reduced the SWCNT and exceeded the initial hole dopant concentration, thus leaving the SWCNTs in a reduced state as opposed to an oxidized state. The

resultant increase in the  $E_T$  intensity suggests that this photoluminescence peak serves as an indicator of the dopant concentration of either charge nature.

These changes in the intensity of  $E_T$  as a function of doping are also reflected in the peak shift and width changes of  $E_{11}^-$  (Figure 4-16). Before sodium reduction, the  $E_{11}^-$  peak of the 4-nitrobenzene functionalized sample occurred at 1126 nm, with a full width at half maximum (FWHM) of 44 nm. After reduction by 0.75 equivalents sodium, the  $E_{11}^-$  FWHM decreased to 37 nm, and the peak position blue-shifted slightly to 1124 nm. SWCNT optical spectra are highly sensitive to dopants, demonstrating significant peak intensity loss and broadening with increasing dopant concentration.<sup>158</sup> The decrease in FWHM of  $E_{11}^-$  after reduction suggests that the injected electrons serve to at least partially cancel out the hole-dopants created during the original oleum synthesis, lessening the doping concentration. This process also causes the decrease in  $E_T$  trion emission intensity. Given the defect-dependent doping hypothesis we have constructed, 0.75 equivalents of added sodium may seem far in excess to the actual number of implanted, p-doped  $sp^3$  defects (<5% of total carbon atoms).<sup>71</sup> However, we account for the observed decrease in doping due to parasitic reaction with protons physisorbed to the nanotube sidewalls after functionalization in oleum, effectively canceling out the excess sodium.

However, the addition of 1.5 equivalents of sodium redshifts  $E_{11}^-$  to 1127 nm and broadens the FWHM to 45 nm, which indicates that the dopant concentration has increased compared to the 0.75 equivalent sodium addition. In this case, the sample is likely in the n-doped regime, which could explain the

simultaneous increase in the dopant-dependent  $E_T$  peak. The previous control demonstrated that sodium reduction of nanotubes alone without functionalization does not generate the  $E_T$  emission, due to what we believe is the defect dependence of trions generated under these conditions (Figure 4-9). The reduction and oxidation of the 4-nitrobenzene functionalized SWCNTs demonstrates both positive and negative trion photoluminescence, which were previously observed at nearly identical positions due to the small effective mass difference between holes and electrons.<sup>150</sup> However, some difference in trion shift may in fact be the case here, but is difficult to resolve due to the background emission of other chiralities present within the sample. A (6,5) purified SWCNT sample (using gel chromatography methods for instance<sup>41</sup>) subjected to these covalent chemistries would remove any ambiguity of the positive and negative trions energy shifts, however scale becomes an obstacle to the combination of these techniques.

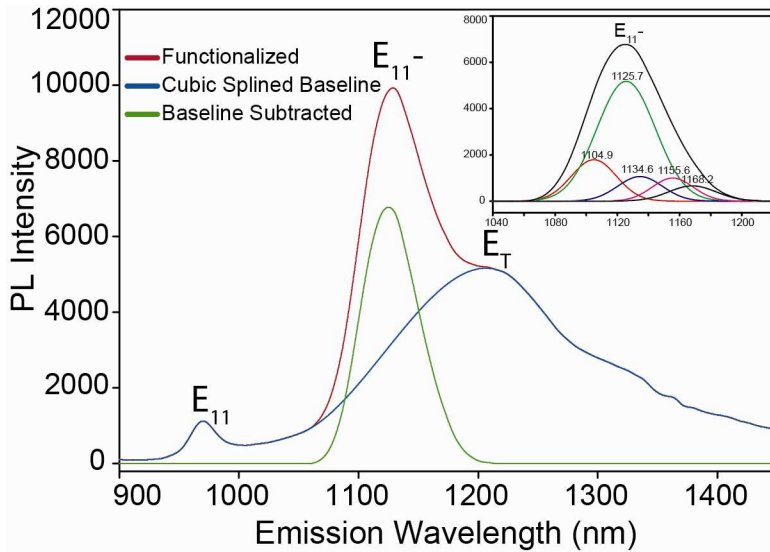


**Figure 4-16.** The peak at 1125 nm for the 4-nitrobenzene functionalized SWCNT sample contains convoluted data from multiple nanotubes in solution. In order to de-conolute and analyze this data, it was smoothed with a first degree Loess polynomial with sampling proportion set to 0.02 (Systat – SigmaPlot 10). A cubic baseline was fit across the peak from 1056 -1215 nm using LabVIEW. This Baseline was subtracted from the data and multiple Voigt-area peaks were fit using Systat PeakFit corresponding to several other chiralities in solution as well as a defect activated peak. Excluding the 1126 nm peak, going from short to longer wavelengths, the 4 other fitted peaks correspond to (8,4), (9,2), (10,0) and(8,6) species also found in low concentration in the solution. The same analysis and peak fit was applied to the 0.75 and 1.5 equivalents sodium reduced 4-nitrobenzene functionalized SWCNT samples corresponding to Figure 4-14 in order to derive  $E_{11}^-$  peak positions and FWHM values.

#### *SWCNT Trion Defect Dependence*

In both the negative and positive trion chemistries,  $E_T$  failed to appear in the absence of defects. To better understand the defect dependence of  $E_T$ , we used an alternative chemistry to generate SWCNT defects under conditions that were neither highly reductive nor oxidative. These experiments allowed us to separate the effects of functionalization and reduction/oxidation on the photoluminescence spectra, which cannot be achieved by the oleum-based diazonium and Billups-Birch reduction chemistries.

With this in mind, aqueous phase diazonium chemistry (without the use of oleum) was chosen for its ability to controllably add defects to SWCNTs by varying the reactant concentration and reaction time without simultaneously reducing or oxidizing the material.<sup>60,160</sup> After functionalizing SWCNTs with freshly synthesized 4-nitrobenzene diazonium dispersed in 1 wt% SDS-D<sub>2</sub>O, the E<sub>11</sub><sup>-</sup> peak was observed (Figure 4-17A) as expected of the exciton tailoring chemistry.<sup>146</sup>

The diazonium functionalized SWCNTS were then reduced using the same conditions as with the Billups-Birch alkylation, but without the addition of new functional groups. Unlike the reduction of pristine SWCNTs (Figure 4-9), the generation of E<sub>T</sub> was apparent, verifying that the reduction of SWCNTs and subsequent trion emission is highly defect dependent under these conditions (Figure 4-17B).

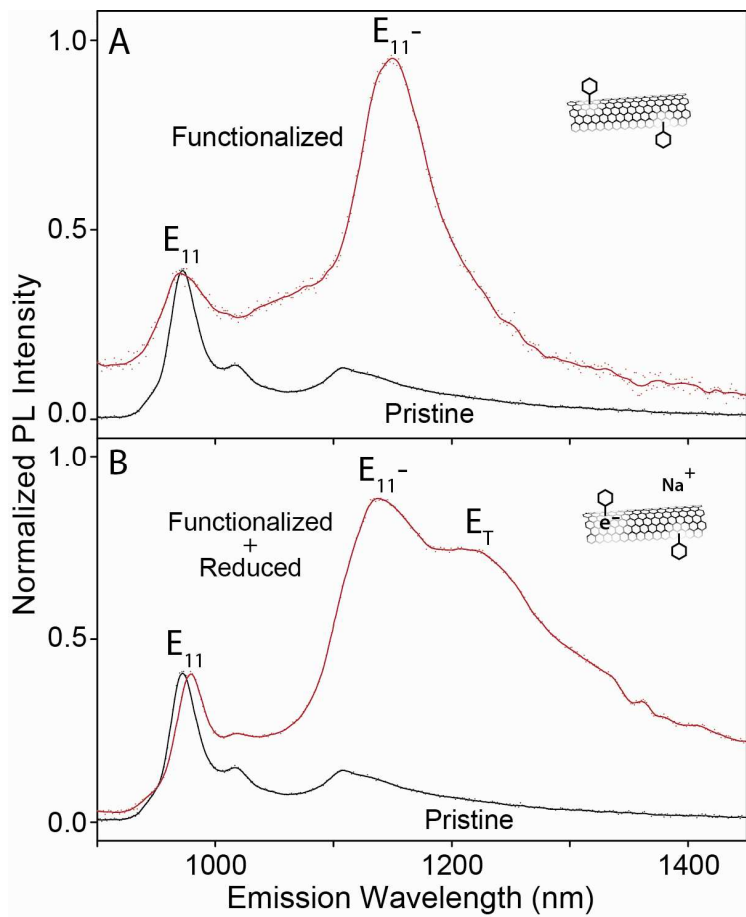


**Figure 4-17.** (A) Covalent functionalization SWCNTs by 4-nitrobenzene under neutral, aqueous conditions produces the  $E_{11}^-$  peak but not the  $E_T$  peak. (B) Subsequent charging by sodium of the functionalized SWCNTs revealed the  $E_T$  peak, suggesting a defect-dependence of trion emission under these conditions.

TFT devices were fabricated from these same neutral and reduced 4-nitrobenzene functionalized SWCNT samples to further elucidate the stabilizing effect of defects on reduced SWCNTs. Control devices were synthesized from pristine and reduced (6,5) SWCNTs, with no functionalization, for a total of four devices (pristine, reduced, functionalized, functionalized+reduced). In air, all four devices act as p-type, which is the typical behavior of SCWNTs under ambient conditions.<sup>161</sup> However, using a vacuum TT microprobe system at room temperature, the same transistors were measured at  $10^{-5}$  torr to remove the effects

of p-doping by oxygen. The pristine, reduced, and functionalized samples remained strongly p-type. However, the 4-nitrobenzene functionalized+reduced sample was weakly n-type under this minimized oxygen atmosphere, further emphasizing the importance of defects on the stability of reduced SWNTs (Figure 4-18). Interestingly, upon repeated measurement, the reduced-functionalized device went from n-type to no gate modulation, suggesting that the reduced defect site may be destroyed as it is probed, effectively oxidizing the nanotube. However, the switch from p-type to n-type for functionalized+reduced SWCNTs provides ample evidence of the trion promoting conditions of this sample, and the defect dependence of the  $E_T$ , trion emission.

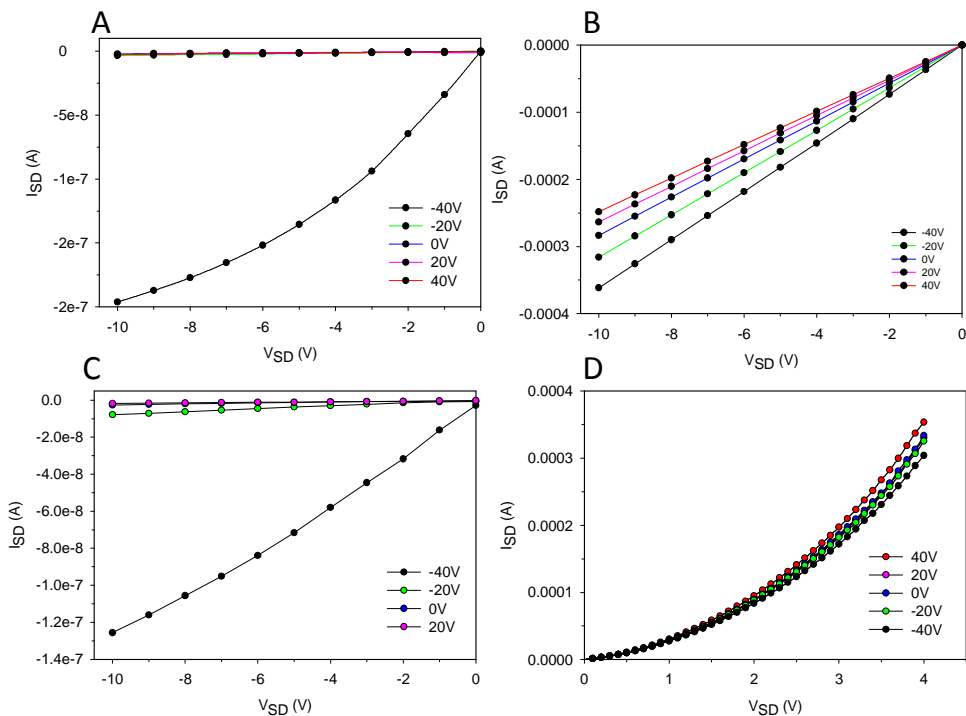


**Figure 4-18.** TFTs made from the 4-nitrobenzene functionalized and reduced samples. The (A) pristine, (B) reduced, and (C) functionalized samples show p-type behavior while measured in vacuum, but when the sample is simultaneously functionalized+reduced (D), the I-V curve switches to minor n-type behavior, indicating the importance of defects on the stability of doped electrons in the SWCNT electronic structure

## Conclusions

Excitation of covalently functionalized SWCNTs under highly reducing or oxidizing conditions produces defect activated trion photoluminescence. Reduction or oxidation alone fails to create trion emission, suggesting that significant defect enhanced stabilization of excess charge carriers is required to form the trion. The functionalized and doped SWCNT samples can be handled in air, purified in water and suspended in D<sub>2</sub>O, all without completely oxidizing the nanotubes and eliminating trion photoluminescence. Our results suggest that defects on the doped SWCNTs stabilize electrons and holes well enough to provide the excess carriers necessary to generate trions upon exciton diffusion to these doped defect sites. This picture is consistent with previous DFT computations that show localization of electrons at covalent defect sites on a SWCNT.<sup>71</sup> These results suggest a way to controllably dope SWCNTs with enhanced stability which may be of interest to semiconductor devices such as photovoltaics. Additionally, a non-doping state should not be assumed for functionalized SWCNTs, as there may be significant impact on electrochemical and device behavior.

The near-IR photoluminescence of SWCNTs is highly desirable for bioimaging applications and this new optically active states suggest a convenient method of tuning SWCNT fluorescence even further into the near-IR where photo-interference from other materials is even less likely to occur (1000-1400 nm), optical tissue penetrative depth can be maximized,<sup>19</sup> and efficient excitation by the E<sub>11</sub> transition is possible.<sup>73</sup>

## Chapter 5: Conclusions and Outlook

CNTs are on the verge of being used in many different mechanical, electronic, and optical applications.<sup>24,81,108,162</sup> However, the tendency of these materials to aggregate has been a major obstacle. Aggregation complicates device fabrication, making production more expensive and thus less likely to be of significant commercial value. It also causes the behavior of the bulk CNT material to be dominated by van der Waals forces instead of the more intriguing sp<sup>2</sup> covalent bonds that make up the individual nanotubes and are the root of most of these materials' amazing properties. Covalent functionalization had been largely dismissed as a solution to CNT dispersion problem due to the concomitant loss of electrical and optical properties. We have shown that functionalization can be achieved without these negative consequences. By controlling the location of functional groups on the nanotube surface, we are able to maintain desirable CNT behavior while improving the solubility of these materials.

Addition of organic groups to the CNT sidewalls helps to overcome the van der Waals driven aggregation of these materials that both degrades functionality and makes processing extremely difficult. Adding carbon-carbon single bonds to the nanotube surface converts the native sp<sup>2</sup> hybridized carbon atoms to sp<sup>3</sup> which disrupts the extended conjugated system of  $\pi$  orbitals that make up the delocalized bonding structure. These sp<sup>3</sup> defects generate scattering centers that limit electron and exciton diffusion, diminishing conductivity and optical activity as a result.

However, the negative effects of covalent addition can be minimized by controlling the morphology of functional groups on the nanotube surface in a manner that leaves significant tracts of the CNT  $sp^2$  hybridized carbon lattice intact to prevent excessive perturbation of diffusing electrons and excitons. This locational control is achieved by studying and understanding how the atomic and electronic structure of CNTs directs covalent chemistry on the nanotube surface. We have achieved this goal using two different chemistries, outer-wall selective functionalization of DWCNTs and defect propagative functionalization of SWCNTs that confines surface groups to discrete bands.

By utilizing the outer-walls of DWCNTs as a chemically tailorable surface on which to add functional groups, we are able to improve solubility, while retaining the pristine graphitic quality of the inner-tubes to prevent the conductivity of the entire structure from dropping to zero after the reaction. Outer-wall selectivity was demonstrated by Raman spectroscopy, which showed that the radial breathing vibrational mode of the inner-walls is retained after the reaction while the outer-wall signal is diminished. This observation reveals the retention of the inner-tube graphitic quality relative to the outer-walls after oxidation. We believe that this selectivity occurs by restriction of diffusion. The outer-walls are readily available to the oxidizing reagents, but also serve to protect the inner-tubes due to the concentric configuration as well as the high aspect ratios of the structures.

We observe this functional morphology using TEM as well, exemplified by functionalized DWCNT structures that appear rough and slightly amorphous at

the outer-walls where the addition of oxygen groups has occurred. Retention of the quality and structure of the inner-tubes is also apparent. Thin film, 2-point conductivity measurements indicate that DWCNTs oxidized using the same conditions have greater conductivity than SWCNTs due to a conductive inner-tube pathway that maintains electrical percolation of the thin film. For oxidized SWCNTs, no such conductive inner-tube pathway exists, which results in lower percolation and conductivity.

The ability of the outer-wall selectively oxidized DWNCTs to retain good electrical percolation suggested that the outer-walls must also feature an uneven distribution of oxygenated functional groups on the surface to enable electronic contact with the inner-tubes. This distribution is reflected in our TEM images as well, which suggest that oxidation occurs in a roughly clustered distribution that leaves small regions of the outer-walls intact, conductive, and thus better able to contact with the inner-tubes for improved percolation.

We explored this “banding” morphology further by studying the confined, propagative reaction mechanism of the Billups-Birch reductive alkylation chemistry on SWCNTs. Our characterization of these functionalized samples suggests a similar uneven distribution of functional groups on the SWCNT surface that leaves regions of the nanotube intact, which is important for avoiding disruption of optical properties. After covalent addition using this chemistry, we observed unusual SEM images of the functionalized SWCNT sample. These images featured alternating bright and dark regions of the nanotubes corresponding to the position of functional groups and intact graphitic nanotube

surface. Covalent addition creates insulating regions on the nanotube that charge when exposed to the electron beam of the SEM, which are manifested as brighter colored regions of the nanotube. To corroborate this evidence, the position of functional groups on the SWCNT surface were also “tagged” by nucleating Al<sub>2</sub>O<sub>3</sub> from the covalently attached carboxylic acid functionalities. The growth of Al<sub>2</sub>O<sub>3</sub> was clearly observed on the nanotube surfaces in discrete banding patterns that reflected the SEM imaging contrast.

As a result of this functional group banding pattern, retention of optical properties is also observed as shown by the continued appearance of van Hove transitions in the absorbance spectrum and near-IR photoluminescence even after covalent functionalization, counter to the previously understood optical sensitivity of functionalized CNTs.<sup>53,69,163</sup> Photoluminescence after functionalization suggests that the non-functionalized regions of the reacted SWCNT must be at least 90 nm long (the mean free path of CNT excitons) to avoid scattering and fluorescence loss.<sup>69</sup> In addition to retention of optical properties, thin films constructed from these Billups-Birch functionalized samples also remain conductive, although less so compared to their non-functionalized counterparts.<sup>147</sup>

DFT calculations suggest this banding mechanism occurs due to localization of reactive electrons around sp<sup>3</sup> defects introduced by the reductive Billups-Birch reaction into the SWCNT sp<sup>2</sup> structure. A higher electron density surrounding sp<sup>3</sup> defects primes these neighboring carbon atoms to engage in the generation of alkyl halide radicals via single-electron transfer around the defect

site, which kinetically favors the addition of these radicals around the same region of the nanotube, resulting in the observed banding structure.<sup>71,72</sup>

Retention of optical and electrical properties occurred for the Billups-Birch reaction at low functional degree featured in the aqueous extractions of the reacted SWCNT sample. However, we also observe that new photoluminescence features beyond the usual E<sub>11</sub> transition appear at higher functional degree levels (without any aqueous extraction). Calculations demonstrated to us that the addition of defects to the SWCNT surface has the effect of splitting the nanotube E<sub>11</sub> valence and conduction band energy states. Selection rules favor a transition that is lower in energy than the native energy level of the non-functionalized nanotube surface. This deviation leads to a new, redshifted photoluminescence peak that is activated by the judicious presence of defects in the CNT carbon lattice.<sup>72</sup> If there are too many defects, excitons will be scattered or unable to form due to the loss of absorption. If there are too few defects, this defect-activated photoluminescence is not observed.

However, when the addition of covalent functional groups occurs simultaneously with a highly reducing or oxidative chemistry, we observe that the splitting of the E<sub>11</sub> energy levels surrounding the defect site generates a potential well in the SWCNT electronic structure that is capable of trapping excess carriers injected into the system. Upon photogeneration of an exciton and diffusion to one of these doped defect sites, the three carriers bind due to enhanced Coulombic forces that occur in quantum confined systems. The binding forms a charged exciton, or trion, which is lower in energy than to the exciton species alone. This

trion is manifested as an additional, redshifted photoluminescence peak. Given the correct balance of functionalization, we are able to observe all three photoluminescence peaks simultaneously ( $E_{11}$ , defect activated, and trion) from a single nanotube chirality. Positive and negative trions are observed using oxidative and reducing covalent functionalization chemistries respectively. This new trion emission feature is unusually stable, lasting for several months. We believe this longevity is due to the trapping effect at defect sites, which makes it energetically difficult for excess carriers to be removed, even under aqueous conditions. This defect-dependent, trion photoluminescence in conjunction with the defect activated emission may be of interest for bio-imaging applications in which both excitation and emission are desired in the biological tissue transparent window of 1000-1400 nm.<sup>19,78</sup>

We have demonstrated several covalent functionalization strategies of dispersing CNTs to utilize the properties related to individual CNTs, but translated on a bulk scale. By controlling the location of functional groups on the nanotube surface, we are able to enjoy both the benefits of functionalization (individual dispersion related properties, improved processing) while retaining the optical and electrical properties that are normally sacrificed by uncontrolled covalent addition.

There may be opportunities for roll-to-roll printing processes using these CNT dispersions, particularly as thin film current collectors. Low conductivities can be rectified after deposition by high-temperature annealing to remove functional groups at a stage in which dispersion is already set after drying or

filtration steps.<sup>162</sup> Alternatively, this step may be unnecessary if DWCNTs or MWCNTs are used according to the proposed inner-tube conductive pathway hypothesis<sup>80</sup>.

A collaboration in CNT bio-imaging is advised to observe whether the defect activated trion photoluminescence would be observable in biological tissue. Time resolved photoluminescence studies should also be done on these doped, functionalized samples to identify the luminescence lifetimes of both the excitons and trions in the system to unequivocally identify these species.<sup>164</sup>

We hope these studies on covalently functionalized CNTs will bring them a step closer to the electronic, optical and mechanical applications originally envisioned for this unique material. The importance of this work remains to be seen, but I believe these results will help the graphitic materials field to understand that the functional impact of defects is controlled not by just the absolute concentration but also the density. From this perspective, it becomes possible to avoid the negative effects of defects by controlling the defect density, but also to use these defects to engineer new material properties through spatial control.

## Appendix 1

**Table 3-2.** Net atomic charges on a (10,0)-(CH<sub>2</sub>)<sub>5</sub>COOH SWCNT.

63	Site of defect (sp <sup>3</sup> C)
	C surrounding sp <sup>3</sup> C
1	neutral
1	0.000
2	-0.006
2	0.002
3	-0.012
3	0.001
4	-0.005
4	0.000
5	-0.011
5	0.000
6	-0.012
6	0.001
7	-0.010
7	0.000
8	-0.007
8	0.000
9	-0.005
9	0.000
10	-0.011
10	0.001
11	-0.006
11	0.000
12	-0.015
12	0.000
13	-0.012
13	0.000
14	-0.012
14	0.001
15	-0.013
15	-0.001
16	-0.019
16	0.000
17	-0.011
17	-0.001
18	-0.015
18	0.000
19	-0.014
19	0.000
20	-0.018
20	-0.001
21	-0.015
21	-0.001
22	-0.018
22	0.000
23	-0.011
23	0.000
24	-0.011
24	0.000
25	-0.010
25	-0.001
26	-0.018
26	0.001
27	-0.010
27	0.000
28	-0.009
28	0.000
29	-0.007
29	0.000
30	-0.010
30	0.001
31	-0.006
31	0.001
32	-0.012
32	-0.001
33	-0.011
33	0.001
34	-0.006
34	0.000
35	-0.013
35	-0.001
36	-0.015
36	0.000
37	-0.012
37	-0.002
38	-0.014
38	-0.001
39	-0.014
39	-0.004

40	-0.014	-0.016	-0.020
41	0.007	0.003	-0.003
42	0.000	-0.008	-0.017
43	0.000	-0.006	-0.014
44	-0.002	-0.010	-0.018
45	-0.003	-0.006	-0.009
46	0.001	-0.010	-0.014
47	0.000	-0.003	-0.009
48	0.000	-0.008	-0.013
49	0.000	-0.004	-0.010
50	-0.001	-0.008	-0.017
51	0.000	-0.006	-0.015
52	0.000	-0.012	-0.018
53	0.000	-0.005	-0.013
54	-0.001	-0.006	-0.014
55	0.001	-0.002	-0.005
56	0.000	-0.005	-0.009
57	0.000	-0.003	-0.009
58	0.001	-0.012	-0.018
59	-0.001	-0.006	-0.011
60	-0.002	-0.012	-0.022
61	0.002	-0.003	-0.009
62	-0.037	-0.061	-0.069
63	0.120	0.127	0.127
64	0.004	0.001	-0.004
65	-0.039	-0.061	-0.068
66	-0.004	-0.007	-0.015
67	-0.007	-0.031	-0.038
68	-0.003	-0.005	-0.012
69	0.000	-0.003	-0.009
70	0.002	-0.002	-0.005
71	0.000	-0.006	-0.009
72	0.000	-0.002	-0.006
73	0.001	-0.007	-0.011
74	0.000	-0.003	-0.009
75	0.000	-0.003	-0.010
76	0.000	-0.004	-0.010
77	0.000	-0.007	-0.012
78	0.000	-0.005	-0.011
79	0.001	-0.011	-0.016

80	-0.001	-0.006	-0.015
81	-0.001	-0.007	-0.016
82	0.000	-0.006	-0.015
83	0.001	-0.007	-0.016
84	-0.001	-0.005	-0.011
85	0.000	-0.010	-0.016
86	0.000	-0.006	-0.013
87	0.000	-0.007	-0.014
88	-0.001	-0.005	-0.012
89	0.000	-0.006	-0.013
90	0.000	-0.002	-0.006
91	0.001	-0.008	-0.011
92	0.000	-0.003	-0.006
93	0.000	-0.005	-0.008
94	0.000	-0.003	-0.009
95	0.000	-0.003	-0.010
96	0.000	-0.004	-0.009
97	0.001	-0.009	-0.015
98	0.002	-0.004	-0.009
99	0.001	-0.008	-0.012
100	-0.001	-0.005	-0.012
101	0.000	-0.005	-0.013
102	0.000	-0.015	-0.023
103	-0.001	-0.003	-0.008
104	0.000	-0.004	-0.010
105	-0.002	-0.013	-0.021
106	0.000	-0.005	-0.014
107	-0.002	-0.016	-0.022
108	-0.001	-0.005	-0.012
109	-0.001	-0.006	-0.012
110	0.001	-0.002	-0.005
111	0.001	-0.006	-0.009
112	0.000	-0.002	-0.007
113	0.000	-0.007	-0.010
114	0.000	-0.003	-0.009
115	0.000	-0.003	-0.009
116	0.000	-0.005	-0.010
117	0.000	-0.007	-0.012
118	0.000	-0.005	-0.011
119	0.001	-0.009	-0.015

120	-0.001	-0.007	-0.016
121	-0.001	-0.008	-0.016
122	0.000	-0.006	-0.015
123	0.001	-0.007	-0.015
124	-0.001	-0.006	-0.012
125	0.000	-0.010	-0.016
126	-0.001	-0.006	-0.013
127	0.000	-0.007	-0.014
128	-0.001	-0.005	-0.012
129	0.000	-0.006	-0.013
130	0.001	-0.002	-0.005
131	0.001	-0.007	-0.010
132	0.000	-0.003	-0.006
133	0.000	-0.005	-0.008
134	0.000	-0.003	-0.010
135	0.000	-0.003	-0.009
136	0.000	-0.004	-0.010
137	0.000	-0.008	-0.014
138	0.001	-0.005	-0.010
139	0.000	-0.008	-0.014
140	-0.002	-0.007	-0.015
141	0.000	-0.008	-0.015
142	-0.001	-0.005	-0.010
143	0.002	-0.008	-0.017
144	0.001	-0.004	-0.008
145	0.000	-0.004	-0.011
146	0.000	-0.003	-0.009
147	0.000	-0.002	-0.007
148	0.001	-0.009	-0.015
149	0.000	-0.005	-0.010
150	0.001	-0.007	-0.016
151	-0.001	-0.007	-0.016
152	0.000	-0.007	-0.014
153	-0.001	-0.006	-0.012
154	0.001	-0.006	-0.009
155	0.000	-0.005	-0.012
156	0.000	-0.003	-0.010
157	0.000	-0.003	-0.006
158	0.001	-0.007	-0.012
159	0.000	-0.004	-0.010

160	0.000	-0.006	-0.014
161	0.108	0.105	0.102
164	0.123	0.122	0.122
165	0.136	0.136	0.135
168	0.129	0.129	0.129
171	0.117	0.116	0.114
174	-0.070	-0.070	-0.073
O			
177	-0.117	-0.121	-0.122
178	-0.055	-0.056	-0.058
H			
162	-0.061	-0.066	-0.070
163	-0.061	-0.070	-0.075
166	-0.073	-0.076	-0.076
167	-0.061	-0.063	-0.064
169	-0.065	-0.069	-0.074
170	-0.065	-0.069	-0.072
172	-0.056	-0.055	-0.054
173	-0.055	-0.057	-0.059
175	-0.038	-0.040	-0.042
176	-0.038	-0.040	-0.042
179	0.180	0.180	0.181

**Table 3-3.** Net Atomic Charges on a (5,5)-(CH<sub>2</sub>)<sub>5</sub>COOH

59	Site of the defect (sp <sup>3</sup> C)
58	C directly attached to the sp <sup>3</sup> (ortho)
57	Meta
56	Para

C	neutral	-1 charge	-2 charge
1	0.001	-0.008	-0.024
2	-0.001	-0.011	-0.019
3	0.001	-0.008	-0.021
4	0.000	-0.009	-0.019
5	0.000	-0.008	-0.018
6	0.000	-0.009	-0.021
7	0.000	-0.010	-0.020
8	0.001	-0.008	-0.018
9	0.000	-0.009	-0.017
10	0.000	-0.007	-0.020
11	0.000	-0.010	-0.020
12	0.001	-0.008	-0.021
13	0.000	-0.009	-0.019
14	0.000	-0.007	-0.020
15	-0.001	-0.011	-0.019
16	0.001	-0.008	-0.024
17	0.000	-0.009	-0.022
18	0.000	-0.008	-0.018
19	0.000	-0.005	-0.015
20	-0.001	-0.006	-0.016
21	0.001	-0.006	-0.013
22	0.000	-0.008	-0.017
23	-0.001	-0.005	-0.013
24	0.001	-0.005	-0.015
25	-0.001	-0.008	-0.014
26	0.001	-0.004	-0.017
27	0.000	-0.007	-0.019
28	0.000	-0.010	-0.017
29	0.001	-0.009	-0.019
30	-0.001	-0.008	-0.014
31	0.000	-0.009	-0.015
32	-0.001	-0.013	-0.022
33	0.002	-0.009	-0.016
34	0.001	-0.008	-0.020
35	-0.003	-0.010	-0.016
36	-0.002	-0.010	-0.017
37	0.001	-0.013	-0.020
38	-0.001	-0.012	-0.019
39	-0.004	-0.007	-0.014

40	-0.002	-0.033	-0.039
41	0.002	-0.001	-0.007
42	-0.002	-0.013	-0.019
43	-0.002	-0.021	-0.026
44	0.001	-0.002	-0.012
45	0.000	-0.029	-0.035
46	0.001	-0.004	-0.008
47	0.000	-0.005	-0.013
48	-0.001	-0.015	-0.021
49	0.000	-0.007	-0.018
50	0.000	-0.012	-0.018
51	-0.001	-0.013	-0.019
52	0.000	-0.008	-0.018
53	-0.001	-0.008	-0.022
54	-0.001	-0.014	-0.020
55	0.001	-0.007	-0.014
56	-0.002	-0.010	-0.014
57	-0.001	0.000	-0.007
58	-0.035	-0.072	-0.078
59	0.115	0.132	0.131
60	-0.024	-0.051	-0.057
61	0.007	-0.001	-0.005
62	0.002	-0.018	-0.028
63	-0.004	-0.011	-0.016
64	0.000	-0.012	-0.026
65	-0.001	-0.007	-0.015
66	0.000	-0.008	-0.016
67	-0.001	-0.005	-0.010
68	0.000	-0.006	-0.019
69	-0.001	-0.008	-0.022
70	-0.001	-0.015	-0.021
71	0.000	-0.005	-0.013
72	-0.002	-0.010	-0.014
73	-0.001	0.000	-0.006
74	-0.002	-0.033	-0.039
75	-0.004	-0.008	-0.013
76	-0.023	-0.050	-0.056
77	0.006	-0.002	-0.007
78	-0.001	-0.012	-0.022
79	0.000	-0.009	-0.015

80	0.000	-0.012	-0.026
81	-0.001	-0.007	-0.015
82	0.001	-0.005	-0.015
83	-0.001	-0.005	-0.013
84	0.000	-0.006	-0.019
85	0.000	-0.007	-0.018
86	0.000	-0.012	-0.018
87	0.001	-0.002	-0.012
88	-0.002	-0.021	-0.026
89	0.002	-0.002	-0.007
90	-0.002	-0.013	-0.018
91	-0.002	-0.010	-0.017
92	-0.003	-0.010	-0.017
93	0.001	-0.009	-0.016
94	0.001	-0.008	-0.020
95	0.000	-0.010	-0.017
96	0.000	-0.007	-0.019
97	-0.001	-0.008	-0.014
98	0.001	-0.004	-0.017
99	-0.001	-0.006	-0.016
100	0.000	-0.005	-0.015
101	0.117	0.108	0.108
104	0.109	0.111	0.110
105	0.142	0.141	0.140
108	0.124	0.124	0.124
111	0.121	0.119	0.119
114	-0.071	-0.072	-0.094
O			
117	-0.118	-0.125	-0.152
118	-0.055	-0.057	-0.094
H			
102	-0.059	-0.071	-0.075
103	-0.060	-0.071	-0.075
106	-0.068	-0.072	-0.074
107	-0.066	-0.070	-0.072
109	-0.065	-0.070	-0.076
110	-0.065	-0.070	-0.074
112	-0.054	-0.056	-0.059
113	-0.056	-0.058	-0.062
115	-0.038	-0.041	-0.054

## Bibliography

1. Edwards, B. C. Design and Deployment of a Space Elevator. *Acta Astronaut.* **2000**, *47*, 735–744.
2. Graham, A. P.; Duesberg, G. S.; Seidel, R. V; Liebau, M.; Unger, E.; Pamler, W.; Kreupl, F.; Hoenlein, W. Carbon Nanotubes for Microelectronics? *Small* **2005**, *1*, 382–390.
3. Saito, R.; Dresselhaus, G.; Dresselhaus, M. S. *Physical Properties of Carbon Nanotubes*; Imperial College Press: London, 1998; pp. 1–38.
4. Iijima, S. Helical Microtubules of Graphitic Carbon. *Nature* **1991**, *354*, 56–58.
5. Iijima, S.; Ajayan, P. M.; Ichihashi, T. Growth Model for Carbon Nanotubes. *Phys. Rev. Lett.* **1992**, *69*, 3100–3103.
6. Ajayan, P. M.; Ebbesen, T. W.; Ichihashi, T.; Iijima, S.; Tanigaki, K.; Hiura, H. Opening Carbon Nanotubes with Oxygen and Implications for Filling. *Nature* **1993**, *362*, 522–525.
7. Monthioux, M.; Kuznetsov, V. L. Who Should Be Given the Credit for the Discovery of Carbon Nanotubes? *Carbon* **2006**, *44*, 1621–1623.
8. Avouris, P.; Chen, Z.; Perebeinos, V. Carbon-based Electronics. *Nat. Nanotechnol.* **2007**, *2*, 605–615.
9. Webb, J. F.; Ahmadi, M. T. *Advanced Nanoelectronics*; Ismail, R.; Ahmadi, M. T.; Anwar, S., Eds.; 1st ed.; CRC Press, 2012; pp. 55–56.
10. Sgobba, V.; Guldi, D. M. Carbon Nanotubes—electronic/electrochemical Properties and Application for Nanoelectronics and Photonics. *Chem. Soc. Rev.* **2009**, *38*, 165–184.
11. Dürkop, T.; Getty, S. a.; Cobas, E.; Fuhrer, M. S. Extraordinary Mobility in Semiconducting Carbon Nanotubes. *Nano Lett.* **2004**, *4*, 35–39.
12. Poncharal, P.; Berger, C.; Yi, Y.; Wang, Z. L.; Heer, W. A. De Room Temperature Ballistic Conduction in Carbon Nanotubes. *J. Phys. Chem. B* **2002**, *106*, 12104–12118.
13. Treacy, M. M. J.; Ebbesen, T. W.; Gibson, J. M. Exceptionally High Young's Modulus Observed for Individual Carbon Nanotubes. *Nature* **1996**, *381*, 678–680.

14. Fujii, M.; Zhang, X.; Xie, H.; Ago, H.; Takahashi, K.; Ikuta, T.; Abe, H.; Shimizu, T. Measuring the Thermal Conductivity of a Single Carbon Nanotube. *Phys. Rev. Lett.* **2005**, *95*, 065502.
15. Wang, F.; Dukovic, G.; Brus, L. E.; Heinz, T. F. The Optical Resonances in Carbon Nanotubes Arise from Excitons. *Science* **2005**, *308*, 838–841.
16. O'Connell, M. J.; Bachilo, S. M.; Huffman, C. B.; Moore, V. C.; Strano, M. S.; Haroz, E. H.; Rialon, K. L.; Boul, P. J.; Noon, W. H.; Kittrell, C. *et al.* Band Gap Fluorescence from Individual Single-walled Carbon Nanotubes. *Science* **2002**, *297*, 593–596.
17. Bachilo, S. M.; Strano, M. S.; Kittrell, C.; Hauge, R. H.; Smalley, R. E.; Weisman, R. B. Structure-assigned Optical Spectra of Single-walled Carbon Nanotubes. *Science* **2002**, *298*, 2361–2366.
18. Welsher, K.; Liu, Z.; Sherlock, S. P.; Robinson, J. T.; Chen, Z.; Daranciang, D.; Dai, H. A Route to Brightly Fluorescent Carbon Nanotubes for Near-infrared Imaging in Mice. *Nat. Nanotechnol.* **2009**, *4*, 773–780.
19. Welsher, K.; Sherlock, S. P.; Dai, H. Deep-tissue Anatomical Imaging of Mice Using Carbon Nanotube Fluorophores in the Second Near-infrared Window. *Proc. Natl. Acad. Sci. U. S. A.* **2011**, *108*, 8943–3948.
20. Hong, S.; Myung, S. Nanotube Electronics: a Flexible Approach to Mobility. *Nat. Nanotechnol.* **2007**, *2*, 207–208.
21. Chang, C.; Hsu, I.; Aykol, M.; Hung, W.; Chen, C.; Cronin, S. B. A New Lower Limit for the Ultimate Breaking Strain of Carbon Nanotubes. *ACS Nano* **2010**, *4*, 5095–5100.
22. Ajayan, P. M.; Tour, J. M. Nanotube Composites. *Nature* **2007**, *447*, 1066–1068.
23. Sandler, J.; Shaffer, M. S. .; Prasse, T.; Bauhofer, W.; Schulte, K.; Windle, A. H. Development of a Dispersion Process for Carbon Nanotubes in an Epoxy Matrix and the Resulting Electrical Properties. *Polymer* **1999**, *40*, 5967–5971.
24. Liu, Z.; Tabakman, S.; Welsher, K.; Dai, H. Carbon Nanotubes in Biology and Medicine: In Vitro and in Vivo Detection, Imaging and Drug Delivery. *Nano Res.* **2009**, *2*, 85–120.

25. Kongkanand, A.; Domínguez, R. M.; Kamat, P. V Single Wall Carbon Nanotube Scaffolds for Photoelectrochemical Solar Cells. Capture and Transport of Photogenerated Electrons. *Nano Lett.* **2007**, *7*, 676–680.
26. Wu, Z.; Chen, Z.; Du, X.; Logan, J. M.; Sippel, J.; Nikolou, M.; Kamaras, K.; Reynolds, J. R.; Tanner, D. B.; Hebard, A. F. *et al.* Transparent, Conductive Carbon Nanotube Films. *Science* **2004**, *305*, 1273–1276.
27. Sun, C.; Karki, K.; Jia, Z.; Liao, H.; Zhang, Y.; Li, T.; Qi, Y.; Cumings, J.; Rubloff, G. W.; Wang, Y. A Beaded-String Silicon Anode. *ACS Nano* **2013**, *7*, 2717–2724.
28. Ericson, L. M.; Fan, H.; Peng, H.; Davis, V. A.; Zhou, W.; Sulpizio, J.; Wang, Y.; Booker, R.; Vavro, J.; Guthy, C. *et al.* Macroscopic, Neat, Single-walled Carbon Nanotube Fibers. *Science* **2004**, *305*, 1447–1450.
29. Wong, E. W.; Sheehan, P. E.; Lieber, C. M. Nanobeam Mechanics: Elasticity, Strength, and Toughness of Nanorods and Nanotubes. *Science* **1997**, *277*, 1971–1975.
30. Coleman, J. N.; Khan, U.; Blau, W. J.; Gun’ko, Y. K. Small but Strong: A Review of the Mechanical Properties of Carbon Nanotube–polymer Composites. *Carbon* **2006**, *44*, 1624–1652.
31. Wang, F.; Dukovic, G.; Brus, L.; Heinz, T. Time-Resolved Fluorescence of Carbon Nanotubes and Its Implication for Radiative Lifetimes. *Phys. Rev. Lett.* **2004**, *92*, 177401.
32. Avouris, P.; Appenzeller, J.; Martel, R.; Wind, S. J. Carbon Nanotube Electronics. *Proc. IEEE* **2003**, *91*, 1772–1784.
33. Tans, S. J.; Devoret, M. H.; Dai, H. J.; Thess, A.; Smalley, R. E.; Geerligs, L. J.; Dekker, C. Individual Single-wall Carbon Nanotubes as Quantum Wires. *Nature* **1997**, *386*, 474–477.
34. Nikolaev, P.; Bronikowski, M. J.; Bradley, R. K.; Rohmund, F.; Colbert, D. T.; Smith, K. A.; Smalley, R. E. Gas-phase Catalytic Growth of Single-walled Carbon Nanotubes from Carbon Monoxide. *Chem. Phys. Lett.* **1999**, *313*, 91–97.
35. Endo, M.; Muramatsu, H.; Hayashi, T.; Kim, Y. A.; Terrones, M.; Dresselhaus, M. S. “Buckypaper” from Coaxial Nanotubes. *Nature* **2005**, *433*, 476.

36. Zheng, M.; Jagota, A.; Semke, E. D.; Diner, B. A.; Mclean, R. S.; Lustig, S. R.; Richardson, R. E.; Tassi, N. G. DNA-assisted Dispersion and Separation of Carbon Nanotubes. *Nat. Mater.* **2003**, *2*, 338 – 342.
37. Tu, X.; Manohar, S.; Jagota, A.; Zheng, M. DNA Sequence Motifs for Structure-specific Recognition and Separation of Carbon Nanotubes. *Nature* **2009**, *460*, 250–253.
38. Zheng, M.; Jagota, A.; Strano, M. S.; Santos, A. P.; Barone, P.; Chou, S. G.; Diner, B. A.; Dresselhaus, M. S.; Mclean, R. S.; Onoa, G. B. *et al.* Structure-Based Carbon Nanotube Sorting by Sequence-Dependent DNA Assembly. *Science* **2003**, *302*, 1545–1548.
39. Huang, X.; Mclean, R. S.; Zheng, M. High-Resolution Length Sorting and Purification of DNA-Wrapped Carbon Nanotubes by Size-Exclusion Chromatography. *Anal. Chem.* **2005**, *77*, 6225–6228.
40. Tanaka, T.; Jin, H.; Miyata, Y.; Fujii, S.; Suga, H.; Naitoh, Y.; Minari, T.; Miyadera, T.; Tsukagoshi, K.; Kataura, H. Simple and Scalable Gel-Based Separation of Metallic and Semiconducting Carbon Nanotubes. *Nano Lett.* **2009**, *9*, 1497–1500.
41. Liu, H.; Nishide, D.; Tanaka, T.; Kataura, H. Large-scale Single-chirality Separation of Single-wall Carbon Nanotubes by Simple Gel Chromatography. *Nat. Commun.* **2011**, *2*.
42. Arnold, M. S.; Green, A. A.; Hulvat, J. F.; Stupp, S. I.; Hersam, M. C. Sorting Carbon Nanotubes by Electronic Structure Using Density Differentiation. *Nat. Nanotechnol.* **2006**, *1*, 60–65.
43. Green, A. A.; Hersam, M. C. Nearly Single-Chirality Single-Walled Carbon Nanotubes Produced via Orthogonal Iterative Density Gradient Ultracentrifugation. *Adv. Mater.* **2011**, *23*, 2185–2190.
44. Arnold, M. S.; Stupp, S. I.; Hersam, M. C. Enrichment of Single-Walled Carbon Nanotubes by Diameter in Density Gradients. *Nano Lett.* **2005**, *5*, 713–718.
45. Kitiyanan, B.; Alvarez, W. E.; Harwell, J. H.; Resasco, D. E. Controlled Production of Single-wall Carbon Nanotubes by Catalytic Decomposition of CO on Bimetallic Co – Mo Catalysts. *Chem. Phys. Lett.* **2000**, *317*, 497–503.
46. Bachilo, S. M.; Balzano, L.; Herrera, J. E.; Pompeo, F.; Resasco, D. E.; Weisman, R. B. Narrow (n,m)-distribution of Single-walled Carbon

- Nanotubes Grown Using a Solid Supported Catalyst. *J. Am. Chem. Soc.* **2003**, *125*, 11186–11187.
- 47. O'Connell, M. J.; Boul, P.; Ericson, L. M.; Huffman, C.; Wang, Y.; Haroz, E.; Kuper, C.; Tour, J.; Ausman, K. D.; Smalley, R. E. Reversible Water-solubilization of Single-walled Carbon Nanotubes by Polymer Wrapping. *Chem. Phys. Lett.* **2001**, *342*, 265–271.
  - 48. Zhou, G.; Duan, W.; Gu, B. First-principles Study on Morphology and Mechanical Properties of Single-walled Carbon Nanotube. *Chem. Phys. Lett.* **2001**, *333*, 344–349.
  - 49. Tan, P.; Rozhin, a.; Hasan, T.; Hu, P.; Scardaci, V.; Milne, W.; Ferrari, a. Photoluminescence Spectroscopy of Carbon Nanotube Bundles: Evidence for Exciton Energy Transfer. *Phys. Rev. Lett.* **2007**, *99*, 1–4.
  - 50. Hertel, T.; Fasel, R.; Moos, G. Charge-carrier Dynamics in Single-wall Carbon Nanotube Bundles: a Time-domain Study. *Appl. Phys. A* **2002**, *75*, 449–465.
  - 51. Zhang, Q.; Rastogi, S.; Chen, D.; Lippits, D.; Lemstra, P. J. Low Percolation Threshold in Single-walled Carbon Nanotube/high Density Polyethylene Composites Prepared by Melt Processing Technique. *Carbon* **2006**, *44*, 778–785.
  - 52. Ausman, K. D.; Piner, R.; Lourie, O.; Ruoff, R. S.; Korobov, M. Organic Solvent Dispersions of Single-Walled Carbon Nanotubes□: Toward Solutions of Pristine Nanotubes. *J. Phys. Chem. B* **2000**, *104*, 8911–8915.
  - 53. Bahr, J. L.; Mickelson, E. T.; Bronikowski, M. J.; Smalley, R. E.; Tour, J. M. Dissolution of Small Diameter Single-wall Carbon Nanotubes in Organic Solvents? *Chem. Commun.* **2001**, *0*, 193–194.
  - 54. Moore, V. C.; Strano, M. S.; Haroz, E. H.; Hauge, R. H.; Smalley, R. E.; Schmidt, J.; Talmon, Y. Individually Suspended Single-Walled Carbon Nanotubes in Various Surfactants. *Nano Lett.* **2003**, *3*, 1379–1382.
  - 55. Mason, T. J.; Lorimer, J. P. *Sonochemistry: Theory, Applications, and Uses of Ultrasound in Chemistry*; Halsted: New York, NY, 1988.
  - 56. Leeds, J. D.; Fourkas, J. T.; Wang, Y. Achieving Ultrahigh Concentrations of Fluorescent Single-Walled Carbon Nanotubes Using Small-Molecule Viscosity Modifiers. *Small* **2013**, *9*, 241–247.

57. Yurekli, K.; Mitchell, C. a; Krishnamoorti, R. Small-angle Neutron Scattering from Surfactant-assisted Aqueous Dispersions of Carbon Nanotubes. *J. Am. Chem. Soc.* **2004**, *126*, 9902–9903.
58. Green, A. A.; Hersam, M. C. Processing and Properties of Highly Enriched Double-wall Carbon Nanotubes. *Nat. Nanotechnol.* **2009**, *4*, 64 – 70.
59. Zhao, Y. L.; Stoddart, J. F. Noncovalent Functionalization of Single-Walled Carbon Nanotubes. *Acc. Chem. Res.* **2009**, *42*, 1161–1171.
60. Strano, M. S.; Dyke, C. a; Usrey, M. L.; Barone, P. W.; Allen, M. J.; Shan, H.; Kittrell, C.; Hauge, R. H.; Tour, J. M.; Smalley, R. E. Electronic Structure Control of Single-walled Carbon Nanotube Functionalization. *Science* **2003**, *301*, 1519–1522.
61. Hu, H.; Bhowmik, P.; Zhao, B.; Hamon, M. A.; Itkis, M. E.; Haddon, R. C. Determination of the Acidic Sites of Purified Single-walled Carbon Nanotubes by Acid - Base Titration. *Chemical Physics* **2001**, *345*, 25–28.
62. Fan, Y.; Goldsmith, B. R.; Collins, P. G. Identifying and Counting Point Defects in Carbon Nanotubes. *Nat. Mater.* **2005**, *4*, 906–11.
63. Karousis, N.; Tagmatarchis, N.; Tasis, D. Current Progress on the Chemical Modification of Carbon Nanotubes. *Chem. Rev.* **2010**, *110*, 5366–5397.
64. Tasis, D.; Tagmatarchis, N.; Bianco, A.; Prato, M. Chemistry of Carbon Nanotubes. *Chem. Rev.* **2006**, *106*, 1105–1136.
65. Park, H.; Zhao, J.; Lu, J. P. Effects of Sidewall Functionalization on Conducting Properties of Single Wall Carbon Nanotubes. *Nano Lett.* **2006**, *6*, 916–919.
66. Collins, P. G.; Bradley, K.; Ashigami, M.; Zettl, A. Extreme Oxygen Sensitivity of Electronic Properties of Carbon Nanotubes. *Science* **2000**, *287*, 1801–1804.
67. Ashraf, M.; Bruque, N.; Pandey, R.; Collins, P.; Lake, R. Effect of Localized Oxygen Functionalization on the Conductance of Metallic Carbon Nanotubes. *Phys. Rev. B* **2009**, *79*, 115428.
68. Peng, H.; Alemany, L. B.; Margrave, J. L.; Khabashesku, V. N. Sidewall Carboxylic Acid Functionalization of Single-walled Carbon Nanotubes. *J. Am. Chem. Soc.* **2003**, *125*, 15174–15182.

69. Cognet, L.; Tsyboulski, D. a; Rocha, J.-D. R.; Doyle, C. D.; Tour, J. M.; Weisman, R. B. Stepwise Quenching of Exciton Fluorescence in Carbon Nanotubes by Single-molecule Reactions. *Science* **2007**, *316*, 1465–1468.
70. Goldsmith, B. R.; Coroneus, J. G.; Khalap, V. R.; Kane, A. a; Weiss, G. a; Collins, P. G. Conductance-controlled Point Functionalization of Single-walled Carbon Nanotubes. *Science* **2007**, *315*, 77–81.
71. Deng, S.; Zhang, Y.; Brozena, A. H.; Mayes, M. L.; Banerjee, P.; Chiou, W. A.; Rubloff, G. W.; Schatz, G. C.; Wang, Y. Confined Propagation of Covalent Chemical Reactions on Single-walled Carbon Nanotubes. *Nat. Commun.* **2011**, *2*.
72. Zhang, Y.; Valley, N.; Brozena, A. H.; Paio, Y.; Song, X.; Schatz, G. C.; Wang, Y. Propagative Sidewall Alkylcarboxylation That Induces Red-Shifted Near-IR Photoluminescence in Single-Walled Carbon Nanotubes. *J. Phys. Chem. Lett.* **2013**, *4*, 826–830.
73. Ghosh, S.; Bachilo, S. M.; Simonette, R. A.; Beckingham, K. M.; Weisman, R. B. Oxygen Doping Modifies Near-Infrared Band Gaps in Fluorescent Single-Walled Carbon Nanotubes. *Science* **2011**, *330*, 1656–1659.
74. Lampert, M. Mobile and Immobile Effective-Mass-Particle Complexes in Nonmetallic Solids. *Phys. Rev. Lett.* **1958**, *1*, 450–453.
75. Kheng, K.; Cox, R.; d' Aubigné, M.; Bassani, F.; Saminadayar, K.; Tatarenko, S. Observation of Negatively Charged Excitons X- in Semiconductor Quantum Wells. *Phys. Rev. Lett.* **1993**, *71*, 1752–1755.
76. Cox, R. T.; Huard, V.; Kheng, K.; Lovisa, S.; Miller, R. B.; Saminadayar, K.; Arnoult, A.; Cibert, J.; Tatarenko, S.; Potemski, M. Exciton Trions in II-VI Heterostructures. *Acta Phys. Pol. A* **1998**, *94*, 99–109.
77. Klingshirn, C. *Semiconductor Optics*; 2nd ed.; Springer, 2005; pp. 254–259.
78. Chance, B. Near-Infrared Images Using Continuous, Phase-Modulated, and Pulsed Light with Quantitation of Blood and Blood Oxygenation. *Ann. N. Y. Acad. Sci.* **1998**, *838*, 29–45.
79. Dumortier, H.; Lacotte, S.; Pastorin, G.; Marega, R.; Wu, W.; Bonifazi, D.; Briand, J.-P.; Prato, M.; Muller, S.; Bianco, A. Functionalized Carbon Nanotubes Are Non-cytotoxic and Preserve the Functionality of Primary Immune Cells. *Nano Lett.* **2006**, *6*, 1522–1528.

80. Brozena, A. H.; Moskowitz, J.; Shao, B.; Deng, S.; Liao, H.; Gaskell, K. J.; Wang, Y. Outer Wall Selectively Oxidized, Water-soluble Double-walled Carbon Nanotubes. *J. Am. Chem. Soc.* **2010**, *132*, 3932–3938.
81. Baughman, R. H.; Zakhidov, A. A.; Heer, W. A. de Carbon Nanotubes--the Route Toward Applications. *Science* **2002**, *297*, 787–792.
82. Vigolo, B.; Coulon, C.; Maugey, M.; Zakri, C.; Poulin, P. An Experimental Approach to the Percolation of Sticky Nanotubes. *Science* **2005**, *309*, 920–923.
83. Rahman, G. M. A.; Guldi, D. M.; Cagnoli, R.; Mucci, A.; Schenetti, L.; Vaccari, L.; Prato, M. Combining Single Wall Carbon Nanotubes and Photoactive Polymers for Photoconversion. *J. Am. Chem. Soc.* **2005**, *127*, 10051–10057.
84. Sun, C.-H.; Yin, L.-C.; Li, F.; Lu, G.-Q.; Cheng, H.-M. Van Der Waals Interactions Between Two Parallel Infinitely Long Single-walled Nanotubes. *Chem. Phys. Lett.* **2005**, *403*, 343–346.
85. Peng, X.; Wong, S. S. Functional Covalent Chemistry of Carbon Nanotube Surfaces. *Adv. Mater.* **2009**, *21*, 625–642.
86. Liu, K.; Wang, W.; Xu, Z.; Bai, X.; Wang, E.; Yao, Y.; Zhang, J.; Liu, Z. Chirality-dependent Transport Properties of Double-walled Nanotubes Measured in Situ on Their Field-effect Transistors. *J. Am. Chem. Soc.* **2009**, *131*, 62–63.
87. Kim, Y. a.; Muramatsu, H.; Hayashi, T.; Endo, M.; Terrones, M.; Dresselhaus, M. S. Thermal Stability and Structural Changes of Double-walled Carbon Nanotubes by Heat Treatment. *Chem. Phys. Lett.* **2004**, *398*, 87–92.
88. Peng, B.; Locascio, M.; Zapol, P.; Li, S.; Mielke, S. L.; Schatz, G. C.; Espinosa, H. D. Measurements of Near-ultimate Strength for Multiwalled Carbon Nanotubes and Irradiation-induced Crosslinking Improvements. *Nat. Nanotechnol.* **2008**, *3*, 626–631.
89. Liu, J.; Rinzler, A. G.; Dai, H.; Hafner, J. H.; Bradley, R. K.; Boul, P. J.; Lu, A.; Iverson, T.; Shelimov, K.; Huffman, C. B. *et al.* Fullerene Pipes. *Science* **1998**, *280*, 1253–1256.
90. Chen, Z.; Kobashi, K.; Rauwald, U.; Booker, R.; Fan, H.; Hwang, W.-F.; Tour, J. M. Soluble Ultra-short Single-walled Carbon Nanotubes. *J. Am. Chem. Soc.* **2006**, *128*, 10568–10571.

91. Davis, V. A.; Ericson, L. M.; Parra-Vasquez, A. N. G.; Fan, H.; Wang, Y.; Prieto, V.; Longoria, J. A.; Ramesh, S.; Saini, R. K.; Kittrell, C. *et al.* Phase Behavior and Rheology of SWNTs in Superacids. *Macromolecules* **2004**, *37*, 154–160.
92. Paci, J. T.; Belytschko, T.; Schatz, G. C. Computational Studies of the Structure, Behavior Upon Heating, and Mechanical Properties of Graphite Oxide. *J. Phys. Chem. C* **2007**, *111*, 18099–18111.
93. Li, J.-L.; Kudin, K.; McAllister, M.; Prud’homme, R.; Aksay, I.; Car, R. Oxygen-Driven Unzipping of Graphitic Materials. *Phys. Rev. Lett.* **2006**, *96*, 176101.
94. Chiang, L. Y.; Upasani, R. B.; Swirczewski, J. W. Versatile Nitronium Chemistry for C<sub>60</sub> Fullerene Functionalization. *J. Am. Chem. Soc.* **1992**, *114*, 10154–10157.
95. Forrest, G. A.; Alexander, A. J. A Model for the Dependence of Carbon Nanotube Length on Acid Oxidation Time. *J. Phys. Chem. C* **2007**, *111*, 10792–10798.
96. Kaempgen, M.; Lebert, M.; Haluska, M.; Nicoloso, N.; Roth, S. Sonochemical Optimization of the Conductivity of Single Wall Carbon Nanotube Networks. *Adv. Mater.* **2008**, *20*, 616–620.
97. Shirley, D. A. High-Resolution X-Ray Photoemission Spectrum of the Valence Bands of Gold. *Phys. Rev. B* **1972**, *5*, 4709–4714.
98. Bronikowski, M. J.; Willis, P. a.; Colbert, D. T.; Smith, K. a.; Smalley, R. E. Gas-phase Production of Carbon Single-walled Nanotubes from Carbon Monoxide via the HiPco Process: A Parametric Study. *J. Vac. Sci. Technol., A* **2001**, *19*, 1800–1805.
99. Dresselhaus, M. S.; Dresselhaus, G.; Jorio, a. Raman Spectroscopy of Carbon Nanotubes in 1997 and 2007. *J. Phys. Chem. C* **2007**, *111*, 17887–17893.
100. Villalpando-Paez, F.; Son, H.; Nezich, D.; Hsieh, Y. P.; Kong, J.; Kim, Y. a; Shimamoto, D.; Muramatsu, H.; Hayashi, T.; Endo, M. *et al.* Raman Spectroscopy Study of Isolated Double-walled Carbon Nanotubes with Different Metallic and Semiconducting Configurations. *Nano Lett.* **2008**, *8*, 3879–3886.
101. Maultzsch, J.; Telg, H.; Reich, S.; Thomsen, C. Radial Breathing Mode of Single-walled Carbon Nanotubes: Optical Transition Energies and Chiral-index Assignment. *Phys. Rev. B* **2005**, *72*, 205438.

102. Telg, H.; Maultzsch, J.; Reich, S.; Thomsen, C. Resonant-Raman Intensities and Transition Energies of the E11 Transition in Carbon Nanotubes. *Phys. Rev. B* **2006**, *74*, 115415.
103. Araujo, P.; Doorn, S.; Kilina, S.; Tretiak, S.; Einarsson, E.; Maruyama, S.; Chacham, H.; Pimenta, M.; Jorio, A. Third and Fourth Optical Transitions in Semiconducting Carbon Nanotubes. *Phys. Rev. Lett.* **2007**, *98*, 067401.
104. Green, A. A.; Hersam, M. C. Processing and Properties of Highly Enriched Double-wall Carbon Nanotubes. *Nat. Nanotechnol.* **2008**, *14*, 1–7.
105. Hayashi, T.; Shimamoto, D.; Kim, Y. A.; Muramatsu, H.; Okino, F.; Touhara, H.; Shimada, T.; Miyauchi, Y.; Maruyama, S.; Terrones, M. *et al.* Selective Optical Property Modification of Double-Walled Carbon Nanotubes by Fluorination. *ACS Nano* **2008**, *2*, 485–488.
106. Khlobystov, A. N. . *Chemistry of Carbon Nanotubes*; Basiuk, V.; Basiuk, E., Eds.; American Scientific Publishers: Stevenson Ranch, CA, 2008; pp. 87–111.
107. Zhang, J.; Zou, H.; Qing, Q.; Yang, Y.; Li, Q.; Liu, Z.; Guo, X.; Du, Z. Effect of Chemical Oxidation on the Structure of Single-Walled Carbon Nanotubes. *J. Phys. Chem. B* **2003**, *107*, 3712–3718.
108. Ajayan, P. M.; Schadler, L. S.; Giannaris, C.; Rubio, a. Single-Walled Carbon Nanotube-Polymer Composites: Strength and Weakness. *Adv. Mater.* **2000**, *12*, 750–753.
109. Hatton, R. A.; Blanchard, N. P.; Tan, L. W.; Latini, G.; Cacialli, F.; Silva, S.; P, R. Oxidised Carbon Nanotubes as Solution Processable, High Work Function Hole-extraction Layers for Organic Solar Cells. *Organic Electronics* **2009**, *10*, 388–395.
110. Park, S.; Ruoff, R. S. Chemical Methods for the Production of Graphenes. *Nat. Nanotechnol.* **2009**, *4*, 217–224.
111. Chattopadhyay, J.; Cortez, F. D. J.; Chakraborty, S.; Slater, N. K. H.; Billups, W. E. Synthesis of Water-Soluble PEGylated Single-Walled Carbon Nanotubes. *Chem. Mater.* **2006**, *18*, 5864–5868.
112. Ziegler, K. J.; Gu, Z.; Peng, H.; Flor, E. L.; Hauge, R. H.; Smalley, R. E. Controlled Oxidative Cutting of Single-walled Carbon Nanotubes. *J. Am. Chem. Soc.* **2005**, *127*, 1541–1547.

113. Irle, S.; Mews, A.; Morokuma, K. Theoretical Study of Structure and Raman Spectra for Models of Carbon Nanotubes in Their Pristine and Oxidized Forms. *J. Phys. Chem. A* **2002**, *106*, 11973–11980.
114. Piao, Y.; Chen, C.-F.; Green, A. a.; Kwon, H.; Hersam, M. C.; Lee, C. S.; Schatz, G. C.; Wang, Y. Optical and Electrical Properties of Inner Tubes in Outer Wall-Selectively Functionalized Double-Wall Carbon Nanotubes. *J. Phys. Chem. Lett.* **2011**, *2*, 1577–1582.
115. Huang, J.; Ng, A. L.; Piao, Y.; Chen, C.-F.; Green, A. a; Sun, C.-F.; Hersam, M. C.; Lee, C. S.; Wang, Y. Covalently Functionalized Double-walled Carbon Nanotubes Combine High Sensitivity and Selectivity in the Electrical Detection of Small Molecules. *J. Am. Chem. Soc.* **2013**, *135*, 2306–2312.
116. Khabashesku, V. N.; Billups, W. E.; Margrave, J. L. Fluorination of Single-wall Carbon Nanotubes and Subsequent Derivatization Reactions. *Acc. Chem. Res.* **2002**, *35*, 1087–1095.
117. Srivastava, D.; Brenner, D. W.; Schall, J. D.; Ausman, K. D.; Yu, M.; Ruoff, R. S. Predictions of Enhanced Chemical Reactivity at Regions of Local Conformational Strain on Carbon Nanotubes□: Kinky Chemistry. *J. Phys. Chem. B* **1999**, *103*, 4330–4337.
118. Niyogi, S.; Hamon, M. a.; Hu, H.; Zhao, B.; Bhowmik, P.; Sen, R.; Itkis, M. E.; Haddon, R. C. Chemistry of Single-Walled Carbon Nanotubes. *Acc. Chem. Res.* **2002**, *35*, 1105–1113.
119. Allen, M. J.; Tung, V. C.; Kaner, R. B. Honeycomb Carbon: a Review of Graphene. *Chem. Rev.* **2010**, *110*, 132–145.
120. García-Lastra, J.; Thygesen, K.; Strange, M.; Rubio, Á. Conductance of Sidewall-Functionalized Carbon Nanotubes: Universal Dependence on Adsorption Sites. *Phys. Rev. Lett.* **2008**, *101*, 236806.
121. López-Bezanilla, A.; Triozon, F.; Latil, S.; Blase, X.; Roche, S. Effect of the Chemical Functionalization on Charge Transport in Carbon Nanotubes at the Mesoscopic Scale. *Nano Lett.* **2009**, *9*, 940–944.
122. Sharma, R.; Baik, J. H.; Perera, C. J.; Strano, M. S. Anomalously Large Reactivity of Single Graphene Layers and Edges Toward Electron Transfer Chemistries. *Nano Lett.* **2010**, *10*, 398–405.
123. Wang, Y.; Mirkin, C. a; Park, S.-J. Nanofabrication Beyond Electronics. *ACS Nano* **2009**, *3*, 1049–1056.

124. Deng, S.; Brozena, A. H.; Zhang, Y.; Piao, Y.; Wang, Y. Diameter-dependent, Progressive Alkylcarboxylation of Single-walled Carbon Nanotubes. *Chem. Commun.* **2011**, *47*, 758–760.
125. Liang, F.; Sadana, A. K.; Peera, A.; Chattopadhyay, J.; Gu, Z.; Hauge, R. H.; Billups, W. E. A Convenient Route to Functionalized Carbon Nanotubes. *Nano Lett.* **2004**, *4*, 1257–1260.
126. Birch, A. J. Reduction by Dissolving Metals. *J. Am. Chem. Soc.* **1942**, *64*, 430–436.
127. Chen, J.; Hamon, M. A.; Hu, H.; Chen, Y.; Rao, A. M.; Eklund, P. C.; Haddon, R. C. Solution Properties of Single-Walled Carbon Nanotubes. *Science* **1998**, *282*, 95–98.
128. Rubloff, G. W.; Liehr, M.; Young, D. R. Defect Microchemistry at the SiO<sub>2</sub>/Si Interface. *Phys. Rev. Lett.* **1987**, *58*, 2379–2382.
129. Chung, C.-H.; Yeom, H.; Yu, B.; Lyo, I.-W. Oxidation of Step Edges on Si(001)-c(4×2). *Phys. Rev. Lett.* **2006**, *97*, 036103.
130. Wang, Y.; Shan, H.; Hauge, R. H.; Pasquali, M.; Smalley, R. E. A Highly Selective, One-pot Purification Method for Single-walled Carbon Nanotubes. *J. Phys. Chem. B* **2007**, *111*, 1249–1252.
131. Zhang, Y.; Son, H.; Zhang, J.; Kong, J.; Liu, Z. Laser-Heating Effect on Raman Spectra of Individual Suspended Single-Walled Carbon Nanotubes. *J. Phys. Chem. C* **2007**, *111*, 1988–1992.
132. George, S. M.; Ott, A. W.; Klaus, J. W. Surface Chemistry for Atomic Layer Growth. *J. Phys. Chem.* **1996**, *100*, 13121–13131.
133. Zhang, Y.; Wang, Y. Gold-Substrate-Enhanced Scanning Electron Microscopy of Functionalized Single-Wall Carbon Nanotubes. *J. Phys. Chem. Lett.* **2011**, *2*, 885–888.
134. Leskelä, M.; Ritala, M. Atomic Layer Deposition Chemistry: Recent Developments and Future Challenges. *Angew. Chem., Int. Ed. Engl.* **2003**, *42*, 5548–5554.
135. Farmer, D. B.; Gordon, R. G. ALD of High-κ Dielectrics on Suspended Functionalized SWNTs. *Electrochem. Solid-State Lett.* **2005**, *8*, G89–G91.
136. Wang, X.; Tabakman, S. M.; Dai, H. Atomic Layer Deposition of Metal Oxides on Pristine and Functionalized Graphene. *J. Am. Chem. Soc.* **2008**, *130*, 8152–8153.

137. Davis, V. A.; Parra-Vasquez, A. N. G.; Green, M. J.; Rai, P. K.; Behabtu, N.; Prieto, V.; Booker, R. D.; Schmidt, J.; Kesselman, E.; Zhou, W. *et al.* True Solutions of Single-walled Carbon Nanotubes for Assembly into Macroscopic Materials. *Nat. Nanotechnol.* **2009**, *4*, 830–834.
138. Moniruzzaman, M.; Chattopadhyay, J.; Billups, W. E.; Winey, K. I. Tuning the Mechanical Properties of SWNT/nylon 6,10 Composites with Flexible Spacers at the Interface. *Nano Lett.* **2007**, *7*, 1178–1185.
139. Kelly, K. F.; Chiang, I. W.; Mickelson, E. T.; Hauge, R. H.; Margrave, J. L.; Wang, X.; Scuseria, G. E.; Radloff, C.; Halas, N. J. Insight into the Mechanism of Sidewall Functionalization of Single-walled Nanotubes: An STM Study. *Chem. Phys. Lett.* **1999**, *313*, 445–450.
140. Chou, S. G.; Son, H.; Kong, J.; Jorio, a.; Saito, R.; Zheng, M.; Dresselhaus, G.; Dresselhaus, M. S. Length Characterization of DNA-wrapped Carbon Nanotubes Using Raman Spectroscopy. *Appl. Phys. Lett.* **2007**, *90*, 131109.
141. Simpson, J. R.; Fagan, J. A.; Becker, M. L.; Hobbie, E. K.; Hight Walker, A. R. The Effect of Dispersant on Defects in Length-separated Single-wall Carbon Nanotubes Measured by Raman Spectroscopy. *Carbon* **2009**, *47*, 3238–3241.
142. Perdew, J.; Burke, K.; Ernzerhof, M. Generalized Gradient Approximation Made Simple. *Phys. Rev. Lett.* **1996**, *77*, 3865–3868.
143. Troullier, N.; Martins, J. L. Efficient Pseudopotentials for Plane-wave Calculations. *Phys. Rev. B* **1991**, *43*.
144. Zimmerman, H. E.; Wang, P. A. The Regioselectivity of the Birch Reduction. *J. Am. Chem. Soc.* **1993**, *115*, 2205–2216.
145. Sun, C.; Karki, K.; Jia, Z.; Liao, H.; Zhang, Y.; Li, T.; Qi, Y.; Cumings, J.; Rubloff, G. W.; Wang, Y. A Beaded-String Silicon Anode. *ACS Nano* **2013**, *7*, 2717–2724.
146. Piao, Y.; Meany, B.; Powell, L. R.; Valley, N.; Kwon, H.; Schatz, G. C.; Wang, Y. Brightening of Dark Excitons in Covalently Functionalized Carbon Nanotubes with Sp<sub>3</sub> Defects. *Nat. Chem.* **2013**.
147. Brozena, A. H.; Leeds, J. D.; Zhang, Y.; Wang, Y. Trion Photoluminescence of Covalently Functionalized, Semiconducting Carbon Nanotubes. **2013**, To be submitted.
148. Rønnow, T. F.; Pedersen, T. G.; Cornean, H. D. Stability of Singlet and Triplet Trions in Carbon Nanotubes. *Phys. Lett. A* **2009**, *373*, 1478–1481.

149. Matsunaga, R.; Matsuda, K.; Kanemitsu, Y. Observation of Charged Excitons in Hole-Doped Carbon Nanotubes Using Photoluminescence and Absorption Spectroscopy. *Phys. Rev. Lett.* **2011**, *106*, 37404.
150. Park, J. S.; Hirana, Y.; Mouri, S.; Miyauchi, Y.; Nakashima, N.; Matsuda, K. Observation of Negative and Positive Trions in the Electrochemically Carrier-doped Single-walled Carbon Nanotubes. *J. Am. Chem. Soc.* **2012**, *134*, 14461–14466.
151. Santos, S.; Yuma, B.; Berciaud, S.; Shaver, J.; Gallart, M.; Gilliot, P.; Cognet, L.; Lounis, B. All-Optical Trion Generation in Single-Walled Carbon Nanotubes. *Phys. Rev. Lett.* **2011**, *107*, 1–5.
152. Klingshirn, C. *Semiconductor Optics*; 2nd ed.; Springer, 2005; pp. 254–259.
153. Mouri, S.; Miyauchi, Y.; Iwamura, M.; Matsuda, K. Temperature Dependence of Photoluminescence Spectra in Hole-doped Single-walled Carbon Nanotubes: Implications of Trion Localization. *Phys. Rev. B* **2013**, *87*, 045408.
154. Barone, P. W.; Baik, S.; Heller, D. a; Strano, M. S. Near-infrared Optical Sensors Based on Single-walled Carbon Nanotubes. *Nat. Mater.* **2005**, *4*, 86–92.
155. Jin, H.; Heller, D. a; Kalbacova, M.; Kim, J.-H.; Zhang, J.; Boghossian, A. A.; Maheshri, N.; Strano, M. S. Detection of Single-molecule H<sub>2</sub>O<sub>2</sub> Signalling from Epidermal Growth Factor Receptor Using Fluorescent Single-walled Carbon Nanotubes. *Nat. Nanotechnol.* **2010**, *5*, 302–309.
156. Hudson, J. L.; Casavant, M. J.; Tour, J. M. Water-soluble, Exfoliated, Nonroping Single-wall Carbon Nanotubes. *J. Am. Chem. Soc.* **2004**, *126*, 11158–11159.
157. Danek, O.; Snobl, D.; Knizek, I.; Nouzova, S. Diazotization of Aminophenols in Concentrated Fluoroboric Acid. *Collect. Czech. Chem. Commun.* **1967**, *32*, 1642–1645.
158. Strano, M. S.; Huffman, C. B.; Moore, V. C.; O'Connell, M. J.; Haroz, E. H.; Hubbard, J.; Miller, M.; Rialon, K.; Kittrell, C.; Ramesh, S. *et al.* Reversible, Band-Gap-Selective Protonation of Single-Walled Carbon Nanotubes in Solution. *J. Phys. Chem. B* **2003**, *107*, 6979–6985.
159. Bahr, J. L.; Yang, J.; Kosynkin, D. V; Bronikowski, M. J.; Smalley, R. E.; Tour, J. M. Functionalization of Carbon Nanotubes by Electrochemical

- Reduction of Aryl Diazonium Salts: a Bucky Paper Electrode. *J. Am. Chem. Soc.* **2001**, *123*, 6536–42.
- 160. Usrey, M. L.; Lippmann, E. S.; Strano, M. S. Evidence for a Two-step Mechanism in Electronically Selective Single-walled Carbon Nanotube Reactions. *J. Am. Chem. Soc.* **2005**, *127*, 16129–16135.
  - 161. Collins, P. G. Extreme Oxygen Sensitivity of Electronic Properties of Carbon Nanotubes. *Science* **2000**, *287*, 1801–1804.
  - 162. Klinke, C.; Hannon, J. B.; Afzali, A.; Avouris, P. Field-effect Transistors Assembled from Functionalized Carbon Nanotubes. *Nano Lett.* **2006**, *6*, 906–910.
  - 163. Dyke, C. A.; Tour, J. M. Unbundled and Highly Functionalized Carbon Nanotubes from Aqueous Reactions. *Nano Lett.* **2003**, *3*, 1215–1218.
  - 164. Nishihara, T.; Yamada, Y.; Kanemitsu, Y. Dynamics of Exciton-hole Recombination in Hole-doped Single-walled Carbon Nanotubes. *Phys. Rev. B* **2012**, *86*, 075449.